



GEORGEAU

CONSTRUCTION
RESEARCH
CENTER

Title: **Development of a Simulation and Experimental Environment
for Evaluating Structural Performance under Wind Loads**

PI(s): **Upul Attanayake, Ph.D., P.E.
William Liou, Ph.D.
Kanchani Basnayake, M.Sc.**

Report Number: 18-2

Date: **December 31, 2019**

ABSTRACT

Roofing system failures are most commonly observed during post hurricane and tornado disaster investigations. Such failures allow water penetration leading to significant damages/losses to a building's interior and possible structural failure. The magnitude of such disasters and expected unfavorable conditions, potentially being developed due to climate change, prompted us to study the means and methods of improving the resilience of structures, including roofing systems. This study was initiated to (i) synthesize the state-of-the-art and practice for improving roofing system performance under damaging wind conditions, (ii) develop an experimental facility and necessary instrumentation to study monitoring system performance, wind loading and structural response under various exposure conditions, and (iii) develop the necessary workforce and resources to perform wind-structure interaction simulations. The scope of this study is limited to flat roof systems in low-rise buildings. Typically, high negative pressure (suction) is observed at roof corners and edges due to wind. The pressure magnitude depends on the wind, building, and roofing system characteristics as well as the terrain and surrounding environment. Geometric modifications of the existing roof by rounding and chamfering the edges and installing wind suction mitigation features/devices at the roof corners and edges are the two approaches implemented to control pressure magnitudes. Such techniques and approaches were documented through a comprehensive review of literature. An experimental facility that includes the experimental building, meteorological measurement system, roof response (displacement, force, and pressure) measurement system, and the data acquisition system was designed with a cost estimate. Also, wind-structure interaction simulation and model validation using published data are discussed. The wind-structure interaction simulation capabilities demonstrated during this project can be extended to investigate wind-structure interaction for the design of experiments and evaluation of various options for mitigating roof damage under high wind loads.

DISCLAIMER

The content of this report reflects the views of the authors, who are solely responsible for the facts and the accuracy of the information presented herein. This publication is disseminated under the sponsorship of the Georgeau Construction Research Center (GCRC) in the interest of information exchange. This report does not necessarily reflect the official views or policies of GCRC, who assume no liability for the contents or use thereof. This report does not represent standards, specifications, or regulations.

ACKNOWLEDGMENT

The authors greatly appreciate the Georgeau Construction Research Center (GCRC) at Western Michigan University for funding this research project.

TABLE OF CONTENTS

ABSTRACT.....	II
DISCLAIMER.....	III
ACKNOWLEDGMENT	III
LIST OF TABLES	VI
TABLE OF FIGURES.....	VIII
1 INTRODUCTION.....	1
1.1 Overview	1
1.2 Project Objectives and Scope	5
1.3 Report Organization	5
2 STATE-OF-THE-ART LITERATURE AND PRACTICE REVIEW	6
2.1 Objective and Approach	6
2.2 Wind Flow Pattern around a Building with a Flat Roof.....	6
2.2.1 Flow Visualization Techniques.....	9
2.2.2 Factors Affecting the Roof Pressure Distribution.....	10
2.3 Wind Suction Mitigation Features and Devices for Flat and Steep Sloped Roofs.....	18
2.3.1 Roof Geometry Modifications	18
2.3.2 Architectural Aerodynamic Features/Devices	23
2.4 Wind Flow Measurements around a Low-Rise Building	53
2.4.1 Instrumented Low-rise Buildings	54
2.4.2 Instrumented Experimental Structures.....	57
2.4.3 Flow (Wind) Measurement Equipment/System.....	59
2.4.4 Pressure Measurement System	62
2.4.5 Structural Response Measurement System	63
2.4.6 Data Acquisition and Data Processing System	64
2.5 Summary.....	76
3 NUMERICAL SIMULATION OF THE FLOW AROUND A FLAT ROOF OF A LOW-RISE BUILDING.....	77
3.1 Objective and Approach	77
3.2 Experimental Structure	77
3.3 Numerical Model.....	78

3.4 Results and Discussion	81
3.5 Summary and Conclusions	83
4 PROPOSED OUTDOOR EXPERIMENTAL FACILITY.....	85
4.1 Objective and Approach	85
4.2 Design Details and the Cost Estimate	85
4.2.1 Design Details of the Experimental Structure	85
4.2.2 Meteorological System	102
4.2.3 Structural Response Measurement System.....	105
4.2.4 Data Acquisition System (DAS).....	111
4.3 Summary.....	112
5 SUMMARY, CONCLUSIONS, AND RECOMMENDATIONS	114
5.1 Summary and Conclusions	114
5.1.1 Roof Wind Pressure Distribution.....	114
5.1.2 Wind Suction Mitigation Techniques for a Low-Rise Building.....	116
5.1.3 Wind Pressure Measurements of a Full-Scale Low-Rise Building	124
5.1.4 Numerical Simulation of the Flow around a Flat Roof of a Low-Rise Building....	125
5.2 Recommendations	125
5.2.1 Wind Suction Mitigation Approaches	125
5.2.2 Numerical Simulations to Predict Wind Loads on Flat Roofs.....	128
6 REFERENCE.....	129

APPENDIX A: ABBREVIATIONS

APPENDIX B: SYMBOLS AND NOTATIONS

APPENDIX C: INSTRUMENTED EXPERIMENTAL OUTDOOR FACILITIES

APPENDIX D: THE PROPOSED EXPERIMENTAL FACILITY

APPENDIX E: QUOTATIONS

LIST OF TABLES

Table 2-1. Effect of Edge Modifications on the Aerodynamic Drag and Lift Force Coefficients on a Flat Roof Building under a Wind Angle of 45° (Aly and Bresowar 2016)	22
Table 2-2. Porous Screen Shapes and Reduction of Wind Load at Roof Corners (25.4 mm = 1 in.) (Cochran and English 1997)	28
Table 2-3. Test Configurations Used in Gravel Scour Testing (Chowdhury and Blessing 2007)	35
Table 2-4. Test Configurations Used in Pressure Measurements and the Observations Made (Chowdhury and Blessing 2007)	37
Table 2-5. Peak Values of Minimum Pressure Coefficients (Cp) with and without Solar Panels (Iverson 2016).....	47
Table 2-6. ASCE 07-10 Pressure Coefficients and Measured Values with and without Solar Panels (Iverson 2016).....	48
Table 2-7. Drag and Lift Coefficients on the Building and the Damage Mitigation Devices (Aly and Bresowar 2016)	49
Table 2-8. Drag and Lift Coefficients on the Gable Roof Building with Different Solar Panel Configurations (Aly et al. 2017)	50
Table 2-9. Instrumented Low-Rise Buildings for Wind Pressure and Response Monitoring	55
Table 2-10. Pressure Transducer Details in TTU Building (Levitan and Mehta 1992a).....	68
Table 2-11. Details of the Anemometers (Levitan and Mehta 1992b)	69
Table 2-12. Specifications of the Anemometers (Huang et al. 2012).....	73
Table 2-13. Specifications of the Pressure Transducers (Huang et al. 2012)	73
Table 3-1. Boundary Condition Definitions	80
Table 4-1. Cost Estimate for the Structure.....	94
Table 4-2. Cost Estimate for the Flat Roof and Steep Sloped Roof Systems	97
Table 4-3. Cost Estimate for the Anchoring System	101
Table 4-4. Cost Estimate for the Flooring and Wall Materials.....	102
Table 4-5. Cost Estimate for the Meteorological System	105
Table 4-6. Cost Estimate for a Pressure Measurement System	109
Table 4-7. Cost Estimate for the Displacement and Force Measurement System.....	111
Table 4-8. Cost Estimate for the DAS	112
Table 4-9. Cost Estimate for the Proposed Experimental System	113

Table 5-1. Impact of Wind and Structure Characteristics on Wind Pressure Distribution and Magnitude over a Low-Rise Building Roof.....	115
Table 5-2. Roof Edge Modification - A Summary of Findings.....	117
Table 5-3. Research Findings on Aerodynamic Devices - Parapets.....	119
Table 5-4. Research Findings on Aerodynamic Devices – Parapets (Contd.).....	120
Table 5-5. Research Findings on Aerodynamic Devices - Parapets (Contd.)	121
Table 5-6. Research Findings on Aerodynamic Devices – Spoilers.....	122

TABLE OF FIGURES

Figure 1-1. Flow patterns around rigid and deformable roofs (Sun et al. 2012)	2
Figure 1-2. External pressure coefficients for flat and steep sloped roofs (ASCE 2010).....	4
Figure 2-1. Wind flow patterns around a low-rise cube shaped building (Wu 2000)	6
Figure 2-2. Separation bubble and the resulting pressure distribution on a flat roof under a boundary layer flow (Cook 1985).....	7
Figure 2-3. Formation of a separation bubble on a sloped roof (Wang 1998).....	7
Figure 2-4. Formation of conical vortices (a) and the resulting typical pressure distribution on a flat roof (b) (Cook 1985).....	8
Figure 2-5. Roof damages indicating high-pressure zones during hurricanes (FEMA 2006).....	9
Figure 2-6. Flow visualization techniques	10
Figure 2-7. Separation bubbles and pressure distribution on a flat roof under uniform flow (a) and a boundary layer flow (b) (Cook 1985)	11
Figure 2-8. Peak roof pressure coefficient variation with wind direction (Lin et al. 1995)	12
Figure 2-9. Isobar diagrams (Gerhardt and Kramer 1992)	13
Figure 2-10. ASCE 07 definitions of flat roof wind pressure zones.....	13
Figure 2-11. Impact of roof geometry on wind uplift forces (Keote et al. 2015)	15
Figure 2-12. Effect of roof pitch on wind flow patterns (Cook 1985).....	15
Figure 2-13. Variation of the minimum pressure coefficient over gable, hip, and flat roofs (Prasad and Ahmed 2009).....	16
Figure 2-14. Velocity streamlines around buildings with various roof designs (Enteria 2016)..	17
Figure 2-15. Effect of roof pitch and wind angle on the pressure distribution on a pyramidal roof (Singh and Roy 2019)	18
Figure 2-16. Model geometry and pressure tap locations on the roof (Blackmore 1988)	19
Figure 2-17. Aerodynamically modified roof geometries (Sehn 2008).....	19
Figure 2-18. Flow separation in the presence of sharp and rounded edges under two wind directions: 90° (a) and 45° (b) (Mahmood 2011)	20
Figure 2-19. Flow separation in the presence of sharp and rounded edge models under a 25° wind direction (Mahmood 2011)	21
Figure 2-20. Roof edge modifications (Aly and Bresowar 2016)	21
Figure 2-21. Mean pressure distribution under wind directions 0° and 45° (Dong et al. 2019)..	23

Figure 2-22. Impact of parapets on roof pressure distribution (Lstiburek 2012)..... 24

Figure 2-23. Parapet configurations for altering wind flow over roofs (Kopp et al. 2005)..... 24

Figure 2-24. Influence of parapet configuration on the vortex formation (Pinando et. al 2009). 25

Figure 2-25. Aerodynamic mitigation techniques (Sehn 2008)..... 26

Figure 2-26. Roof corner configurations (25.4 mm = 1 in.) (Surry and Lin 1995) 27

Figure 2-27. Flow divider and the working principle (25.4 mm = 1 in.) (Banks et al. 2001) 29

Figure 2-28. Geometry of the flat plate (a), circular cylinder flow divider (b), and the variation of minimum pressure coefficients in the presence of roof suction mitigation devices (c) (25.4 mm = 1 in.) (Banks et al. 2001)..... 30

Figure 2-29. Perimetric spoiler evaluated by Kopp et al. (2005b)..... 31

Figure 2-30. Minimum pressure coefficient distribution along the line $y/H = 0.42$ (25.4 mm = 1 in.) (Kopp et al. 2005a)..... 32

Figure 2-31. A test structure placed in front of the WOW at a 45° wind direction (Chowdhury and Blessing 2007) 33

Figure 2-32. Modified and standard roof edge devices (Chowdhury and Blessing 2007) 34

Figure 2-33. Comparison of the scour threshold wind speeds as a function of the gravel diameter for traditional roof edge products and the AeroEdge guard (Lin et al. 2008) 36

Figure 2-34. Aerodynamic mitigation techniques (Sehn 2008)..... 38

Figure 2-35. Test model placed inside the wind tunnel (a) and pressure tap layout on the roof (b) (Suaris and Irwin 2010) 38

Figure 2-36. Variation of the peak pressure coefficient along the gable end (a), ridge (b), and eave (c) (Suaris and Irwin 2010)..... 39

Figure 2-37. Architectural elements installed on the roof (Bitsuamalak et al. 2013)..... 40

Figure 2-38. Variation of peak pressure coefficients on the gable roof and hip roof model with pergolas and ridge extensions under 0° wind direction (Bitsuamalak et al. 2013)..... 41

Figure 2-39. Variation of peak pressure coefficients on the gable roof with gable end extensions under 90° wind direction (Bitsuamalak et al. 2013) 41

Figure 2-40. Different parapet configurations installed on the full-scale structure (Huang et al. 2013) 42

Figure 2-41. Fluctuating wind pressure coefficients on the roof with a continuous parapet (a) and a corner parapet (b) (Huang et al. 2013)..... 43

Figure 2-42. Fluctuating wind pressure coefficients on the roof with the four-segment discrete parapet with 180° wind (Huang et al. 2013)..... 44

Figure 2-43. Eave configurations used by Huang et al. (2014) (units are in m, 1 m = 39 in.) 44

Figure 2-44. Variation of the maximum uplift pressure coefficients on the windward roof surface of the three models with the wind direction..... 45

Figure 2-45. Sand erosion observed on flat roofs installed with solar panels along the roof edge (Iverson 2016)..... 47

Figure 2-46. Roof damage mitigation devices evaluated by Aly and Bresowar (2016)..... 48

Figure 2-47. Tested solar panel configurations (Aly et al. 2017) 49

Figure 2-48. Numerical and experimental work conducted by Aly et al. (2017) 50

Figure 2-49. Spoiler configurations evaluated by Li et.al (2018)..... 51

Figure 2-50. Aerodynamics Mitigation and Power Systems (AMPS) evaluated by Chowdhury et al. (2019)..... 52

Figure 2-51. Formation of conical vortices under wind direction of 45° and the impact of wind turbines mounted at roof corners (Chowdhury et al. 2019)..... 52

Figure 2-52. Evaluation of wind loads and structural response..... 53

Figure 2-53. Building site and previous typhoon paths (Li et al. 2012b) 57

Figure 2-54. The movable HNU experimental building (Li et al. 2017a) 58

Figure 2-55. Location of the meteorological tower and the TTU experimental building (Smith et al. 2017) 59

Figure 2-56. Wind speed and/or direction measuring instruments 61

Figure 2-57. Schematic diagram of the pressure measurement system with rain traps (Li et al. 2012a) 63

Figure 2-58. Pressure scanner (scanning system) connected to a model tile (Masters and Gurley 2011)..... 63

Figure 2-59. Displacement sensors 64

Figure 2-60. Details of a force measurement system (Kim and Mehta 1980)..... 64

Figure 2-61. Components of a data acquisition system (National Instruments 2019a)..... 65

Figure 2-62. Wind Engineering Research Field Laboratory (WERFL) of Texas Tech University (TTU), U.S..... 66

Figure 2-63. Pressure tap layout on the TTU building (Smith et al. 2017) 67

Figure 2-64. Arrangement of pressure measurement tubing and instruments on the roof (Smith et al. 2007)	68
Figure 2-65. Meteorological tower located at WERFL (Smith et al. 2007)	69
Figure 2-66. Test building location, shape, and the terrain conditions (Xu et al. 2012)	71
Figure 2-67. The roof lifting mechanism and details (Xu et al. 2012, Huang et al. 2012)	71
Figure 2-68. Details of the meteorological towers at theTonji University (TJU) experimental facility (Huang et al. 2012)	72
Figure 2-69. Pressure tap layout (a) and the top and underside views of the roof (b and c) (Huang et al. 2012)	74
Figure 2-70. Pressure measurement system (a and b) and the respective pressure sensors (c and d) (Huang et al. 2012)	75
Figure 2-71. The adapter and the computer used in the DAS (Huang et al. 2012).....	75
Figure 3-1. Silsoe cube (Richards and Hoxey 2012)	78
Figure 3-2. 1:30 scale model of the Silsoe cube (Irtaza et al. 2013).....	78
Figure 3-3. Geometry of developed numerical model; Plan view (a) and Elevation view (b)	79
Figure 3-4. Details of the mesh near the cube	79
Figure 3-5. Simulated wind profile at the inlet	80
Figure 3-6. Comparison of CFD results with experimental data	81
Figure 3-7. Comparison of the numerical and experimental pressure coefficients along the mid-width of the Silsoe cube by Enteria (2016).....	82
Figure 3-8. Comparison of the numerical and experimental pressure coefficients along the mid-width of the Silsoe cube by Irtaza et al. (2013)	83
Figure 4-1. Layout of the building and typical column geometry	86
Figure 4-2. Elevation view of PF1 and PF2.....	88
Figure 4-3. Elevation view of PF3	89
Figure 4-4. Elevation view of PF4.....	89
Figure 4-5. Building column sections (Unistrut 2017)	90
Figure 4-6. Details of the beams, bracings and cross ties (Unistrut 2017)	91
Figure 4-7. Fitting details (Unistrut 2017).....	91
Figure 4-8. Connection detail showing a nut and a spring supported nut (Unistrut 2017).....	92
Figure 4-9. Locations provided for internal partitioning	93

Figure 4-10. Hurricane ties used at the truss-wall connection (Fasteners Plus 2018)	95
Figure 4-11. Open web roof truss for the flat roof.....	95
Figure 4-12. Howe type pitched roof truss to support steep sloped roof.....	96
Figure 4-13. Bracket support for the pitched roof truss (P1769) (Unistrut 2017)	96
Figure 4-14. Plan view showing the location of the anchors on the perimeter frames.....	98
Figure 4-15. Details of the anchoring system	99
Figure 4-16. Details of the anchoring system proposed for the building.....	100
Figure 4-17. Floor and wall coverings.....	101
Figure 4-18. Components of the AME-55 tower	104
Figure 4-19. Pressure measurement system components	107
Figure 4-20. Pressure measurement system installation accessories (Scanivalve Corp 2019)..	108
Figure 4-21. Ultrasonic displacement sensor and its location in a flat roof system	110
Figure 4-22. Force/torque (F/T) sensor.....	111
Figure 4-23. PXIe-1065* (National Instruments 2019b).....	112
Figure 5-1. Proposed design chart format for a flat roof with perimetric solid parapets on a rectangular building (B/L = 1.0) subjected to a wind flowing at 30°	127

1 INTRODUCTION

1.1 OVERVIEW

The net design wind pressure on a building envelope is the summation of external and internal pressure acting on the building envelope (ASCE 2010). The external pressure is a result of the wind loads acting on the envelope. The internal pressure is the pressure buildup inside the building due to openings and natural porosity of the building. The external and internal pressures can be either positive or negative (suction) (Quimby 2007). The ASCE 07 (2010) defines external and internal pressure coefficients to calculate the net design wind pressure on a building envelope based on building enclosure, such as enclosed, partially enclosed, and open. In addition to building enclosure, building rigidity is also a factor that needs to be considered for wind load calculation. Depending on structure stiffness and fixity at the supports, buildings behave as rigid or flexible structures. According to the ASCE 07 (2010), slender buildings and other structures with a fundamental frequency of less than 1 Hz are defined as flexible structures (ASCE 2010). Typically, the low-rise buildings are considered to be rigid.

Wind tunnel testing of scaled models, full-scale testing of structures under real or simulated wind loads, instrumentation of in-service buildings, and application of numerical techniques such as computational fluid dynamics (CFD) are the available methods for assessing pressure distribution on building envelopes and the resulting structural response (pressure, forces, deformation, etc.) under wind loads. Scaled and full-scale wind tunnel tests are expensive and laborious; however, they are essential for studying the loads, structural response, and the impact of various damage mitigation techniques. With the advancement in CFD simulation techniques, such tools are used to optimize the investigation process from designing experiments to providing clarifications while concluding the research findings. The CFD studies on low-rise buildings thus far assumed that the buildings are rigid. Hence, only the wind flow around such structures was simulated by placing the structure as a geometry without its structural characteristics (Vardoulakis et al. 2011, Abohela et al. 2013, Ntinis et al. 2014, Tominga et al. 2015, Enteria 2016, Aly and Bresowar 2016, and Ricci et al. 2017).

Flexible structures or components could become an integral part of a dynamically coupled system that could change the wind flow pattern around such structures. This interaction between the deformable structure and the wind flow is called the wind-structure interaction or generally termed as fluid-structure interaction (FSI) (Ansys 2019). Experimental and numerical studies have

been conducted to evaluate large deformations and potential flow-induced vibrations of tall buildings (Huang et al. 2012), tensioned membrane roofs (Halfmann et al. 2000 and Wüchner et al. 2006), bridges (Piperno and Bornet 2012), wind turbines (Hsu and Bazilevs 2012), pressurized car tanks (Yu et al. 2009), and car roofs (Knight et al. 2010), etc. Yet, a limited number of studies have been conducted to evaluate the significance of roofing system flexibility. Steep sloped roofs are considered as rigid systems due to their short-spans and stiff elements. Typically, flat roofs tend to be more flexible under transient wind conditions. Baskaran et al. (2012) recognized the need of quantifying the difference in wind loads between rigid and flexible flat roofs. A field performance study by Baskaran et al. (2012) on two roof mock-ups with two different membrane materials revealed that the membrane flexibility influenced the wind-induced response: suction pressure and membrane deformation. Sun et al. (2012) evaluated flow behavior around rigid and flexible roofs. Figure 1-1 shows the flow streamlines and flow separation over rigid and flexible roofs. The study by Sun et al. (2012) did not evaluate the pressure distribution or the possible failure mechanisms and locations.

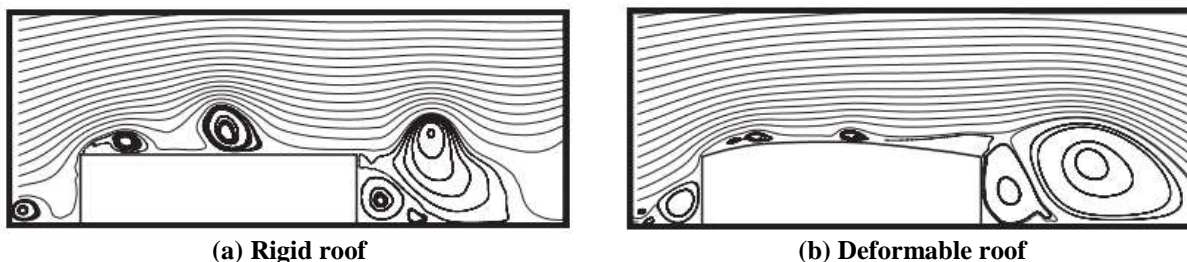
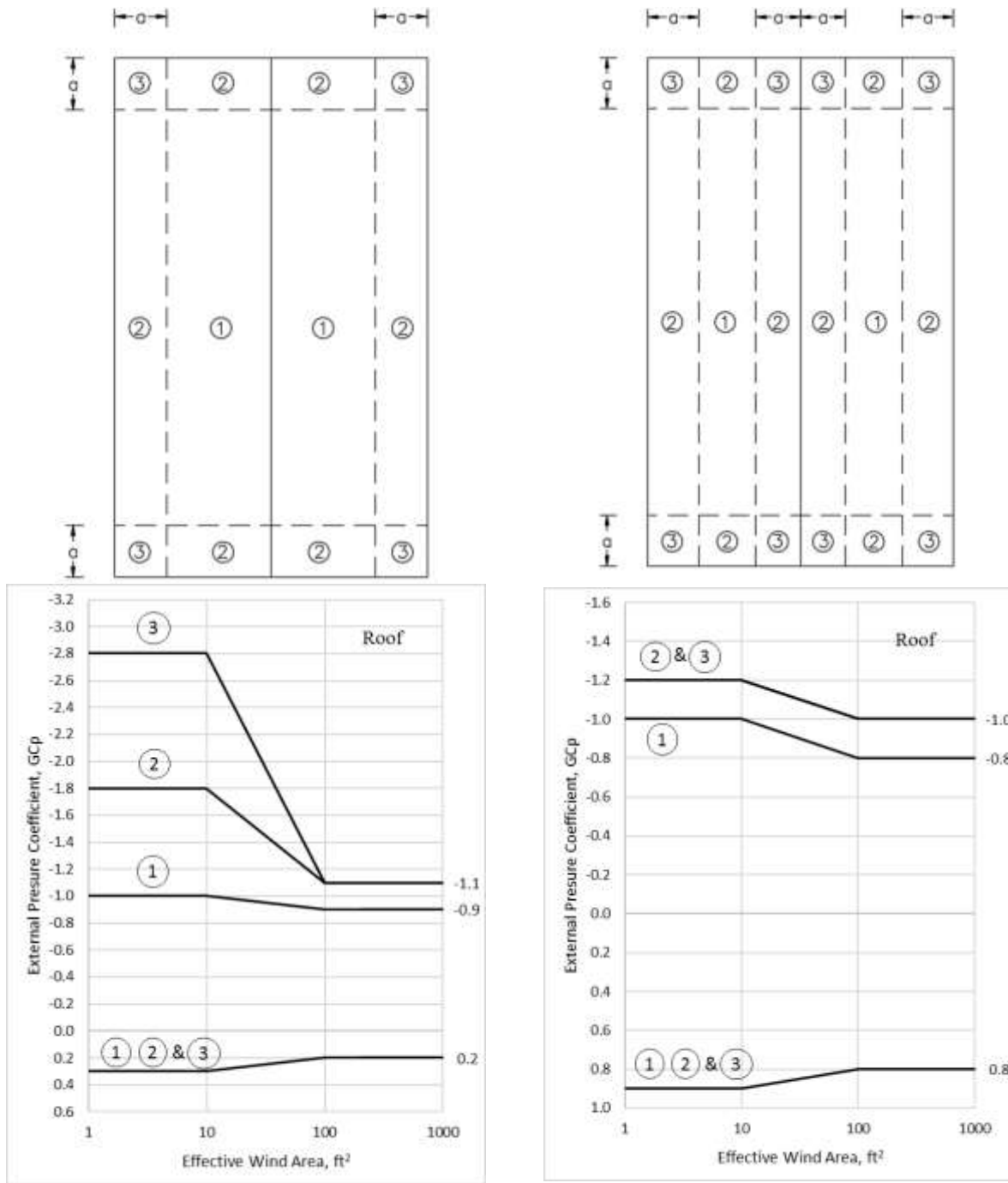


Figure 1-1. Flow patterns around rigid and deformable roofs (Sun et al. 2012)

The flow separates at roof corners and edges, generating additional pressure at such locations than what is generally observed at the interior zones. Therefore, roof damages are commonly initiated at corners and edges under high wind conditions. Federal Emergency Management Agency (FEMA) Mitigation Assessment Teams (MATs) document the performance of structures following hurricane events. The reports indicate roof corners and edges as the damage initiation zones (FEMA 2006). As a result, the ASCE 07 specifies higher external pressure coefficients for corner and edge zones. As shown in Figure 1-2, zones 1, 2 and 3 define roof interior, edge, and corner zones respectively. Figure 1-2(a) and Figure 1-2(b) show the external pressure coefficients specified for a flat roof and a gable roof respectively. Two damage mitigation techniques implemented at corners and edges include (i) modification of the roof geometry to eliminate sharp corners that cause the flow separation and (ii) installation of aerodynamic mitigation features/devices such as roof parapets, screens, spoilers, etc. (Aly and Bresowar 2016).

So far, the investigations performed using CFD tools did not consider the roof flexibility with the presence of aerodynamic mitigation features/techniques. Hence, it is necessary to investigate the effectiveness of strengthening mechanisms and/or wind suction mitigation features/techniques on flexible roofs through coupled fluid-structure interaction simulations. Moreover, it is important to conduct experimental studies to improve resilience of such structures under high wind loads.

Calibrated and/or validated numerical models can be effectively used to conduct parametric studies to develop cost effective experimental programs. Calibration and validation of the models require access to reliable experimental data. Such data can be acquired from publications or by performing experiments. Typically, wind tunnel testing is performed using scale models due to cost and availability of limited facilities to conduct full-scale testing. Concurrently, collection of data from in-service structures is of paramount importance to understand the structural behavior under transient loads. However, instrumentation, maintenance (including power supply), data storage, and data transmission are a few challenges of instrumentation and monitoring of large outdoor structures. Hence, evaluation of sensors and monitoring system component performance under harsh exposure conditions is important for developing reliable monitoring systems.



(a) For a flat roof (b) For a Gable roof with 27° - 45° roof angle
Figure 1-2. External pressure coefficients for flat and steep sloped roofs (ASCE 2010)

Note: a: 10% of the least horizontal dimension or 40% of eave height, whichever is smaller, but not less than 4% of the least horizontal dimension or 3ft.

1.2 PROJECT OBJECTIVES AND SCOPE

The primary goal of this research is to develop simulation and experimental environments for evaluating roof system response under wind loads.

The specific objectives of this research are as follows;

1. Develop computational fluid dynamics (CFD) expertise needed for wind-structure interaction simulation.
2. Design an outdoor experimental facility for sensor evaluation and data collection.
3. Develop a list of sensor technologies for measuring wind pressure distribution and structural response.
4. Develop a cost estimate for building the instrumented outdoor testing facility.

To achieve these objectives, this project was organized into four tasks: (1) review state-of-the-art literature and practice, (2) simulate wind-structure interaction, (3) design a mobile outdoor experimental facility, and (4) develop project deliverables.

1.3 REPORT ORGANIZATION

The report is organized into five chapters:

- Chapter 1 includes an overview and project objectives and scope.
- Chapter 2 includes a review of state-of-the-art and practice related to damage mitigation techniques for flat and steep sloped roofs and full-scale testing of instrumented buildings.
- Chapter 3 describes a simulation case-study that investigated the wind flow around a building and the pressure forces acting on the given structure.
- Chapter 4 describes the details of the outdoor experimental facility, including the instrumentation and data acquisition system.
- Chapter 5 includes the summary, conclusions, and recommendations for further studies.
- Chapter 6 includes the cited references.

The following appendices are included in the report.

- Appendix A: Abbreviations
- Appendix B: Symbols and Notations
- Appendix C: Instrumented Experimental Outdoor Facilities
- Appendix D: The Proposed Experimental Facility
- Appendix E: Quotations

2 STATE-OF-THE-ART LITERATURE AND PRACTICE REVIEW

2.1 OBJECTIVE AND APPROACH

This chapter presents (i) the influence of wind and building characteristics on flat roof wind pressure distribution, (ii) experimental and numerical studies on the roof damage mitigation techniques for low-rise buildings, and (iii) instrumentation and monitoring of full-scale structures to capture loading and building response.

2.2 WIND FLOW PATTERN AROUND A BUILDING WITH A FLAT ROOF

Wind flow patterns become highly complex when a free flow is disturbed by an object. Figure 2-1 shows the impact of a cube shaped building on the parabolic wind profile that approaches the building at 90 degrees. The wind reaches the windward wall and creates a stagnation area before moving outwards to the two vertical windward edges. The downward flow creates the rolled up horseshoe vortices behind the leeward wall. The upward and sideward flows separate at the top and side edges of the windward wall. Based on the building dimensions and turbulence characteristics, the separated flow may or may not reattach to the roof and side walls. If the flow gets reattached to the roof, the flow gets separated at the top edge of the leeward wall to create wakes until the flow reattaches at the ground (Wu 2000). As per the objectives of this research, the following sections will primarily describe the flow patterns near and around the roof.

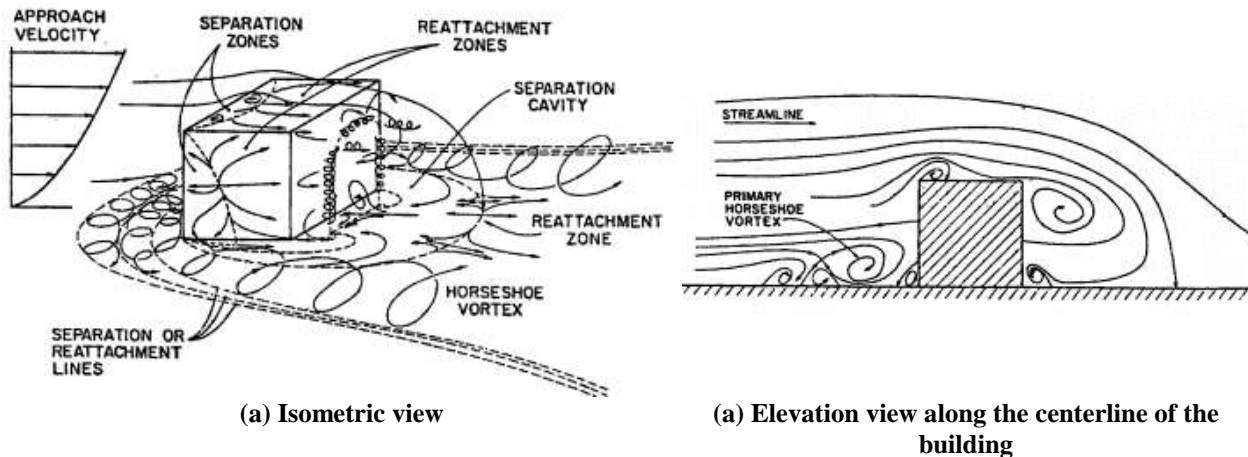


Figure 2-1. Wind flow patterns around a low-rise cube shaped building (Wu 2000)

The flow separation at locations such as corners, edges, ridges, hips, and overhangs creates vortices and results in much higher localized pressure zones. Primarily, two types of vortices are formed: separation bubble and conical vortices. The nature of these vortices depends on the direction of the wind.

The formation of a separation bubble over a flat roof is shown in Figure 2-2. The separation bubbles are formed when a wind flow is approximately normal ($70^\circ\sim 110^\circ$) to the leading edge of a roof (Banks et al. 2001). The upper third portion of the wind flow from the windward wall, rises over and separates from the leading edge (i.e. separation point, SP1) due to the adverse pressure gradient near the roof edge. This is called a separated shear flow layer. The vorticity in the separated shear layer in combination with the wind profile and the momentum from the turbulent boundary layer lowers the shear flow layer. Based on the length of the building, the lowered shear flow layer may or may not get reattached to the roof (Cook 1985). A typical pressure distribution on a flat roof with a separation bubble is shown in Figure 2-2(b). High negative pressures (suction or uplift) are at the windward edge. Figure 2-3 illustrates the formation of a separation bubble on a sloped roof. Similar to a flat roof, the flow gets separated at the leading edge and reattached at a certain distance away from the leading edge.

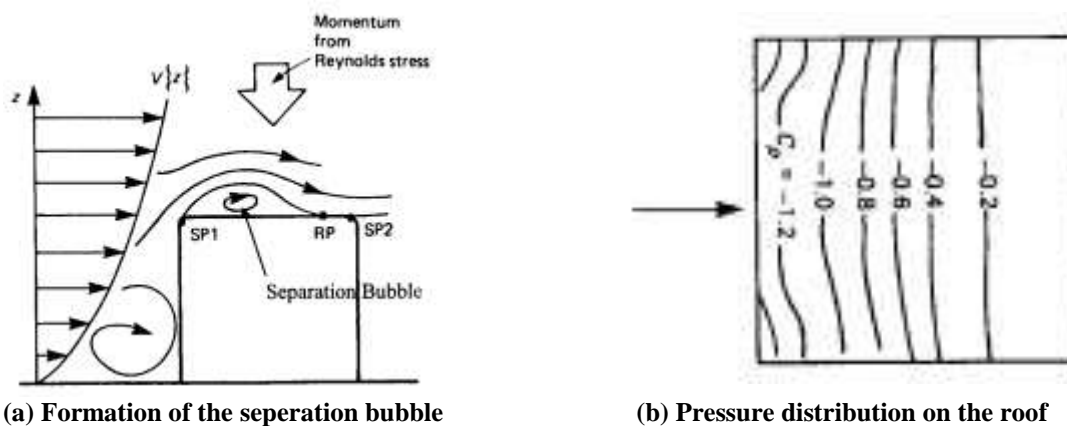


Figure 2-2. Separation bubble and the resulting pressure distribution on a flat roof under a boundary layer flow (Cook 1985)

Note: SP: Separation point, RP: Reattachment point, z : height, $V\{z\}$: Wind velocity with respect to height, C_p : Pressure coefficient.

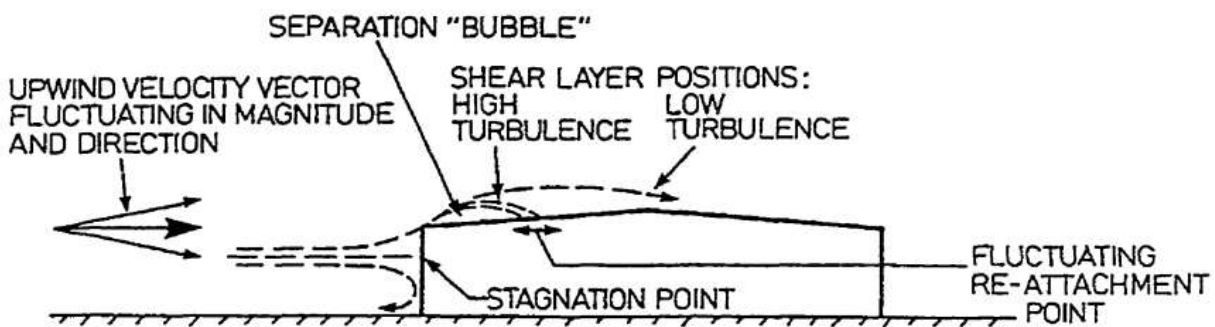


Figure 2-3. Formation of a separation bubble on a sloped roof (Wang 1998)

On the other hand, conical vortices are developed at the windward corner under a cornering (oblique) wind, a wind flowing at an acute angle to the roof edge (Banks et al. 2001). As shown in Figure 2-4(a), conical vortices, also known as delta wing vortices, are formed in pairs along the windward roof edges (Cook 1985). The flow separated at the edge has a velocity component along the separation line. Since the vorticity of the corner upwind flow under the shear layer is transferred and added to the vorticity of the downwind flow under the shear layer, a circulating conical vortex is developed. The formation occurs along the roof edge and the circulation of the vortices; consequently, the size of the shear layer increases as it moves along the roof edge. Localized high negative pressure develops under each radial centerline, shown as pressure lobes in Figure 2-4(b). The conical vortex has primary and secondary vortices under the same shear layer (Cook 1985). High suction pressures near the roof corners occur directly underneath the conical vortex cores, and the pressure reduces drastically near the vortex reattachment point. The incident wind speed, horizontal angle of attack, and vertical angle of attack influence the negative pressure magnitude underneath conical vortices. Although, both horizontal and vertical wind angles of attack influence the position and structure of a conical vortex, the influence of the vertical angle of attack is significant for instantaneous peak suction generation near roof corners (Sarkar 2001). The ASCE 07 accounts the influence of disturbance to wind flow using the topographic factor, but it does not account for the wind angle in the vertical direction.

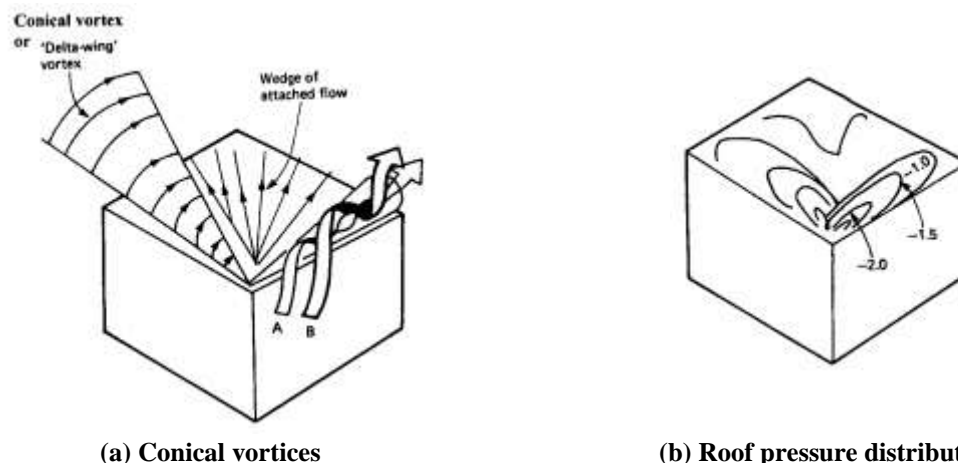


Figure 2-4. Formation of conical vortices (a) and the resulting typical pressure distribution on a flat roof (b) (Cook 1985)

The evidence collected after damaging winds supports the need of strengthening roof edges and corners to prevent damages. Figure 2-5(a) shows the roof covering damage in an apartment complex in Ocean Springs, Mississippi, during Hurricane Katrina. Figure 2-5(b) shows the detachment of a cementitious wood-fiber deck panel in a school in Biloxi, Mississippi, due to its

inadequate attachment to the support structure. These type of old wood-fiber deck panels were unable to withstand the increased uplift loads at roof edges and corners.



(a) Roof covering damage



(b) Deck panel blow off at a roof corner

Figure 2-5. Roof damages indicating high-pressure zones during hurricanes (FEMA 2006)

For this reason, the ASCE 07 divides the roof of a building into three pressure zones as Zone 1, Zone 2, and Zone 3. These regions may differ based on the roof angle. External pressure coefficients are specified for the three zones to calculate the wind loads on the components and claddings at each zone. As shown in Figure 1-2, Zone 3 and Zone 2 (corner and edge zones) are assigned higher external pressure coefficients compared to Zone 1 (interior zone).

2.2.1 Flow Visualization Techniques

The influence of separation bubbles and conical vortices on roof pressure distribution is studied. Flow visualization techniques such as smoke injection, tuft grids, laser sheets, surface oil flow, schlieren photography, sand erosion technique, etc., are used for observation and physical understanding of flow patterns around structures. Figure 2-6(a) shows the use of a sand erosion technique to visualize the formation of conical vortices on a flat roof under a wind direction of 45° . Figure 2-6(b) shows the use of a smoke-wire technique to visualize the streamlines formed around a cube shaped model with sharp edges under a perpendicular wind flow (90°). Figure 2-6(c) shows the use of laser sheets and a camera to capture the images of the vortex formed over a flat roof due to a 45° wind. Sarkar (2001) investigated the formation of conical vortices and the resulting roof corner pressures in full-scale buildings at the Texas Tech Wind Engineering Research Filed Laboratory (WERFL) experimental building. The conical vortex phenomenon was documented by capturing vortex images (using a video camera and a tuft grid) and measuring wind data and corner pressures (using a sonic anemometer and pressure taps).



Figure 2-6. Flow visualization techniques

2.2.2 Factors Affecting the Roof Pressure Distribution

The approach wind and building characteristics influence pressure magnitude and distribution on a building roof. The approach wind characteristics include the wind profile, freestream wind turbulence, and the wind angle (wind direction). The building characteristics include the building geometry and stiffness, building grouping (isolated or surrounded with buildings and other obstacles), along with the roof characteristics (roof type, flexibility, roof pitch/angle, and the presence of architectural or aerodynamic features).

2.2.2.1 Wind Characteristics

The approaching wind profile determines the formation of different flow patterns over a roof and the resulting wind pressure distribution. Cook (1985) studied the formation of separation bubbles under a uniform wind flow and a boundary layer wind flow. Figure 2-7 illustrates the observed flow patterns and pressure distributions over a flat roof under uniform and boundary layer flow conditions. As shown in the figure, a wind flow pattern significantly affects the resulting pressure distribution on a flat roof. Even though low-rise buildings are subjected to the atmospheric boundary layer wind flow due to their limited heights, monitoring wind flow characteristics and structural response is of paramount importance to develop realistic loads for design, assessment, and real-time response of roofing systems. In an era when we are focusing on developing smart structures that are equipped with artificial intelligence (AI) driven technologies, having access to large databases is necessary to develop roofing systems that will respond in real-time to wind loads to minimize the effect of damaging loads. This can be accomplished by incorporating dampers and smart material into the roofing assembly or the building structural system.

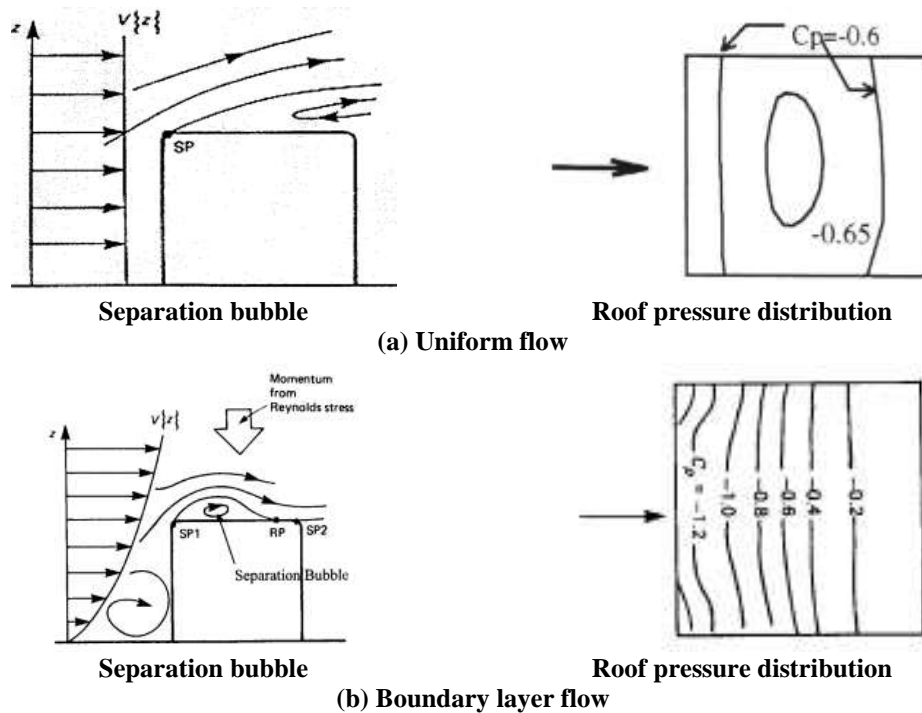


Figure 2-7. Separation bubbles and pressure distribution on a flat roof under uniform flow (a) and a boundary layer flow (b) (Cook 1985)

Note: SP: Separation point, RP: Reattachment point, z : height, $V\{z\}$: Wind velocity with respect to height, C_p : Pressure coefficient.

Lin et al. (1995) studied the variation of wind pressure distribution at windward roof corners by changing the wind direction on scale models of low-rise buildings (same base dimensions but different heights) under a smooth, boundary layer flow. Figure 2-8 shows the peak pressure coefficients (C_p) observed at the windward roof corner on one of the models. The C_p distribution at the windward roof corner for all tested models was similar with only the magnitude being different for each case. It is clear that, irrespective of the wind direction, high suction pressures occur at the windward corner; however, they rapidly decrease with the distance away from the corner. The wind direction that resulted in the highest suction depends on the model geometry (height) and the wind characteristics (smooth or turbulent). Özmen and Baydar (2016) conducted wind tunnel testing of three gable-roof buildings to evaluate the impact of roof pitch and wind direction on the roof pressure distribution. The study included several wind directions and three roof pitches: 15° , 30° and 45° . The results showed that the critical wind direction is 15° from the windward roof corner, irrespective of the roof pitch.

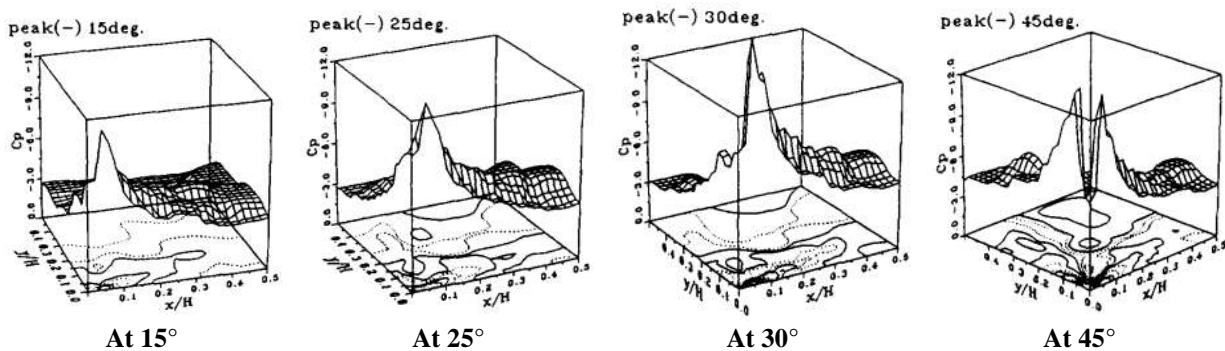


Figure 2-8. Peak roof pressure coefficient variation with wind direction (Lin et al. 1995)

Wu et al. (2000) showed that most of the pressure fluctuations on a building envelope were caused by longitudinal and lateral turbulence. Kawai (1997) studied the structure of conical vortices formed on a flat roof under oblique winds in smooth and turbulent flows. This study revealed that the strength of conical vortices is larger in smooth flows than in the turbulent flows. As a result, higher suction pressures were developed on the roof under a smooth flow.

2.2.2.2 Building Characteristics

Building structural and geometric characteristics affect roof wind pressure distribution. Gerhard and Kramer (1992) conducted wind tunnel testing to evaluate the influence of building geometry on roof loads. They used building models of constant height but varying height-to-width ratios (0.4 to 0.04). The models were subjected to three different boundary layer flows. The flow patterns were visually observed using a sand erosion technique; i.e. distributing sand over the roof and observing the displacement of sand under the wind flow. The borderline between differently shaded areas shown in the sand erosion pictures and lines of constant velocity (isotachs) were drawn to obtain the corresponding isotach diagrams. For all the models, the time averaged roof pressures were determined, and the isobar diagrams (lines of constant pressure) were obtained. Figure 2-9 shows the isobar diagrams for two models with relative height (height/width) of 0.4 and 0.04. The variables B , L , and h represent width, length, and height of the model. Localized high-pressure zones observed at roof corners and edges are shown in Figure 2-9. Since height and width/length ratio were maintained as constants, results primarily indicate the impact of building plan dimensions on pressure distribution. The results show that the area percentage under large suction at corners and edges increases with the decrease in plan dimensions. As an example, the region with $C_p = -1.5$ of $h/B = 0.4$ extends up to 37.5% of the building width, whereas it is only 6.5% when $h/B = 0.04$. Hence, the high negative pressure region at a roof corner is a function of the building plan dimensions. As shown in Figure 2-10, the ASCE 07 defines the width of this

high pressure zone along an edge as 'a', which equals the smaller of 10% of the least horizontal dimension or 0.4h. However, 'a' has to be greater than 4% of the least horizontal dimension or 3 ft. As per the ASCE 07, the corner zone length is 2a. According to Gerhard and Kramer (1992), for narrow structures (i.e., with larger h/B ratios), the ASCE 07 limits for high suction corner regions might not be adequate to prevent corner damages due to wind uplift.

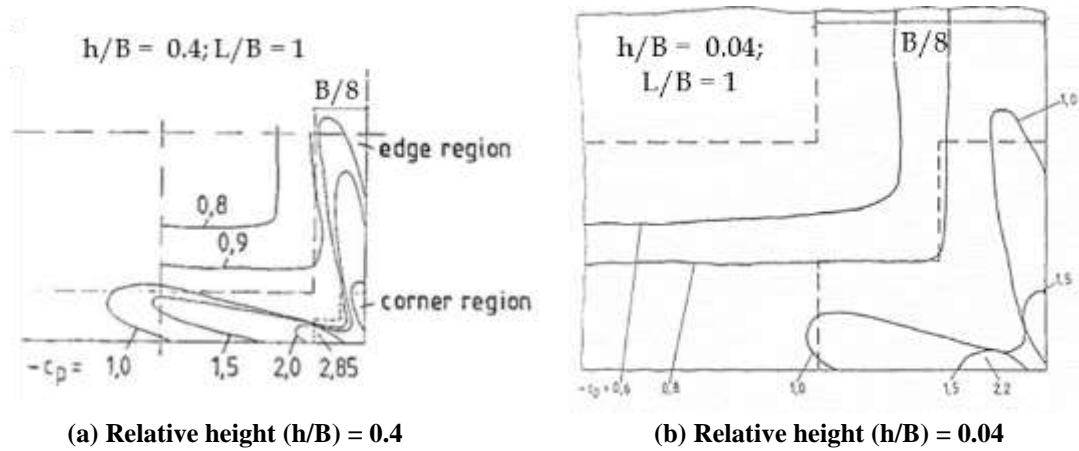


Figure 2-9. Isobar diagrams (Gerhardt and Kramer 1992)

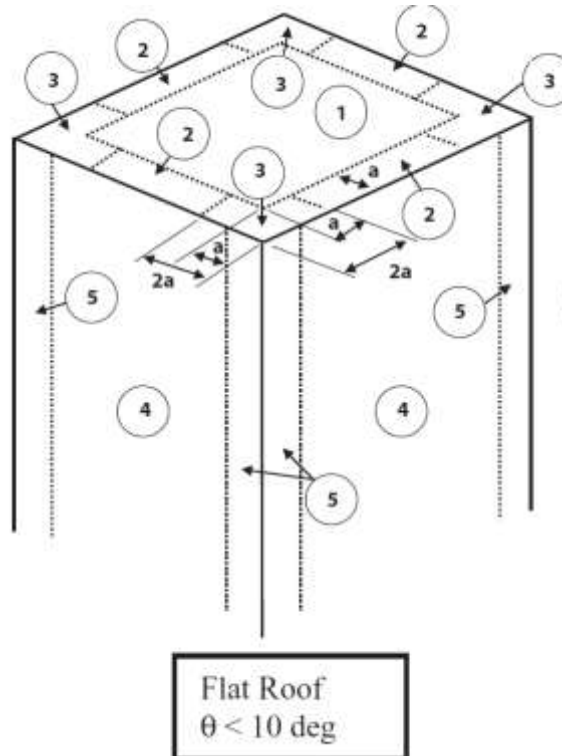


Figure 2-10. ASCE 07 definitions of flat roof wind pressure zones

In comparison to the wind pressure distribution on an isolated building, the presence of neighboring structures (building grouping) alter the flow patterns and the wind induced pressure

distribution. The significance of such interferences depends on the geometry and arrangement of the buildings (i.e., the orientation with respect to the wind direction and the upstream conditions) (Khanduri et al. 1998). Surry and Lin (1995) investigated the influence of different building grouping densities on the behavior of the vortices at roof corners and the roof pressures on a flat roof. The results showed that the presence of surrounding buildings generally reduced the roof suction, with a reduction of 50 – 65% of the mean C_p occurring at the roof corners. Pindado et al. (2011) performed wind tunnel testing to study the interference effect caused by an upstream building on a flat roof of a downstream low-rise building. Pindado's study focused on four different relative building heights (height of the upstream building/height of the downstream building): 1, 1.5, 2, and 3. The study also investigated six different relative distances between the two buildings (distance between the two buildings/height of the downstream building): 0, 0.5, 1, 2, 3, and 4 were considered under different wind directions. The experimental results showed that the presence of an upstream building amplified the wind load on the flat roof of a downstream building. Further, wind load on the roof increased with the elevation in relative height of the buildings with the maximum increase observed when the relative distance between buildings was 1.0. Li et al. (2017) numerically investigated the wind pressure distribution on a gable roof building under wind interference effects caused by a group of buildings. Analysis parameters included various low-rise building arrangements (parallel, tandem, staggered), distances between buildings, and wind directions. The Reynold's Stress Model (RSM) was used for numerical simulation, and the results were verified using wind tunnel test data. The tandem arrangement produced the greatest wind interference effects on a building followed by the staggered and parallel arrangements. The roof of the building located at the corner of a group experiences the largest interference effects, irrespective of the group arrangement.

In addition, roof geometry (flat, gable, hip, spherical, etc.), roof pitch, and the presence of aerodynamic features/devices all affect the wind loads acting on a low-rise building roof. Figure 2-11 illustrates the impact of roof geometry (gable, hip, and pyramidal) on wind uplift forces. The gable roof experiences the highest uplift while pyramidal roof experiences the lowest uplift under the same wind conditions (Keote et al. 2015).

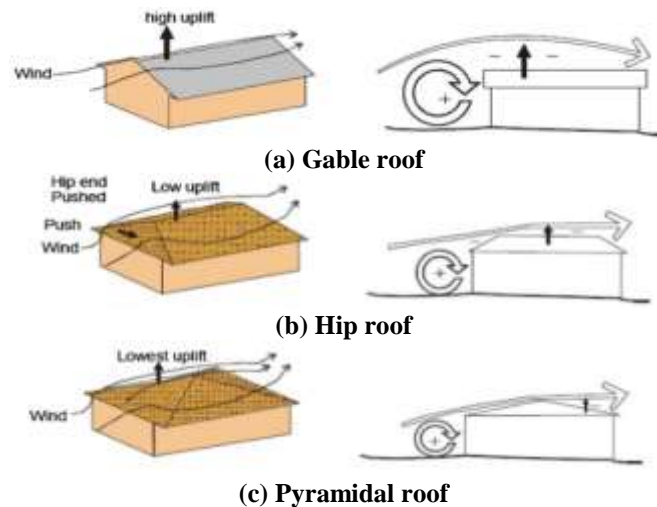


Figure 2-11. Impact of roof geometry on wind uplift forces (Keote et al. 2015)

Cook (1985) studied the effect of the roof pitch on wind flow separation and the location of reattachment by evaluating the mean flow streamlines around pitched roofs. As shown in Figure 2-12, with the increase in roof pitch, the flow reattachment position moved towards the windward edge of the roof with no flow separation observed at 45° . Also, the roof pitch of 45° resulted in a downward pressure.

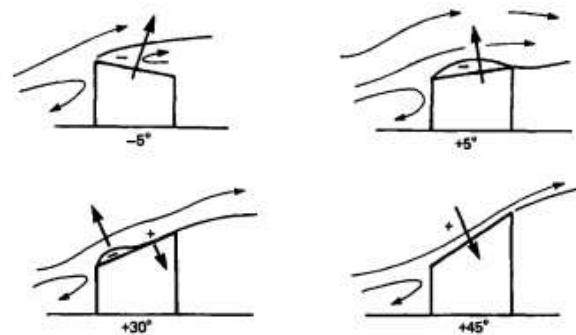


Figure 2-12. Effect of roof pitch on wind flow patterns (Cook 1985)

Meecham (1992) conducted boundary layer wind tunnel (BLWT) testing using scaled models of 4:12 and evaluated the performance of hip and gable roof buildings. Wind direction increments of 10° under different wind environments (open country and suburban) were considered, and the spatial distribution of the mean pressure coefficients were calculated. Compared to the gable roofs, the hip roofs exhibited increased wind resistance. Barnaud et al. (1974), as reviewed by Wang (1998), indicated the roof wind loads as a function of roof pitch by examining the mean and root mean square (rms) pressures on three different roof pitches: 0° , 22.5° and 45° . High negative pressures were observed at the corners and edges of flat roofs, which decreased on the 22.5° sloped roof and disappeared on the 45° sloped roof. Vickery (1976), as

reviewed by Wang (1998), evaluated the pressure variation on gable roofs by studying pressure distribution due to roof pitches of 0° , 6° , 12° and 22° . On 0° and 6° sloped roofs (nearly flat roofs), flow separation occurred at the leading edge. However, the flow reattached and remained attached over the ridgeline until the trailing edge. On 12° sloped roofs, the flow separated at the leading edge, reattached on the windward slope and then re-separated at the ridgeline before reattaching on the leeward slope. The flow behavior of 22° roofs was similar to that of a 12° roof, except for no flow reattachment within the leeward slope. Xu and Reardon (1998) conducted wind tunnel testing of hip roof buildings with 15° , 20° and 30° pitches to evaluate the effect of roof pitch on wind pressure distribution. When the results were compared with gable roofs of similar geometry, both gable and hip roofs with 30° roof pitch exhibited similar peak suction (at roof corners). However, hip roofs with roof pitches of 15° and 20° exhibited lesser peak suction compared to the similar gable roofs. The experimental results indicated that the roof pitch affects the magnitude and the distribution of wind pressure on a hip roof. Prasad and Ahmed (2009) performed wind tunnel testing of low-rise buildings with flat, gable and hip roof configurations using a BLWT. All three building types had the same height, but the roof pitches of gable and hip roofs were 15° , 20° , 30° and 45° . The variation of minimum roof pressure coefficients is illustrated in Figure 2-13. The flat roof recorded the highest suction pressure. The gable and hip roofs with a pitch of 45° showed reduction in the peak suction pressures by 85% and 91% when compared with flat roof pressure. Similarly, hip roof peak suction pressure was 42% lower than the gable roof pressure. Özmen and Baydar (2016) used gable roof building models with roof pitches of 15° , 30° and 45° to evaluate the effect of roof pitch on the external wind pressure distribution. At a 15° wind angle, the highest suction pressure was observed at the roof corners, and the suction pressure decreased with the increase in roof pitch.

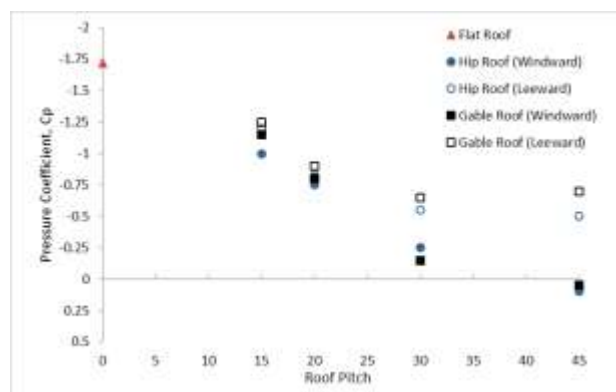


Figure 2-13. Variation of the minimum pressure coefficient over gable, hip, and flat roofs (Prasad and Ahmed 2009)

Enteria (2016) studied the behavior of typical roofing designs in the Philippines (flat, gable with and without overhangs, pyramidal with and without overhangs, vaulted, wedged, and domed) under typhoon wind conditions. The OpenFOAM solver was used for the CFD simulation performed for this study to identify different flow fields, pressure coefficients on building surfaces, and streamline patterns under different wind directions. The occurrence of different flow phenomena changed with the roof design; the occurrence of flow separation on a flat roof was at the leading edge of the roof, whereas the flow separation of a gable roof was at the top of the roof. In vaulted and domed roofs, a little recirculation occurred on the roof. In the wedged roof, flow separated at the top of the roof while the flow recirculation occurred in the leeward area. The flow separation on the pyramidal roof was similar to that of the gable roof. Figure 2-14 illustrates the numerical simulation results for the flow streamlines around different shaped roof designs.

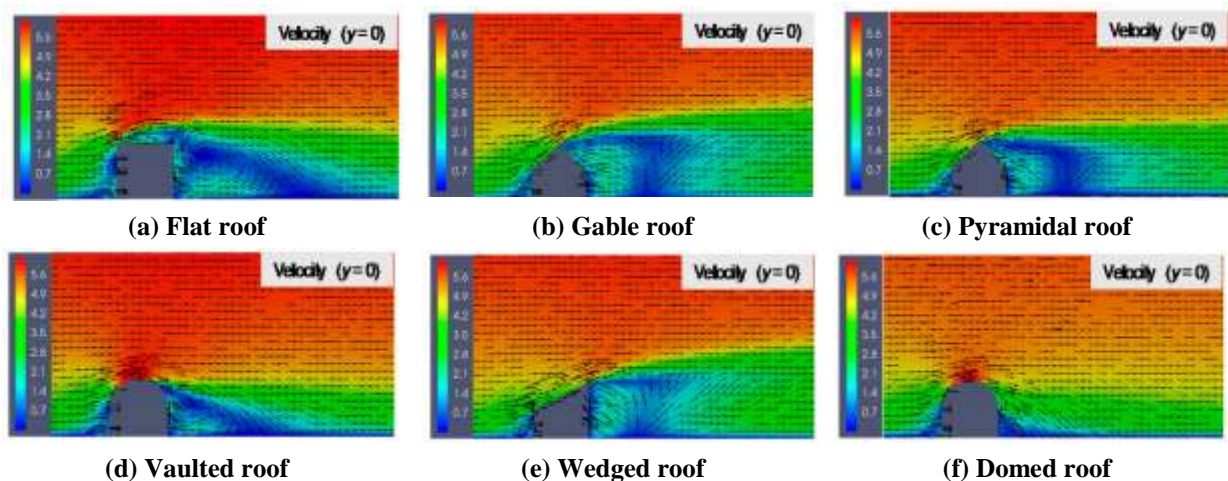


Figure 2-14. Velocity streamlines around buildings with various roof designs (Enteria 2016)

Singh and Roy (2019) conducted CFD simulations to evaluate the effect of roof pitch and the wind direction on the wind pressure distribution over a pyramidal roof of a low-rise building with a square plan. The roof pitch ranged from 0° to 30° in 10° intervals. The wind incident angle ranged from 0° to 75° in 15° intervals. Overall, the highest and the lowest negative pressures were observed on 10° and 20° sloped roofs, respectively. The highest pressure on 0° and 30° sloped roofs were average and similar (Figure 2-15(a)). As shown in Figure 2-15(b), the maximum pressure coefficient changed with respect to the wind direction and roof pitch. Out of the four surfaces of the pyramidal roof, the surface perpendicular to the wind direction experienced higher wind pressures. When the wind direction was perpendicular to an edge between two surfaces, the wind pressure on the entire roof was minimum.

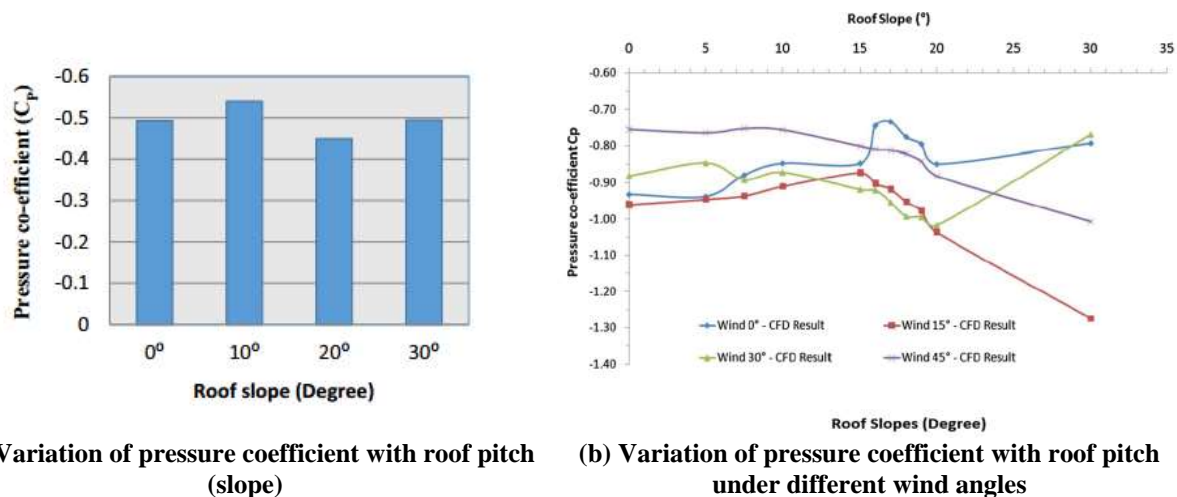


Figure 2-15. Effect of roof pitch and wind angle on the pressure distribution on a pyramidal roof (Singh and Roy 2019)

2.3 WIND SUCTION MITIGATION FEATURES AND DEVICES FOR FLAT AND STEEP SLOPED ROOFS

In addition to the roof slope and the roof shape, presence of aerodynamic features/devices affect the wind pressure distribution on a roof. Parapets, spoilers, eave configurations, overhangs, rounded roof edges, chamfered roof edges, etc., are a few commonly used aerodynamic features on low-rise buildings. The wind pressure patterns on a roof depend on the geometry of such features, location of such features on a roof, and wind characteristics. As a result, the use of such features/devices as possible wind damage mitigation techniques is studied.

2.3.1 Roof Geometry Modifications

Wind flow patterns around bluff bodies are greatly influenced by their shape. Since straight and sharp edges separate the flow creating vortices to develop high negative pressure regions, roof edge details are modified to reduce the resulting aerodynamic load (Surry and Lin 1995). Chamfered or rounded edges are used to reduce the extent of separation bubbles along with the negative pressure magnitude and distribution (Surry and Lin 1995).

2.3.1.1 Experimental and Numerical Studies on Roof Geometry Modification

Blackmore (1988) conducted BLWT testing to investigate the effects of roof edge chamfers with 30°, 45° and 60° slopes on flat roof wind pressure distribution. Figure 2-16 shows the model geometry and the locations of the roof top pressure taps. The wind directions were 0°, 15°, 30°, and 45°. The chamfered edges reduced the wind loads, and the largest reduction was observed at the roof corners. The chamfers with the lowest slope yielded the largest reduction. The chamfered edge with a slope of 30° reduced the wind load at a leading roof corner by 70%. The overall

reduction of the wind pressure load on the roof due to this 30° chamfered edge was 34%. Steep chamfers generally reduced the corner suctions but increased the load at the windward edge (Blackmore 1988).

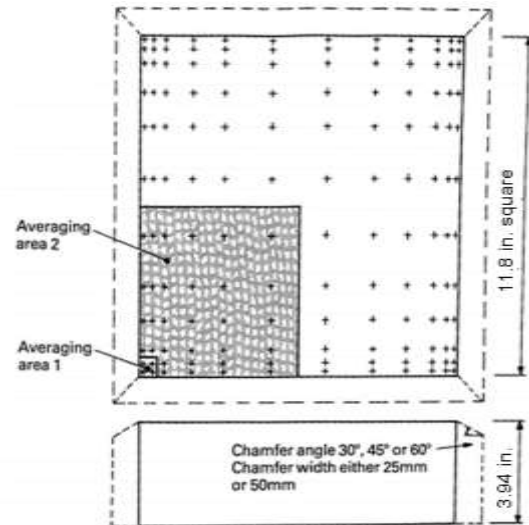
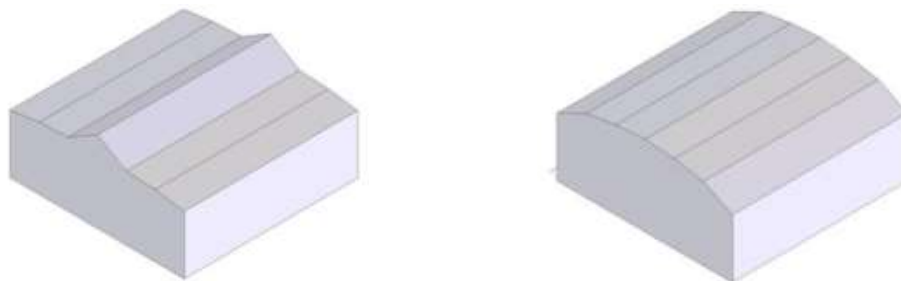


Figure 2-16. Model geometry and pressure tap locations on the roof (Blackmore 1988)

Sehn (2008) investigated two aerodynamically modified roof shapes. As shown in Figure 2-17, the roof geometries were identified as Variably Increasing Sloped Roof (VISR) and Variably Decreasing Sloped Roof (VDSR). The slopes of the VISR were set to 8°, 0° and 30°. The slopes of the VDSR were set to 26°, 10° and 4°. The VISR configuration was developed to lower the flow separation occurring at the leading edge by creating a valley on the roof. The slopes in VDSR were to mimic the streamline flow in order to reduce the pressure gradient that creates flow separation. The performance of these roof shapes was compared with gable and hip roofs by considering the uplift force coefficients. An average performance index representing all the building orientations was calculated for each roof shape and compared with the performance of the gable roof model. The VISR yielded the largest average performance index of 14.3% reduction in uplift. The VDSR or the hip roof models showed no significant reductions in the uplift.



(a) Variably increasing sloped roof (VISR) (b) Variably decreasing sloped roof (VDSR)

Figure 2-17. Aerodynamically modified roof geometries (Sehn 2008)

Mahmood et al. (2008, 2011) conducted wind tunnel testing on 1:100 scaled models to evaluate the effect of sharp and rounded edges on roof wind suction. Four different rounded edges with radii (r) as 0 in. ($r/h = 0$ -sharp edge), 0.197 in. ($r/h = 0.125$), 0.315 in. ($r/h = 0.2$), and 0.394 in. ($r/h = 0.25$) were tested. Four different flow conditions (smooth flow, barrier flow, nominal boundary layer flow with 4% turbulence, and boundary layer flow) were used to find the optimum radius of the rounded edge to minimize roof suction. Laser light illumination and smoke-wire techniques were used to observe vortex formation and flow separation. Figure 2-18 shows separation flow due to sharp and rounded edges. As shown in Figure 2-18(a), the 90° flow separates at the sharp leading edge with a large recirculation bubble and descends to form a ground vortex. The 90° flow shows a smooth separation at the rounded edge with relatively less height in the separation bubble. Similar flow patterns are observed under the 45° wind direction as shown in Figure 2-18(b). In addition, the impact of the rounded edge size was investigated under 25° wind direction for radii 0.197 in. ($d/h = 0.125$) and 0.394 in. ($d/h = 0.25$). The wind flow patterns around the models were observed using the smoke-wire technique. Figure 2-19 shows the flow patterns observed over the sharp edge model and the two rounded edge models. The results support avoiding sharp edges and implementing rounded edges to reduce negative pressure on the roof. Since the height of the separation bubble reduces in proportion to the radius of the rounded edge, additional testing needs to be conducted to determine the practically feasible sizes for prototypes.

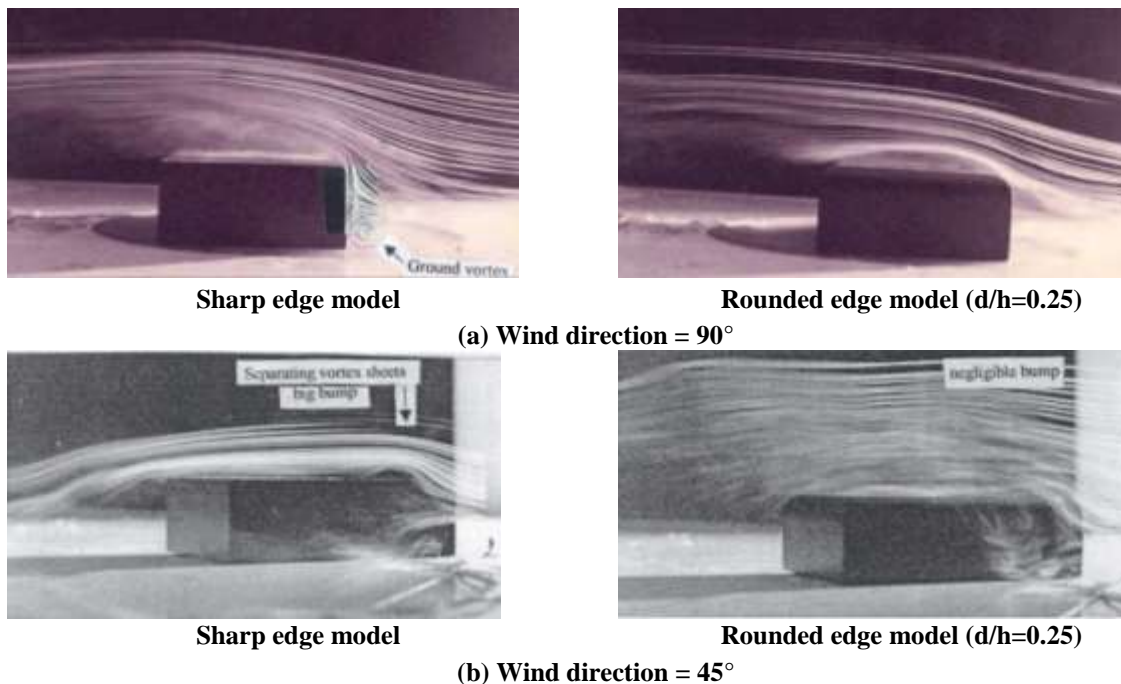


Figure 2-18. Flow separation in the presence of sharp and rounded edges under two wind directions: 90° (a) and 45° (b) (Mahmood 2011)

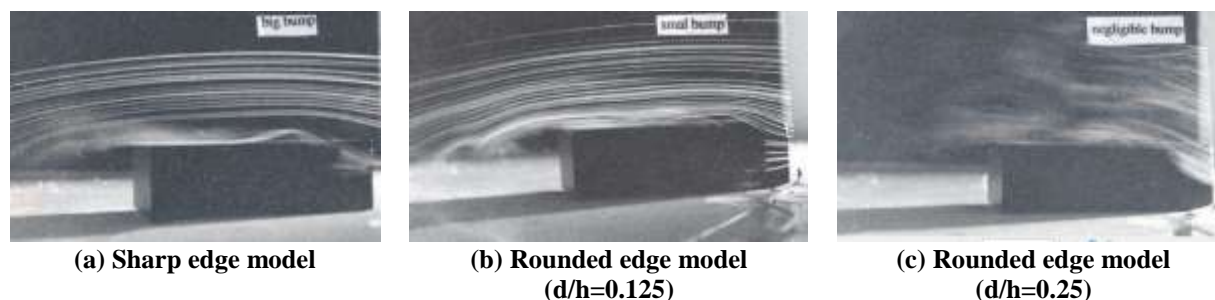


Figure 2-19. Flow separation in the presence of sharp and rounded edge models under a 25° wind direction (Mahmood 2011)

Aly and Bresowar (2016) performed CFD simulations to explore the effectiveness of rounded, chamfered and recessed roof edges. A 1:22 scaled flat roof building model under a wind direction of 45° was used. Figure 2-20 shows the geometries. The results of the modified roof geometries were compared with a sharp edge roof. The numerical results were partially validated by testing a 1:22 scale model of a flat roof building with a sharp edge.

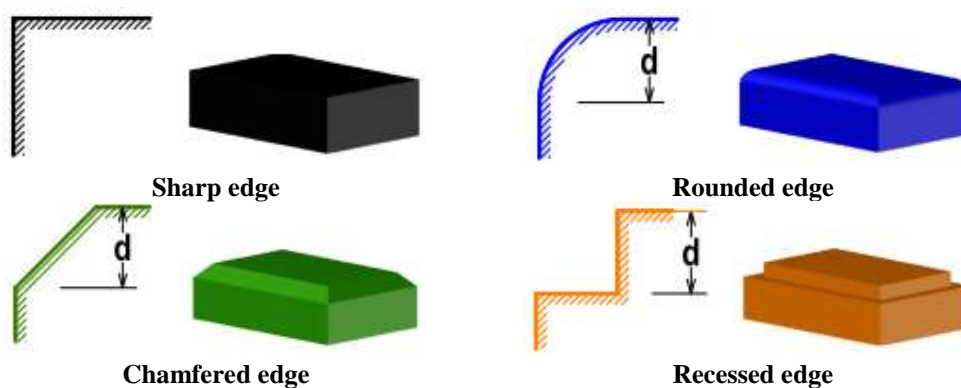


Figure 2-20. Roof edge modifications (Aly and Bresowar 2016)

The size of corner adjustment (d) was defined as a fraction of the building height (h) - small ($d/h = 0.08$), medium ($d/h = 0.16$), and large ($d/h = 0.24$). The drag and lift coefficients were calculated and used as the criteria for comparing the effectiveness of different geometry modification techniques. Table 2-1 shows the drag and lift coefficients calculated for the sharp corner and three corner modifications. Further, the modified corners of different sizes were recommended by comparing the percentage reduction or the increase in the drag and lift coefficients with respect to the sharp edge.

Table 2-1. Effect of Edge Modifications on the Aerodynamic Drag and Lift Force Coefficients on a Flat Roof Building under a Wind Angle of 45° (Aly and Bresowar 2016)

Corner	Size	Drag and Lift Coefficients		Recommendation
		C_d	C_l	
Sharp	-	1.02	1.33	-
Chamfer	small	0.81 (-23.6%)	1.34 (+0.8%)	No
	medium	0.76 (-28.3%)	1.31 (-7.5%)	Yes
	large	0.75 (-29.2%)	1.24 (-12.0%)	Yes
Rounded	small	0.78 (-12.3%)	1.50 (+12.8%)	No
	medium	0.76 (-15.9%)	1.45 (+9.0%)	No
	large	0.72 (-18.9%)	1.35 (+1.5%)	No
Recessed	small	0.87 (-17.9%)	1.26 (-5.3%)	No
	medium	0.85 (-19.8%)	1.22 (-8.3%)	Yes
	large	0.82 (-22.6%)	1.15 (-13.5%)	Yes

Dong et al. (2019) conducted wind tunnel testing to study the wind loads on a flat roof of a low-rise building with rounded leading edges. Three models were tested: one with a sharp edge (FM 1) and the other two with rounded edges (FM 2 and FM 3) of radii 0.984 in. (25 mm) and 1.378 in. (35 mm), respectively. The plan dimensions of the model were 23.6×23.6 in. (600×600 mm). The impact of wind direction was evaluated by considering the variation of wind direction from 0° to 45° in five intervals. The 0° wind direction is considered as the wind flowing perpendicular to the leading edge. The roof suction due to separation bubbles and conical vortices, in the presence of the rounded leading edges, was the main focus of this study. The mean pressure distributions with wind direction 0° and 45° are shown in Figure 2-21. The results showed that for flat roofs with rounded leading edges, suction induced near the edge were increased but decreased beneath the vortices. The roof suction decreased when the radius of the leading round edge was increased. The reduction of the total uplift force on the roof was most effective under skewed flows. The fillet radius had a noticeable influence on the fluctuating suction. The sum of the mean square pressure fluctuation for the flat roofs with a leading edge of radius 1.378 in. ($d/h = 0.175$) was reduced by 66% and 86% under the separation bubble and conical vortices, respectively. In addition, both peak total uplift force and the overturning moments decreased. The overturning moment decreased with the increase in the radius of the leading edge. However, a direct relationship between the fillet radius and the total peak uplift forces was not observed.

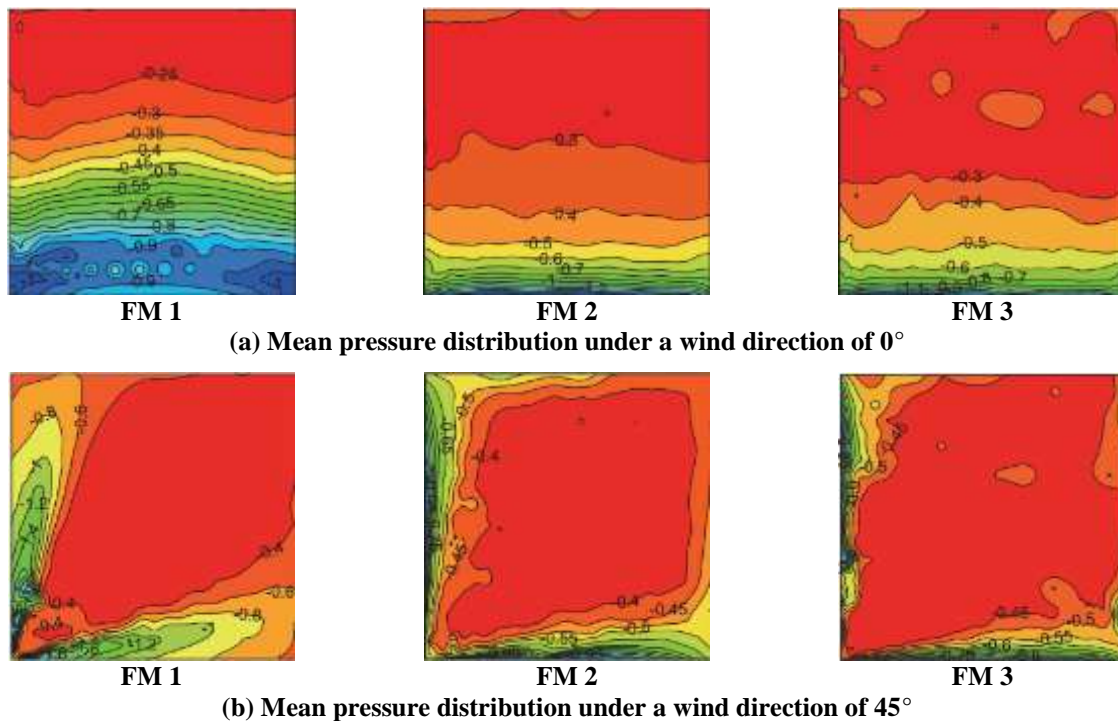


Figure 2-21. Mean pressure distribution under wind directions 0° and 45° (Dong et al. 2019)

2.3.2 Architectural Aerodynamic Features/Devices

Unlike geometric modifications of existing roofs, the use of architectural aerodynamic features/devices involves adding new components at the roof level to control pressure distribution by altering the flow patterns. The expectation is to disrupt the formation of vortices and/or disturb and displace the formed vortices to reduce the suction load (Surry and Lin 1995). Since such components are also subjected to wind loads, the design needs to account for the loads acting on such components, connections, and the structure.

Solid parapets are conventional architectural features that alter wind suction pressure near the perimeter. Solid parapets at roof eaves displace the vortices from the roof edges, thereby reducing the suction on the edges and corners (Lstiburek 2012). Figure 2-22 illustrates the reduction of the high pressures at roof edges and corners with the incorporation of parapets into the roofs. Experimental work on flat roofs with solid parapets showed reduction in the high suction pressures on roof edges but a slight increase of suction pressures at roof interior (Stathopoulos and Baskaran 1987). Figure 2-22(b) and (c) show the impact of parapet height on pressure distribution. Based on parapet height (h_p) to building height (h) ratio, parapets are classified as tall ($h_p/h > 0.08$), intermediate ($0.04 < h_p/h < 0.08$), and low ($h_p/h < 0.04$). A tall parapet displaces vortices vertically to reduce peak suction pressure, while a low or intermediate parapet promotes

the development of vortices at roof corners; thus, resulting in higher peak suction pressures at roof corners compared to a structure without parapets (Bienkiewicz and Sun 1992, Cochran and English 1997).

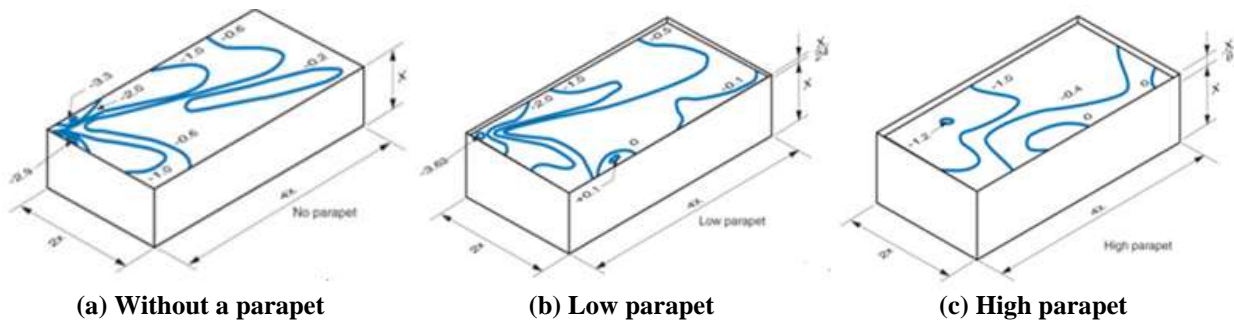


Figure 2-22. Impact of parapets on roof pressure distribution (Lstiburek 2012)

Since tall parapets develop additional dead and wind loads, partial parapet configurations with additional features are considered (Figure 2-23). The alternatives considered include introducing slots at the lower half of the parapet at roof corners (slotted parapets), placing a partial parapet at a small distance away from roof corners (discontinuous parapets), increasing parapet height at roof corners (raised parapets), and using castellated parapets. Although discontinuous parapets reduce loading on the roof compared to solid parapets, they failed to reduce the corner suction pressure that develops on roofs with no parapets.

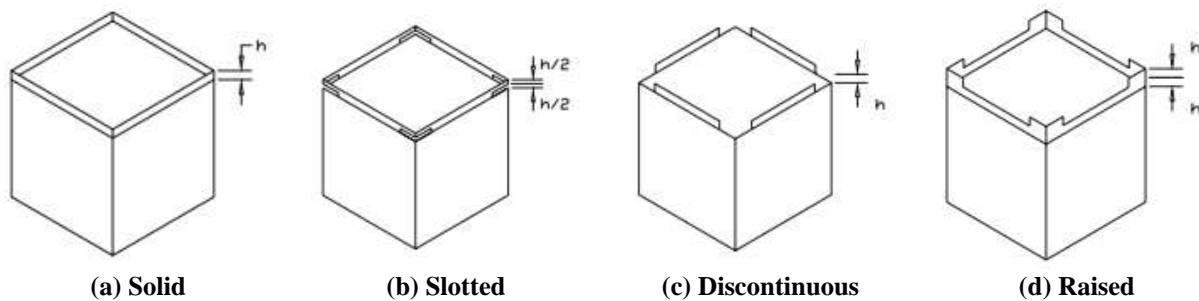


Figure 2-23. Parapet configurations for altering wind flow over roofs (Kopp et al. 2005)

Pindado et al. (2009) present several alternatives to typical solid parapets. They are porous parapets, slotted parapets, isolated parapets (parapets running along the edge of one wall), and cantilever parapets (also called parametric spoilers). The porous and slotted parapets introduce small-scale turbulence over the roof to disrupt vortex formation. The cantilever parapets stretch and deflect the core of the conical vortex from the roof corner to a higher point on the roof. Figure 2-24 shows the influence of three parapet configurations on the formation of vortices over a flat roof.

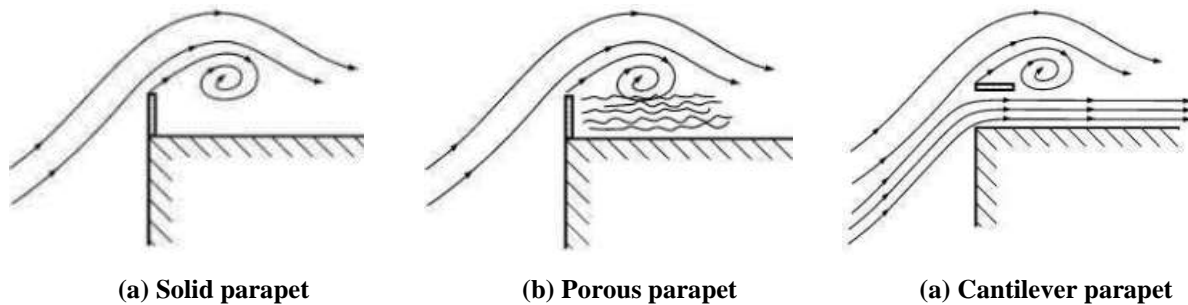
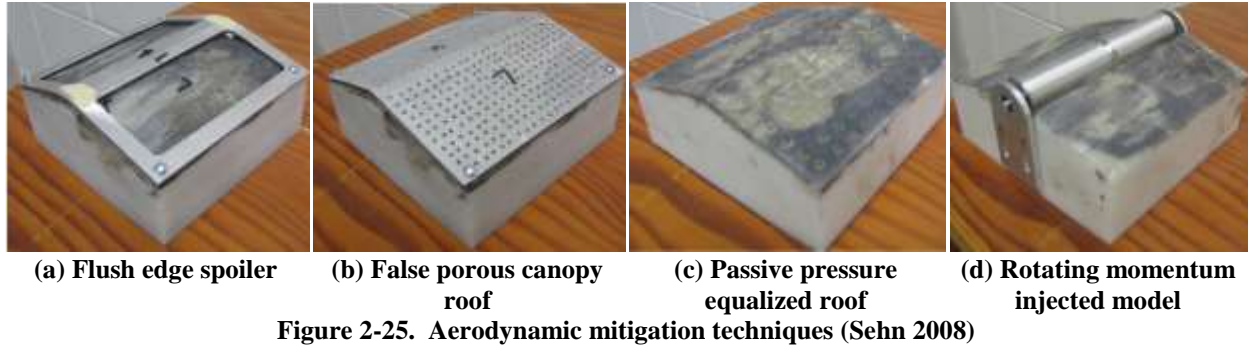


Figure 2-24. Influence of parapet configuration on the vortex formation (Pinando et. al 2009)

As shown in Figure 2-25, several other alternatives are presented in literature. The edge spoiler, shown in Figure 2-25(a), creates a high-pressure zone in front of the spoiler and a low-pressure zone behind the spoiler. In the presence of a pressure gradient, the flow is directed underneath the spoiler into the roof vortex formed above the spoiler. The direction of this flow is opposite to the direction of the vortex direction, which causes an overall reduction in the vortex strength (Sehn 2008). False porous canopy roofs, shown in Figure 2-25(b), allow the air flow through the internal space between the false roof and the actual roof. This creates a positive pressure underneath the top surface that partially reduces the negative pressures on the roof top surface (Sehn 2008). Passive pressure equalization methods, shown in Figure 2-25(c), are employed on roofs by connecting the windward side of a roof to the leeward side through pressure tubing; hence reducing the large suction on the leeward side (Sehn 2008). However, both false porous canopy roofs and pressure equalization methods have practical considerations with construction, implementation and maintenance.

A majority of aerodynamic devices discussed so far are stationary, passive devices. In contrast, certain studies have proposed active devices such as the rotating momentum injected model shown in Figure 2-25(d) (Sehn 2008) or wind turbine systems (Chowdhury et al. 2019). The rotating cylinder mounted at the roof ridge controls the boundary layer separation by delaying or eliminating it. When the cylinder rotates in the direction of the freestream flow, the relative velocity between the cylinder and freestream flow is reduced. This controls the boundary layer separation. Further, the rotating cylinder adds momentum into the weak boundary layer on the leeward side of the roof, thereby accelerating the flow and reducing the wake (Sehn 2008).



2.3.2.1 Experimental and Numerical Studies on Architectural Aerodynamic Features/Devices

Leutheusser (1964) studied the effect of parapets of various heights (h_p) on block-type and cylindrical structures by testing a total of 39 different building models in a wind tunnel. The model variables were parapet height to building height ratio (h_p/h), building height to width ratio (h/B) (for block type structures), building height to building diameter (h/D) (for cylindrical structures), building width to length ratio (B/L), and the wind angle (θ). The results indicated the greatest non-uniform pressure distribution on the roofs with no parapets. Building height was established as the main parameter affecting the lift force coefficient. The critical lift force coefficient was observed under the wind angle of 0° . When the building height is low, shallower parapets with a wind angle of 45° increased the negative pressures at the windward corner of the roof. Leutheusser (1964) proposed Eq. 1 to calculate the required parapet height for a given structure to maintain a negative pressure magnitude less than twice the corresponding lift coefficients.

$$h_p/h = K(B/h)^{2.7} \quad \text{Eq. 1}$$

where,

h_p = parapet height with respect to the roof

h = building height

B = width of the building plan

L = length of the building plan

K = numerical constant; $K = 0.01$ for $B/L = 1$, $K = 0.03$ for $B/L = 0.5$

Surry and Lin (1995) investigated the effect of corner configurations on flat-roof suction. The study was limited to low-rise buildings and corner configurations including parapets, radial splitters, and cylindrical projections. Seven modified corner geometries, as shown in Figure 2-26, were tested under wind directions of 0° , 15° , 25° , 30° , 35° , 40° , and 45° . All the configurations resulted in lower suction near the windward corner and edges compared to a roof without any modifications. The porous parapets reduced corner suction up to 70%. The semi cylindrical

projection reduced corner suction by more than 60% while the splitter configurations reduced corner suction by about 60%. Out of different splitter configurations, porous splitters exhibited better performance than the solid splitters. The saw tooth parapets reduced corner suction up to 40%.

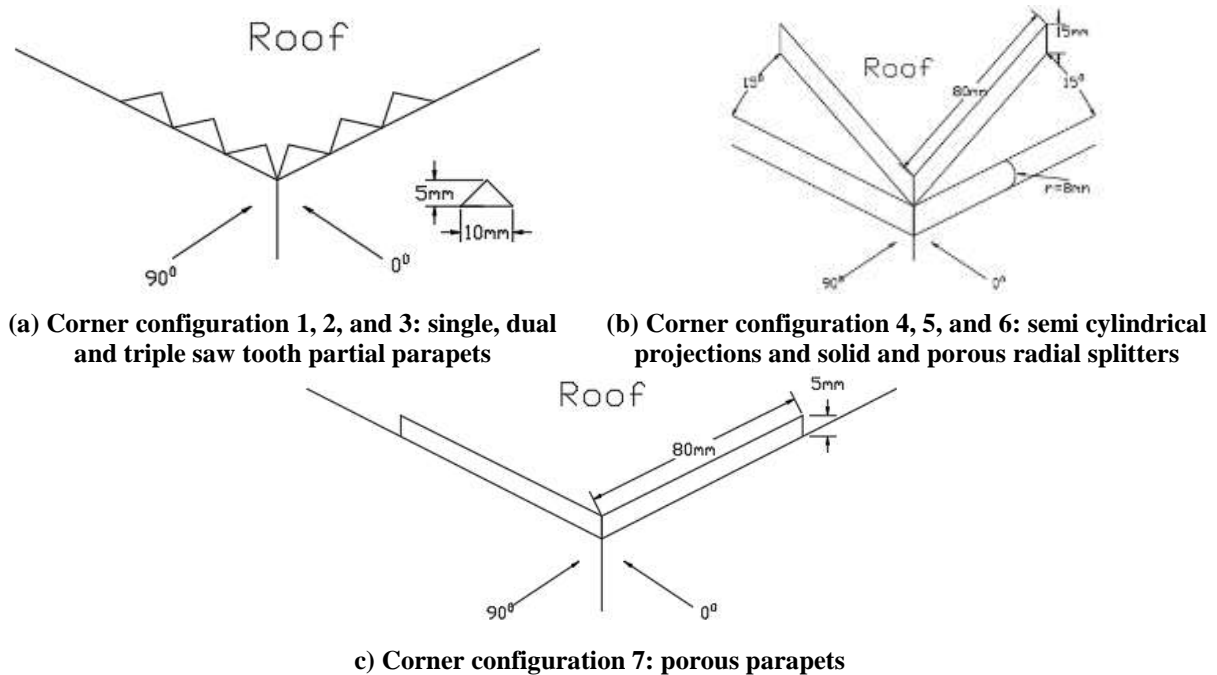
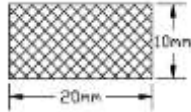
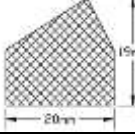
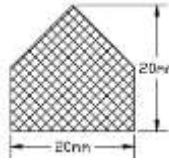
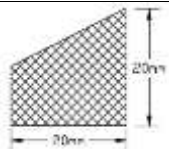
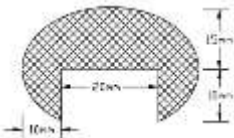
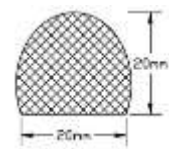
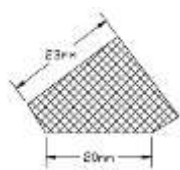
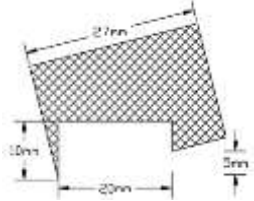
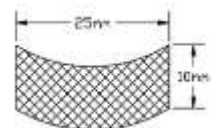


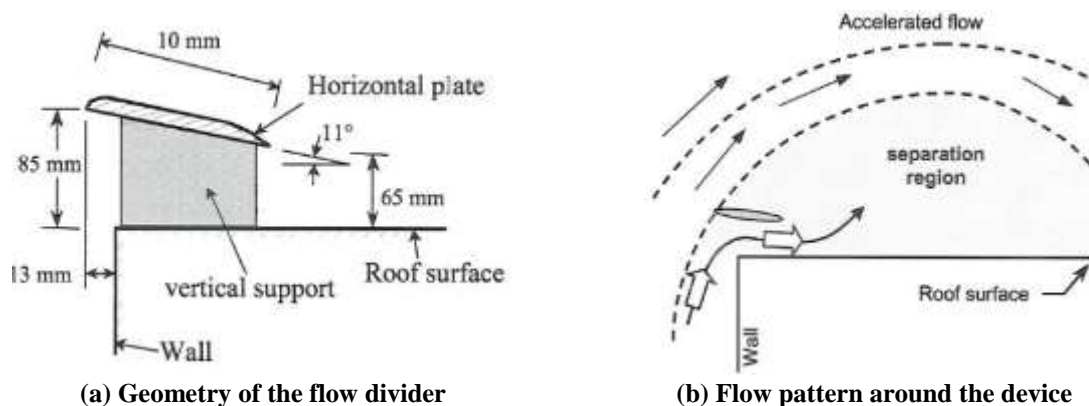
Figure 2-26. Roof corner configurations (25.4 mm = 1 in.) (Surry and Lin 1995)

Cochran and English (1997) investigated the effect of porous screens on roof corner suction. The shapes of the screens used in a 1:100 scaled flat roof model (similar to the Texas Tech University building model) placed in a wind tunnel are shown in Table 2-2. The table also shows the shape number, percent reduction in wind loads, and the effectiveness factor of each screen. The percent reduction is defined with respect to the suction at the corner of a roof without any screens. The effectiveness factor is the ratio of percent in reduction and the area factor. The area factor is the ratio between the area of each screen shape and the area of the shape represented by shape number 0. As an example, the area factor of shape number 2 is 1.5 (i.e., $300 \text{ mm}^2/200 \text{ mm}^2$), and the effectiveness factor is 20 (i.e., $30/1.5$). This effectiveness factor is used to compare the significance of each shape to reduce corner suction. As an example, shape number 4 yields the highest percent reduction, but it is the least effective shape. According to the results presented in Table 2-2, shape number 1 is the most effective porous screen for reducing flat roof corner suction. Even though such screens are beneficial to mitigate wind damage, keeping them mounted on roof tops all the time may not be aesthetically pleasing.

Table 2-2. Porous Screen Shapes and Reduction of Wind Load at Roof Corners (25.4 mm = 1 in.) (Cochran and English 1997)

Shape Number	Shape Dimensions (in 1:100 scaled models)	Percent Reduction (from no screen)	Effectiveness (Percent reduction/area factor)
0		19	19
1		35	24
2		30	20
3		30	20
4		37	11
5		35	21
6		33	20
7		33	16
8	Bent version of shape 7	35	17
9		23	19

Banks et al. (2001) evaluated the effectiveness of a flow divider mounted along the leading edge of a roof. Figure 2-27 shows the geometry of the flow divider used in a full-scale test and the flow pattern around it. The objective of this implementation was to disrupt the vortex by deflecting the shear flow layer towards the interior of the roof, thus the separation bubble.

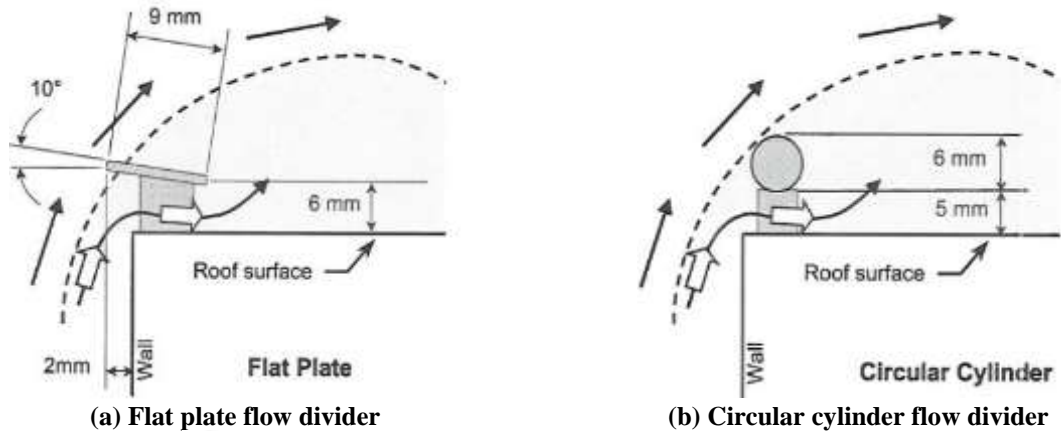


(a) Geometry of the flow divider

(b) Flow pattern around the device

Figure 2-27. Flow divider and the working principle (25.4 mm = 1 in.) (Banks et al. 2001)

Full-scale tests on a nearly flat roof building with a flow divider were conducted over a range of wind directions. Also, model scale tests were conducted in a BLWT. Two different flow dividers mounted on 1:25 scale models were used for the wind tunnel testing. The geometry of the flow dividers is shown in Figure 2-28. The variation of pressure coefficient (C_p) with respect to the angle between the leading edge of the roof and the axis of the conical vortex (ϕ) was compared with the results obtained from the models with a solid parapet, a porous parapet, and a bare roof. As shown in Figure 2-28(c), the flat plate flow divider is the most effective, followed by porous and cylindrical dividers. Banks et al. (2001) evaluated the impact of several variations of this flat plate configuration (i.e. width, angle of inclination, and the presence of overhangs or projections). All these variations reduced wind suction, and the flat plate with an overhang had the greatest influence.



(a) Flat plate flow divider

(b) Circular cylinder flow divider

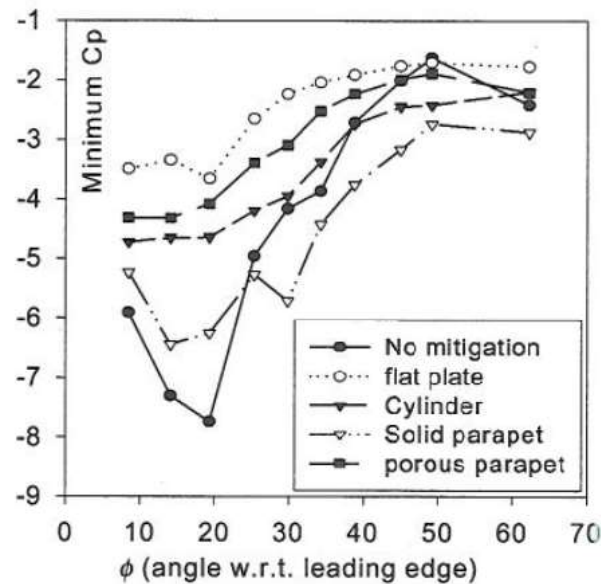
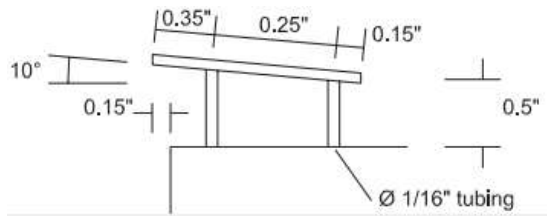
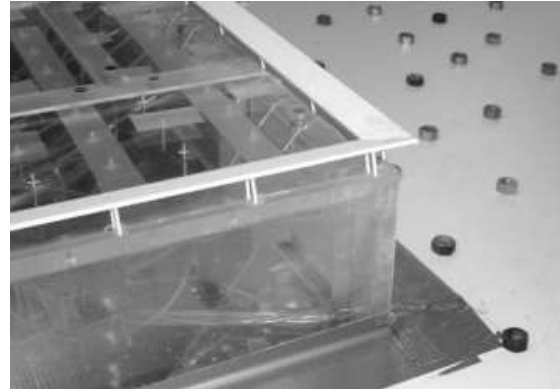
(c) Variation of minimum C_p on the roof under wind directions of 50° measured along a row of pressure taps located 5ft from the corner

Figure 2-28. Geometry of the flat plate (a), circular cylinder flow divider (b), and the variation of minimum pressure coefficients in the presence of roof suction mitigation devices (c) (25.4 mm = 1 in.) (Banks et al. 2001)

Kopp et al. (2005a, 2005b) performed BLWT testing by using 1:50 scaled gable roof building models with a slope of 1/48 to evaluate the impact of various parapet configurations to reduce the roof suction due to corner vortices. A building model with no parapet configuration was used as the reference. Eight parapet configurations involving solid parapets (perimetric), single isolated parapets (isolated, i.e. the parapet spans along one wall of the building), solid parapets with raised corners (raised parapets), discontinuous parapets (no corner), a slotted parapet (slotted corner), discontinuous parapets with 50% porosity screens at four corners (porous corner), a 50% porous perimetric parapet (porous perimeter), and perimetric spoilers (spoiler). The perimetric spoilers used in the study are shown in Figure 2-29.



(a) Details of the perimetric spoiler



(b) The test model with a perimetric spoiler

Figure 2-29. Perimetric spoiler evaluated by Kopp et al. (2005b)

Wind pressure data was collected under simulated wind conditions representing an open country terrain condition under a wind direction of 325° (nearly oblique). Figure 2-30(a) shows the definition of the wind direction with respect to the building. Figure 2-30(b) and Figure 2-30(c) show the variation of minimum pressure coefficient ($C_{p \min}$) along the building width in the presence of perimetric parapets and isolated parapets, respectively. Four different heights of perimetric and isolated parapets: 0.46 m ($h_p/h = 0.1$), 0.91 m ($h_p/h = 0.198$), 1.8 m ($h_p/h = 0.391$), and 2.7 m ($h_p/h = 0.587$) were considered. For both cases, the highest suction is observed at the leading corner, and the magnitude decreases towards the interior. When the h_p/h of a perimetric parapet is greater than 0.198, a uniform pressure distribution is observed with a relatively lower suction at the roof corner. Isolated parapets with h_p/h greater than 0.198 failed to develop a uniform pressure distribution. With continuous perimetric parapets, the vortices formed at the corner are raised above the roof surface. These vortices increase suction at the corner when the parapet height is low. Only perimetric parapets with a h_p/h of 0.587 could reduce suction lower than the case with no parapets; yet there are regions with higher suction than buildings without parapets (Kopp et al. 2005a). The performance of seven different parapet configurations under 325° wind direction is shown in Figure 2-30(d). The h_p/h used in this comparison is 0.198 (indicated as a parapet height of 0.9 m). Only the perimetric spoiler and porous perimeter parapets could successfully reduce suction lower than the level with no parapets (Kopp et al. 2005b).

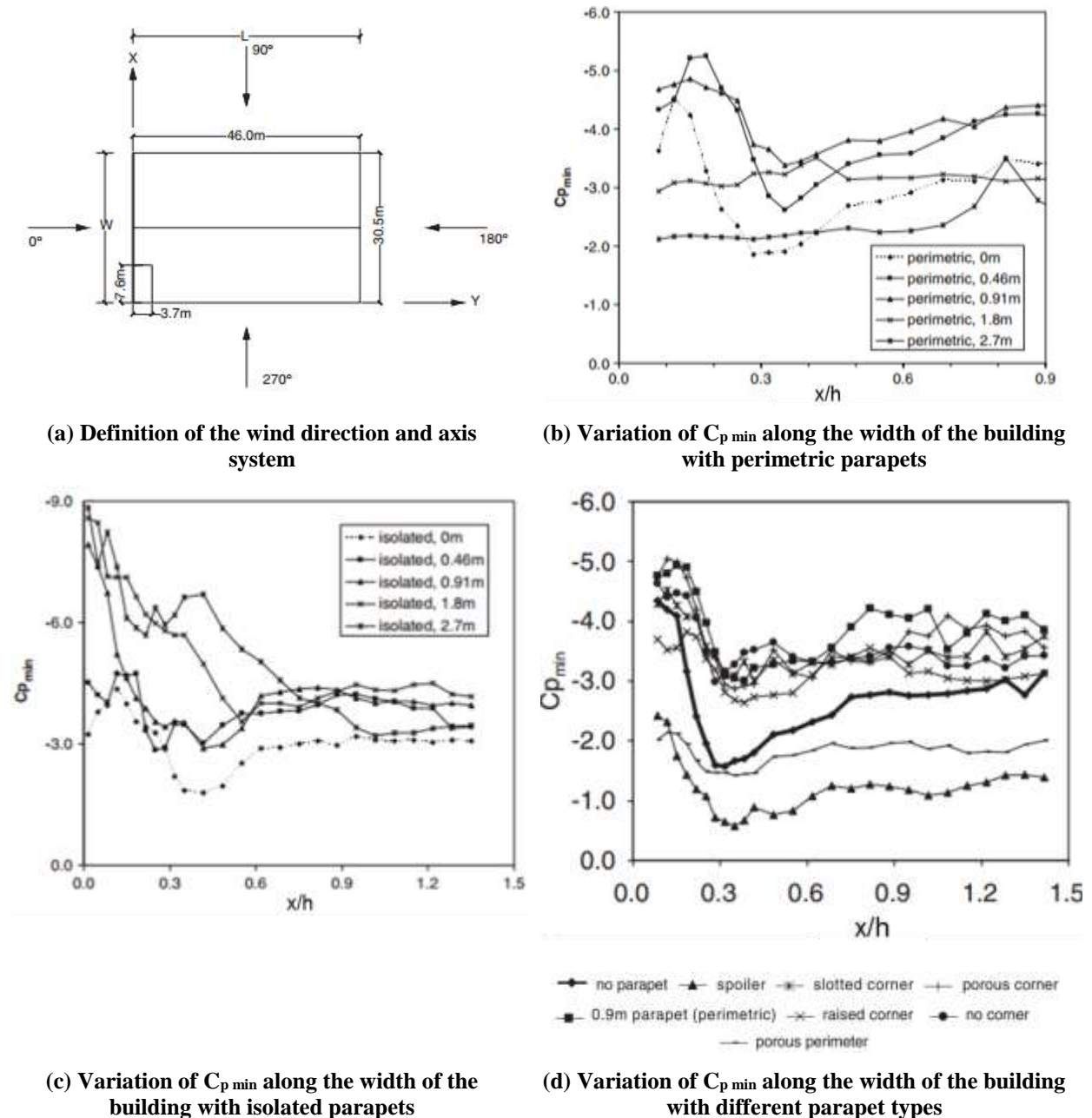


Figure 2-30. Minimum pressure coefficient distribution along the line $y/H = 0.42$ ($25.4 \text{ mm} = 1 \text{ in.}$) (Kopp et al. 2005a)

Chowdhury and Blessing (2007) conducted seven full-scale tests under simulated hurricane wind loads using the Wall of Wind (WOW) at the Florida International University (FIU). Six tests included six different aerodynamic devices while the seventh test was conducted without any devices to use as the benchmark. Figure 2-31 shows the $10 \times 10 \times 10 \text{ ft}$ test structure placed in front of the WOW. The evaluation included four modified and two standard edge devices as shown in Figure 2-32. The modified edge devices were patented or patent pending aerodynamic devices

under the AeroEdge trademark. The two standard edge shapes tested were the Econosnap standard edge fascia and the Drain-thru gravel stop, both of which were of the industry standard (Chowdhury and Blessing 2007).



Figure 2-31. A test structure placed in front of the WOW at a 45° wind direction (Chowdhury and Blessing 2007)

Chowdhury and Blessing (2007) performed gravel scour testing to visually observe the generation of conical vortices in the presence of roof edge devices. For the gravel scour testing, a 2 in. thick layer of 1/4 in. nominal diameter river gravel was placed on the roof, and the test structure was oriented at a 45° angle with respect to the wind direction. Four test configurations, as described in Table 2-3, were used to identify the wind speeds at which the roof gravel is scoured under conical vortices. Table 2-3 shows the gravel scouring patterns resulted from each test configuration. These images were qualitatively and quantitatively examined to observe the effect of each edge shape on the vortex generation. Three criteria were used to evaluate the capability of an edge shape to reduce suction pressure on the roof. They are wind speed at which gravel scour occurred, magnitude of the gravel scour, and location of gravel scour initiation on the roof. The observations revealed that the presence of modified edge shapes did affect the vortex generation. The AeroEdge guard deflects the vortex above the roof surface so that the vortex no longer interacts with the roof. The rounding sharp edge of the AeroEdge cap completely destroys the vortex. In addition, the edge devices increased the threshold speed at which the gravel scouring is initiated by at least a factor of two compared to the traditional edge products. This fact is illustrated by comparing the variation of scour threshold speeds for the traditional and the AeroEdge guard with the gravel diameter as shown in Figure 2-33 (Lin et al. 2008).

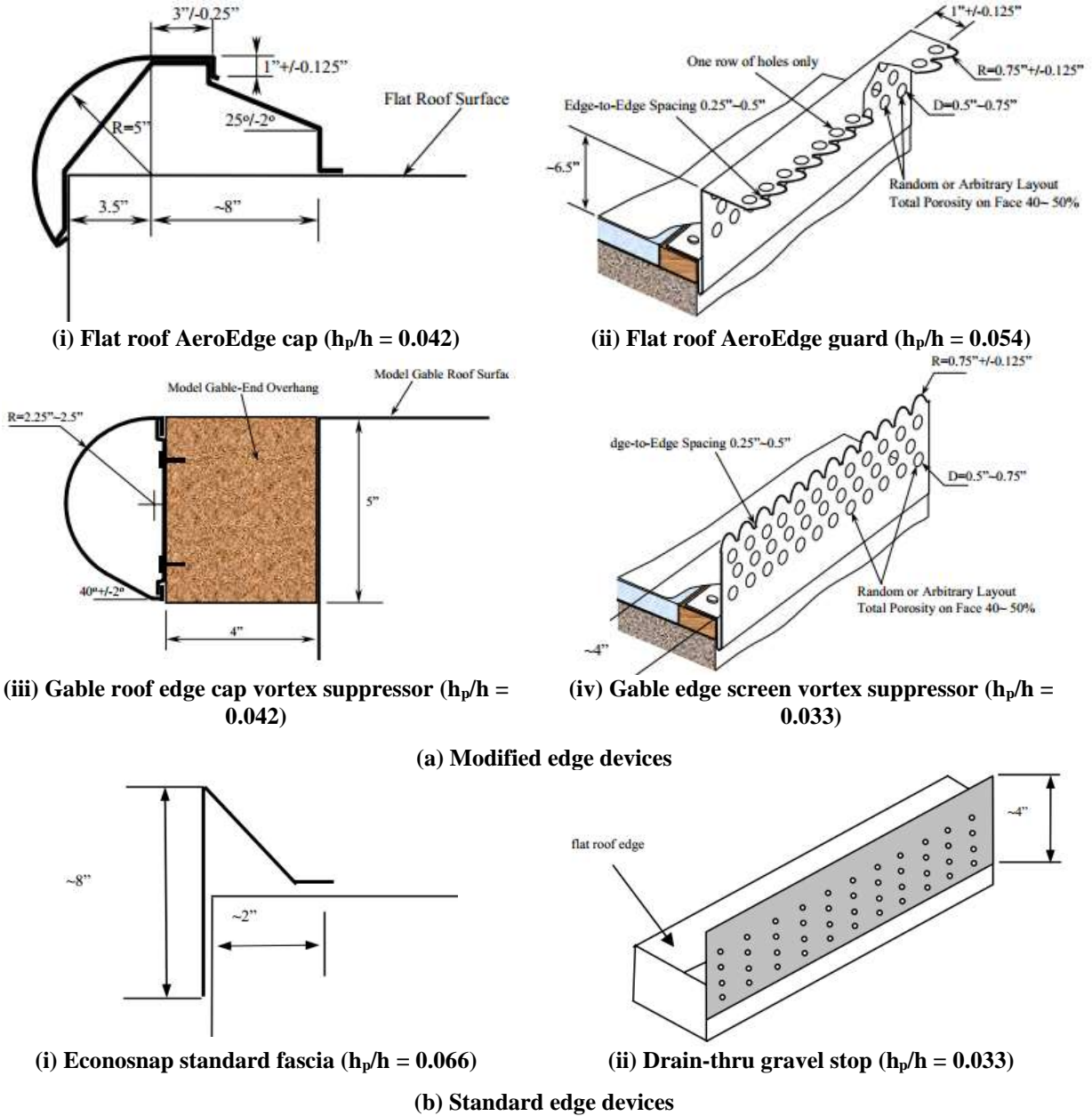










Figure 2-32. Modified and standard roof edge devices (Chowdhury and Blessing 2007)

Table 2-3. Test Configurations Used in Gravel Scour Testing (Chowdhury and Blessing 2007)

Edge Shape Used at		Details	Observations
Windward Side	Leeward Side		
Test Configuration 1			
Econosnap standard fascia	4 in. porous parapet		Gravel scour occurred at 60 mph maximum wind speed 
Test Configuration 2			
Drain-thru gravel stop	4 in. porous parapet		Gravel scour occurred at 60 mph maximum wind speed 
Test Configuration 3			
Flat roof AeroEdge guard	4 in. porous parapet		Slight or no gravel scour was observed 
Test Configuration 4			
Flat roof AeroEdge cap	4 in. porous parapet		Slight or no gravel scour was observed 

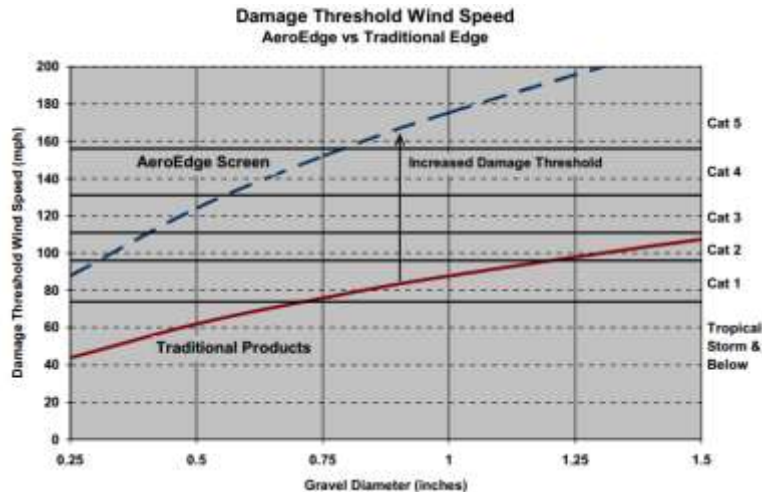


Figure 2-33. Comparison of the scour threshold wind speeds as a function of the gravel diameter for traditional roof edge products and the AeroEdge guard (Lin et al. 2008)

In addition to the four test configurations described in Table 2-3, seven different test configurations were developed to evaluate the performance of six edge shapes shown in Figure 2-32 in reducing suction pressures developed on a flat roof. A test structure, similar to the one used for gravel scour testing, was placed at an angle of 45° in front of the WOW. Pressure distribution was measured, and the external pressure coefficients ($C_{p \text{ min}}$, $C_{p \text{ max}}$, $C_{p \text{ mean}}$, and $C_{p \text{ rms}}$) were calculated to compare with those of the control test to evaluate the percentage reduction in the roof corner suction. Further, $C_{p \text{ min}}$ and $C_{p \text{ max}}$ coefficients were compared with the design coefficients specified in the ASCE 07-05 for Zone 3. Table 2-4 lists the edge shapes used at the windward and leeward sides and the findings. The pressure measurements show a reduction of the suction pressures at the roof corner up to 75% in the presence of the modified edge shapes compared to the traditional edge shapes. Out of the six edge shapes tested, the flat roof AeroEdge guard successfully reduced the roof uplift by destroying the rotational flow of the vortices. All the tested edge shapes caused an increase in suction at certain locations on the roof. The gable edge screen vortex suppressor yielded the highest increase in suction. This is similar to the observation made by Bienkiewicz and Sun (1992) and Cochran and English (1997): shorter parapets tend to increase suction at certain locations on the roof. Overall, all the edge shapes had an impact on both the suction pressures at the roof corner and the pressure distribution on the roof. Since the edge shapes were successful in reducing the roof suction, less negative design pressures for Zone 3 are recommended to be used in design and construction of roofs with these edge shapes (Chowdhury and Blessing 2007).

Table 2-4. Test Configurations Used in Pressure Measurements and the Observations Made (Chowdhury and Blessing 2007)

Test Configuration	Edge Shape Used at		Details	Observations
	Windward Side	Leeward Side		
1	None	None	Control test	High suction at the roof corners and roof edges. Pressure decreases with the increase in distance from the roof edge.
2	Econosnap standard fascia	Gable Edge Screen Vortex Suppressor	-	Slight reduction in the extreme suction at the roof corner.
3	Drain-thru gravel stop		-	Slightly increased $C_{p \text{ min}}$ values.
4	Flat roof AeroEdge guard		-	Yielded the best results in terms of reducing the overall roof suction. Overall, $C_{p \text{ min}}$ was reduced from 15-74% and $C_{p \text{ mean}}$ was reduced from 25-70% depending on the location. The pressure distribution over the roof was uniform.
5	Gable edge vortex cap suppressor		Gable edge vortex cap suppressor extended 2.375 in. above the roof surface	Recorded reductions in the roof uplift by 10-45% at majority of the locations. Helped to reduce the suction pressure throughout the entire roof surface, not just closer to the edge.
6	Gable edge vortex cap suppressor		Gable edge vortex cap suppressor extended 0.5 in. above the roof surface	More significant reduction in the roof suction than the taller version (Gable edge vortex cap suppressor extending 2.375 in. above the roof surface).
7	Gable edge screen vortex suppressor		-	Increase or decrease in pressure depends on the location on the roof. Suction increased by 107% at one location on the roof edge. However, the pressure distribution over the roof was uniform.

Sehn (2008) performed a comparative study of aerodynamic attachments shown in Figure 2-35 on reducing the peak roof uplift pressure. The flush edge spoiler, the 10% porous canopy roof, and passive pressure equalization method reduced peak uplift by 32.3%, 31.4%, and 31.1%, respectively. The reduction in uplift pressure on the porous canopy roof with a 10% porosity is much greater when compared with the roof with a 1% porosity. However, the performance of the proposed rotating cylinder (momentum injecting method) was not evaluated by Sehn (2008).

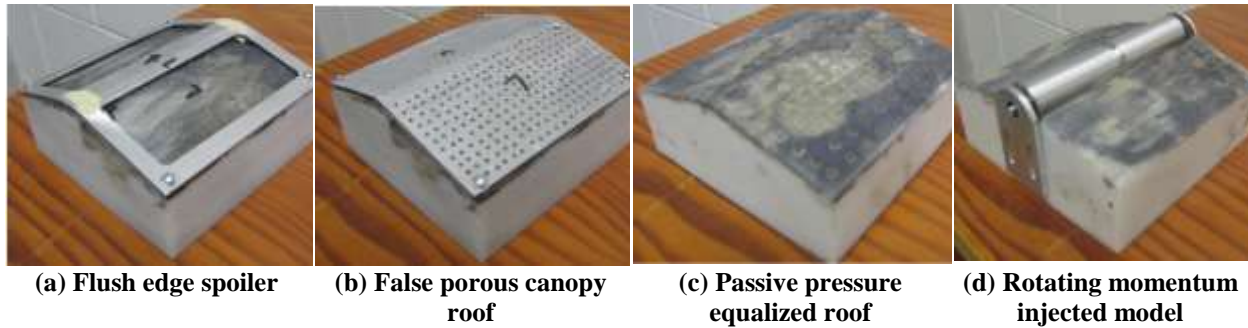


Figure 2-34. Aerodynamic mitigation techniques (Sehn 2008)

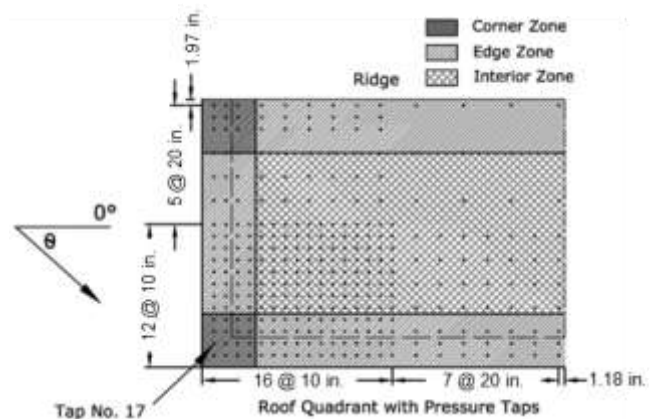
Suaris and Irwin (2010) investigated the effectiveness of solid and perforated parapets in mitigating high suctions at the roof edges and corners of low-rise buildings. Wind tunnel testing was conducted on a 1:20 scaled building with a roof pitch of 3:12. The following parapet configurations were considered for their study:

- A 7.87 in. (0.2 m) tall solid parapet ($h_p/h = 0.054$)
- A 7.87 in. (0.2 m) tall parapet with a perforation ratio of 20% (perforated parapet) ($h_p/h = 0.054$)
- A 7.87 in. (0.2 m) tall parapet with a perforation ratio of 33% and length equal to 10% of the short building dimension (corner parapet) ($h_p/h = 0.054$).

The parapets were installed along the roof perimeter, corners, and corner and ridge. Figure 2-35(a) shows a test model with corner and ridge parapet configuration placed inside the wind tunnel. A reference wind speed of 49.21 ft/s (15 m/s) at a reference height of 98.43 ft (30 m) in full-scale was applied to the models at wind angles of 10° intervals. The wind tunnel simulated rough terrain condition C, as defined in the ASCE 07. Figure 2-35(b) shows the roof pressure tap layout.



(a) Test model with corner and ridge parapets



(b) Pressure tap layout on the roof (plan view)

Figure 2-35. Test model placed inside the wind tunnel (a) and pressure tap layout on the roof (b) (Suaris and Irwin 2010)

Figure 2-36 shows the maximum pressure coefficients recorded along the gable end, ridge, and eave of the roof. The model without parapets records the highest peak coefficients. As shown in Figure 2-36c, the peak pressure coefficients at the corners ($x/L \cong 0$) are reduced by over 50% with corner parapets (Suaris and Irwin 2010). Even though the use of such parapet configurations is capable of reducing corner suction, the practical implementation is questionable due to the size (height) of such parapets in a prototype building.

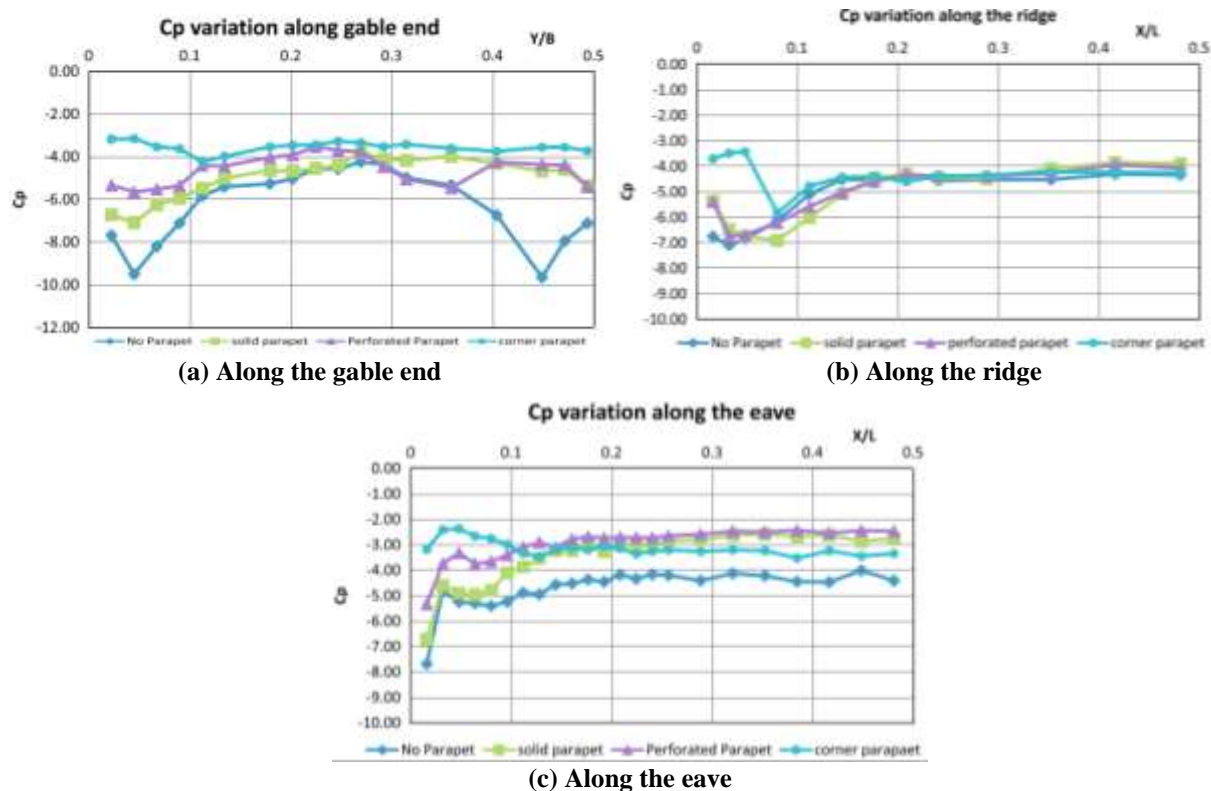


Figure 2-36. Variation of the peak pressure coefficient along the gable end (a), ridge (b), and eave (c) (Suaris and Irwin 2010)

Note: X: Distance along the length of the roof, Y: Distance along the width of the roof.

Bitsuamalak et al. (2013) evaluated the potential use of architectural elements such as pergolas (trellises) for eave damage mitigation, gable end ribs (roof extensions at gable ends) for corner damage mitigation, and ridge rib (ridgeline extensions) for ridge damage mitigation. The evaluation was performed by conducting wind tunnel testing on 1:15 scale models of gable and hip roofs. Figure 2-37 shows pergolas and gable end ribs installed on the test models. The pergolas disrupt the formation of the vortices and encourage the vortex shedding at eave corners. Both ridgeline extensions and gable end extensions displace the vortex away from the roof ridge corner and roof end regions.

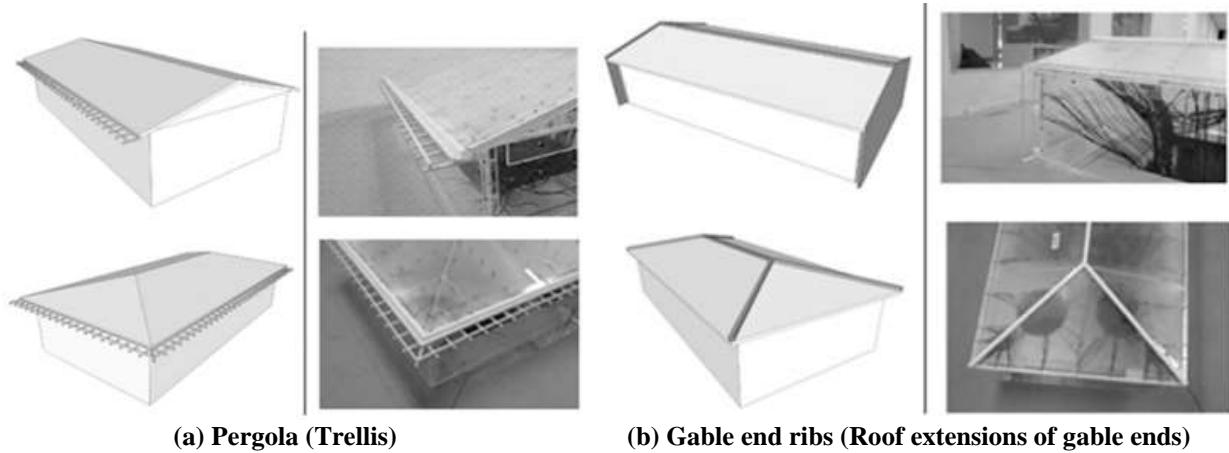


Figure 2-37. Architectural elements installed on the roof (Bitsuamalak et al. 2013)

Figure 2-38 shows the variation of the peak pressure coefficients along the width of the gable roof and hip roof under a wind angle of 0° (wind flowing perpendicular to the length of the roof). When the wind is at 0° , a 25% pressure reduction on the windward eave was observed for the models with pergolas (both roof geometries). When the wind angle was 0° , the peak pressure at the ridge is significantly reduced (about 60%) in the model with ridgeline extensions; however, a moderate increase in the pressure on the leeward side of the roof is observed. Figure 2-39 shows the variation of the peak pressure coefficients along the length and width of the gable roof under a wind angle of 90° (wind flowing parallel to the length of the roof). When the wind angle is 90° , the suction closer to the gable end zone is significantly reduced in the models with gable end extensions, without an increase in pressure in other parts of the roof (Bitsuamalak et al. 2013).

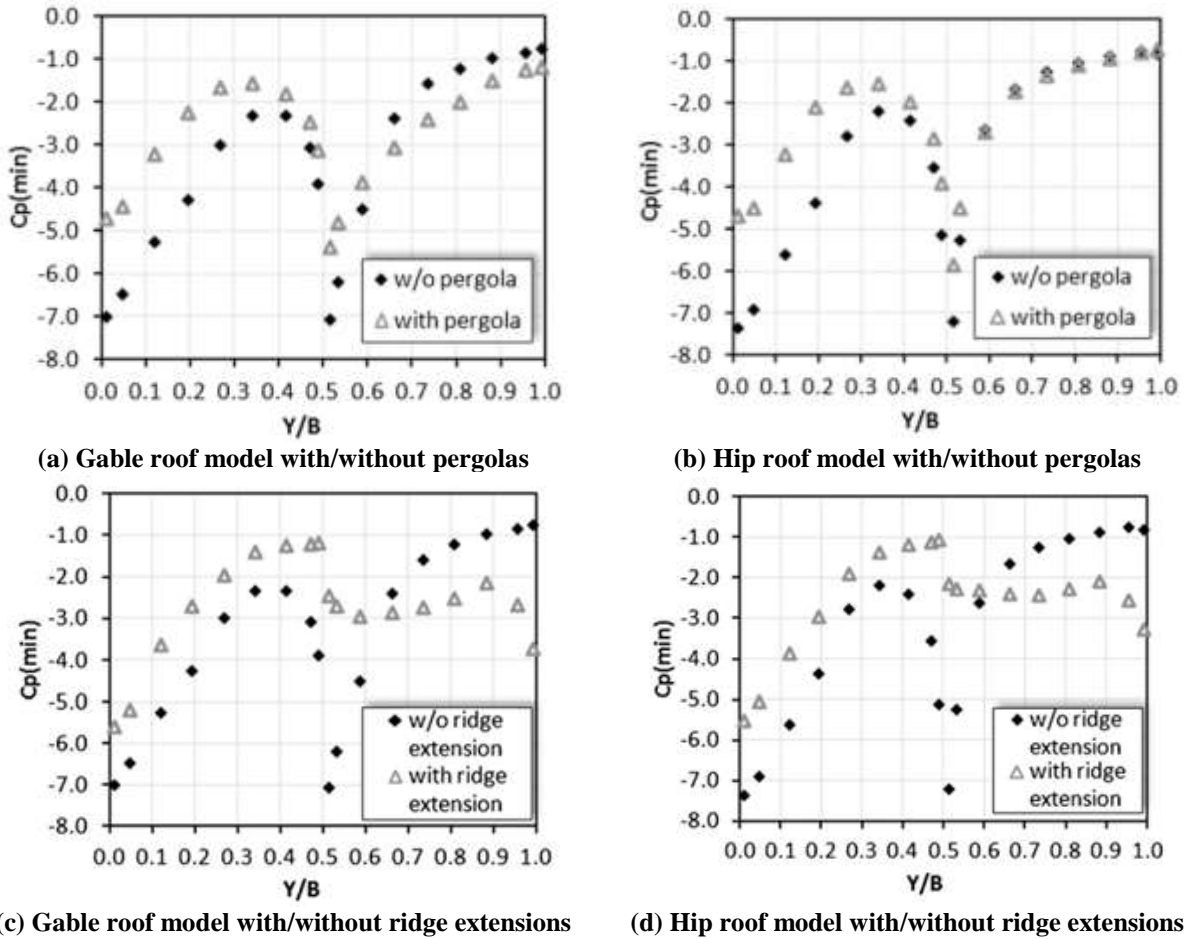


Figure 2-38. Variation of peak pressure coefficients on the gable roof and hip roof model with pergolas and ridge extensions under 0° wind direction (Bitsuamalak et al. 2013)

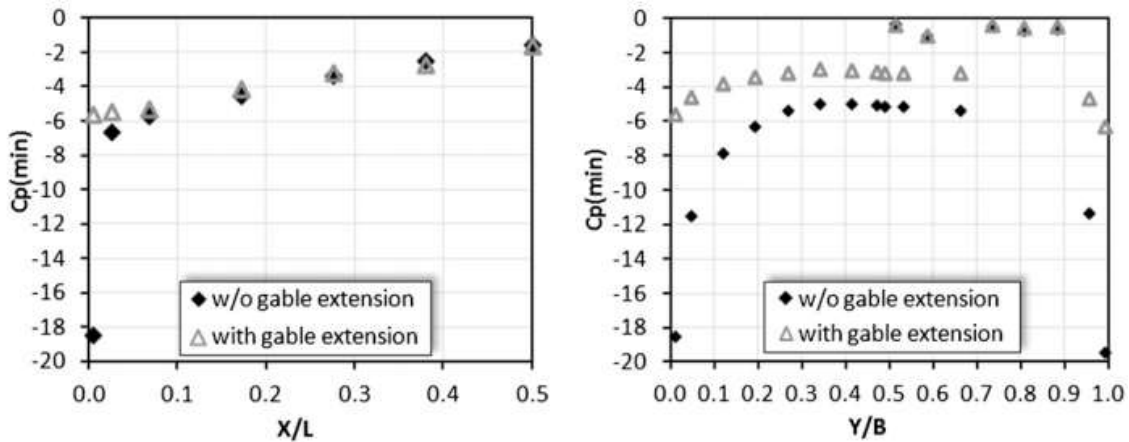


Figure 2-39. Variation of peak pressure coefficients on the gable roof with gable end extensions under 90° wind direction (Bitsuamalak et al. 2013)

Note: X: Distance along the length of the roof, and Y: Distance along the width of the roof.

Huang et al. (2013) studied the change in flow patterns around the roof of a low-rise experimental structure. Two roof pitches (10° and 18.4°) and several parapet configurations, as

shown in Figure 2-40, were considered. The configurations include (i) a 12 in. (0.3 m) tall parapet along the roof edge, (ii) 12 in. (0.3 m) tall and 19.5 in. (0.5 m) long corner parapets, and (iii) 27.3 in. (0.7 m) tall and 19.5 in. (0.5 m) long discrete parapets. The discrete system included two parapet segments spaced at 101.4 in. (2.6 m), three segments spaced at 58.5 in. (1.5 m), and four segments spaced at 39 in. (1 m). The parapet configuration shown in Figure 2-40(a) was installed on the roof with a pitch of 18.4° . The other two parapet configurations were installed on the roof with a pitch of 10° . The mean and fluctuating wind pressure coefficients were measured on the roofs under natural wind conditions before and after installing the parapets. The wind direction was measured clockwise from the edge with the continuous parapet. As an example, 90° wind flows perpendicular to the edge with the continuous parapet are shown in Figure 2-40(a).



(a) 12 in. (0.3 m) tall parapet along the roof



(b) 12 in. (0.3 m) tall and 19.5 in. (0.5 m) long corner parapet



(c) Four segment discrete parapet [one segment is 27.3 in. (0.7 m) tall and 19.5 in. (0.5 m) long]

Figure 2-40. Different parapet configurations installed on the full-scale structure (Huang et al. 2013)

The mean and fluctuating pressure coefficients on the roof with and without a 12 in. (0.3 m) tall continuous parapet along the windward roof edge were measured under the wind directions of 35° and 40° . As shown in Figure 2-41a, the presence of a 12 in. tall ($h_p/h = 0.0375$) continuous parapet reduced the maximum pressure coefficients of 1.2 at the windward roof corner to 0.6. The fluctuating pressure coefficients on the roof with a corner parapet were measured under a wind direction of 145° . As shown in Figure 2-41(b), the presence of a corner parapet ($h_p/h = 0.0375$; $l_b/L = 0.05$, $l_b/B = 0.083$) reduced the maximum pressure coefficient of 1.8 at the windward roof corner to 1.2.

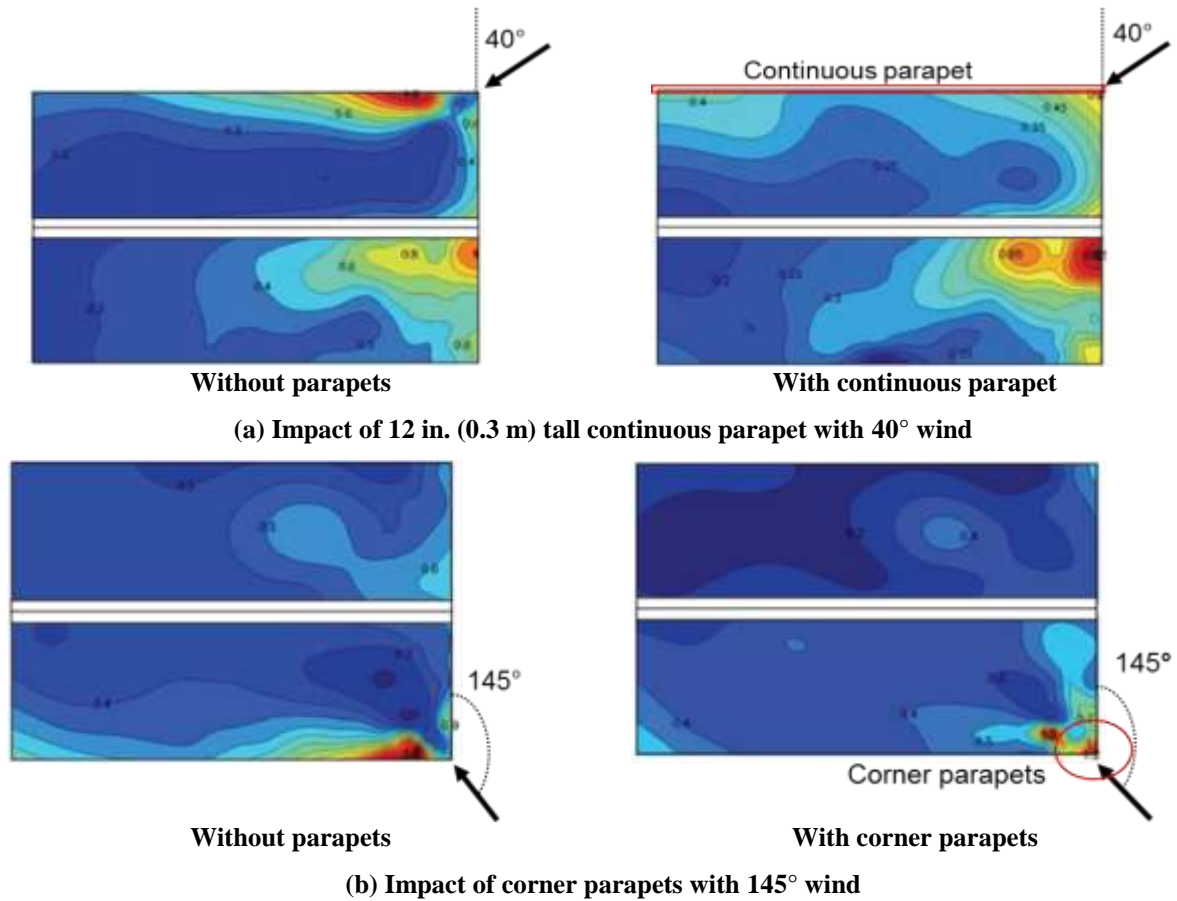


Figure 2-41. Fluctuating wind pressure coefficients on the roof with a continuous parapet (a) and a corner parapet (b) (Huang et al. 2013)

The fluctuating pressure coefficients were measured on a 10° roof with discrete parapets. The impact of the presence of a discrete parapet with four segments on roof pressure distribution was evaluated under 160°, 170°, and 180° wind directions. Figure 2-42(b) shows the fluctuating roof wind pressure coefficients in the presence of a four-segment discrete parapet under a wind direction of 180°. As shown in Figure 2-42(b), the use of discrete parapets ($h_p/h = 0.0875$, $l_p/L = 0.05$) is not effective. The high negative pressure is a result of the formation of wakes behind the discrete parapet (Huang et al. 2013).

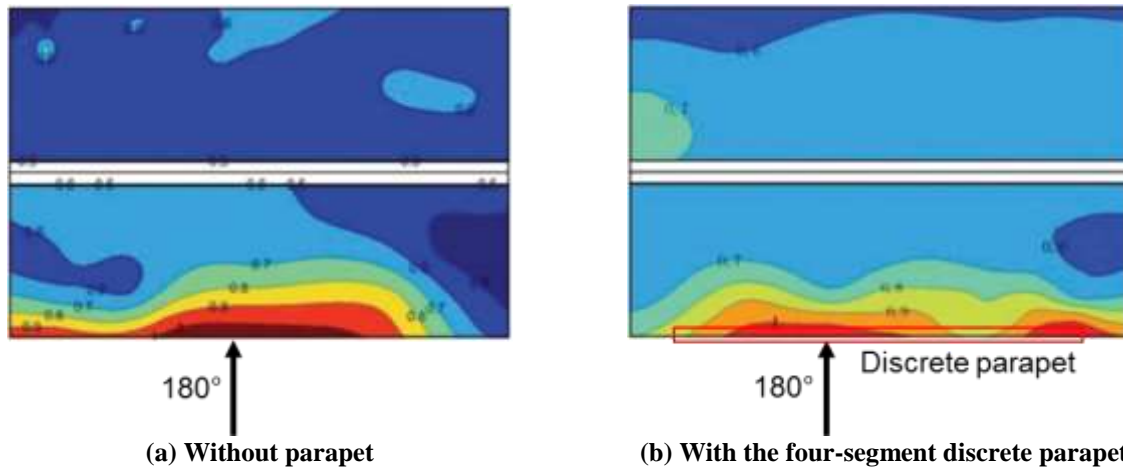


Figure 2-42. Fluctuating wind pressure coefficients on the roof with the four-segment discrete parapet with 180° wind (Huang et al. 2013)

Figure 2-43 shows eight eave configurations used in residential houses in the typhoon prone coastal regions of southeastern China. Huang et al. (2014) evaluated the possibility of using these configurations on reducing peak roof suction. Wind tunnel testing was performed on 1:20 scaled gable roof models with 14° , 26° and 34° pitch. The models were subjected to wind under simulated open terrain conditions and directions ranging from 270° to 360° at 15° intervals. The 270° wind direction corresponds to wind flowing perpendicular to the sorter edge of the roof. The variation of the maximum pressure coefficients at the roof corners and edges was measured under each wind direction. All the eave configurations reduced peak suction at the windward roof corners and edges compared to the buildings without eaves.

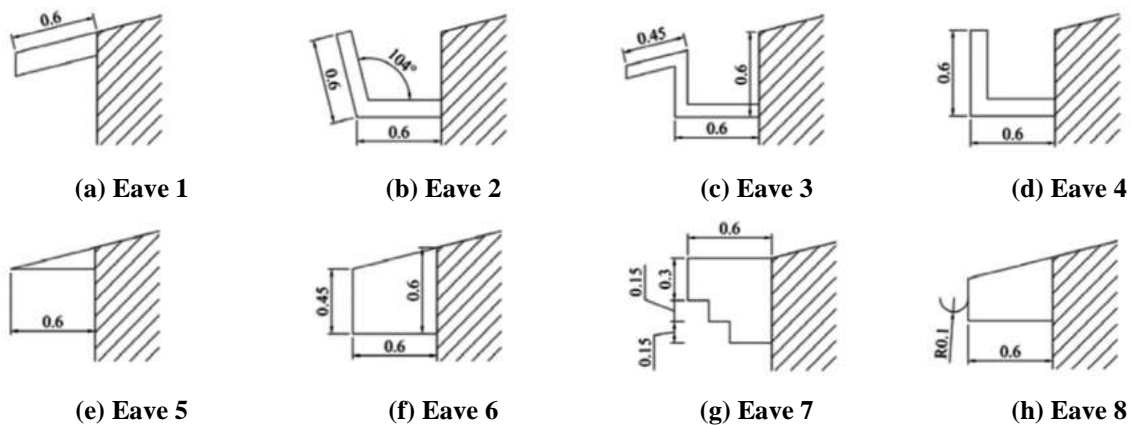


Figure 2-43. Eave configurations used by Huang et al. (2014) (units are in m, 1 m = 39 in.)

Figure 2-44 shows the variation of the peak uplift pressure coefficients on the windward surface of the roofs of the three models with the wind direction. It is clear that under all the wind

directions, the overall best performance was observed with Eave 3 configuration. The impact of these eave configurations on the leeward roof slopes was negligible.

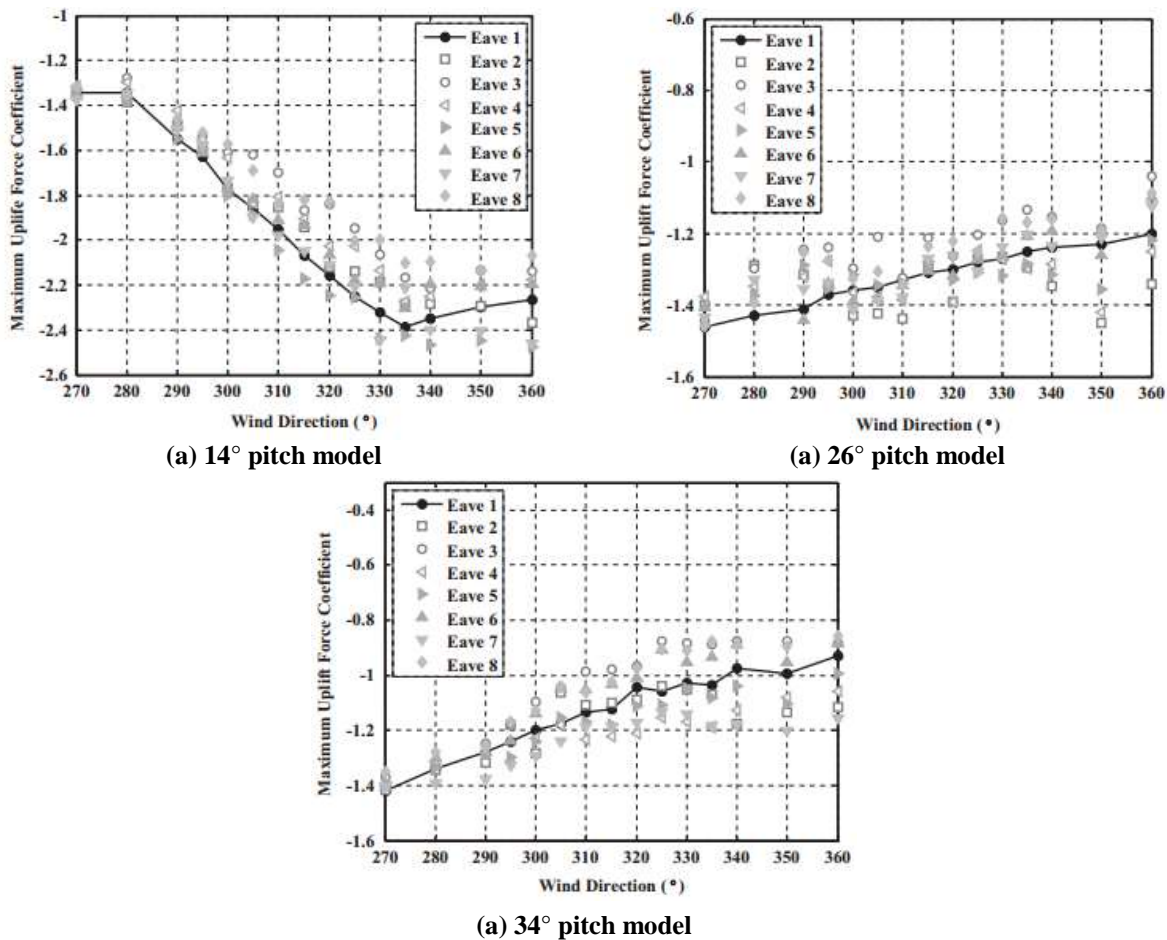


Figure 2-44. Variation of the maximum uplift pressure coefficients on the windward roof surface of the three models with the wind direction

Iverson (2016) investigated the use of solar panels as possible aerodynamic mitigation devices on low-rise, flat roof buildings. Wind tunnel testing was performed on 1:27 scaled building models with solar panels installed around the roof edges under three different wind directions: 0°, 45°, and 90°. The 0° wind direction is perpendicular to the leading edge of the building. The roof without solar panels was used as the reference. The experimental results were evaluated both qualitatively and quantitatively. The qualitative evaluation involved the visualization of flow patterns using the sand erosion technique after 1 minute of wind loading. Figure 2-45 shows the distribution of the sand on the roofs of the test models, before and after wind loading at a 45° wind direction. Figure 2-45(a) shows the distribution of the sand on the bare roof before and after wind loading. Figure 2-45(b) shows the distribution of the sand on the roof with solar panels before and after wind loading. A significant reduction in sand scouring was

observed in the roof with solar panels. The slight scouring of sand observed on the roof with solar panels after 1 minute loading, as shown in Figure 2-45(b), was assumed to have been caused by the wind infiltrating through the slight gap between roof and the solar panels. In order to prevent this, the gap was sealed with tape and was re-tested under wind loading. As shown in Figure 2-45(c), sealing of the gap between solar panels and the roof clearly resulted in no visible sand scouring on the roof after 1 minute of loading.

The data recorded using pressure taps quantified the impact of solar panels on the reduction in roof pressure. Table 2-5 shows the maximum and minimum pressure coefficients observed on the roof with and without solar panels under three wind directions: 0° , 45° , and 90° . The maximum suction pressure reduces with the addition of solar panels along the roof edge, and the best performance is observed with a 45° wind direction. The roof was divided into the three zones (Zone 1, Zone 2, and Zone 3) as per the ASCE 07-10, and the experimental external pressure coefficients were calculated for each zone. The experimental pressure coefficients were compared with the ASCE 07-10 values as shown in Table 2-6. The ASCE 07 coefficients were less conservative when compared with the measured experimental values.

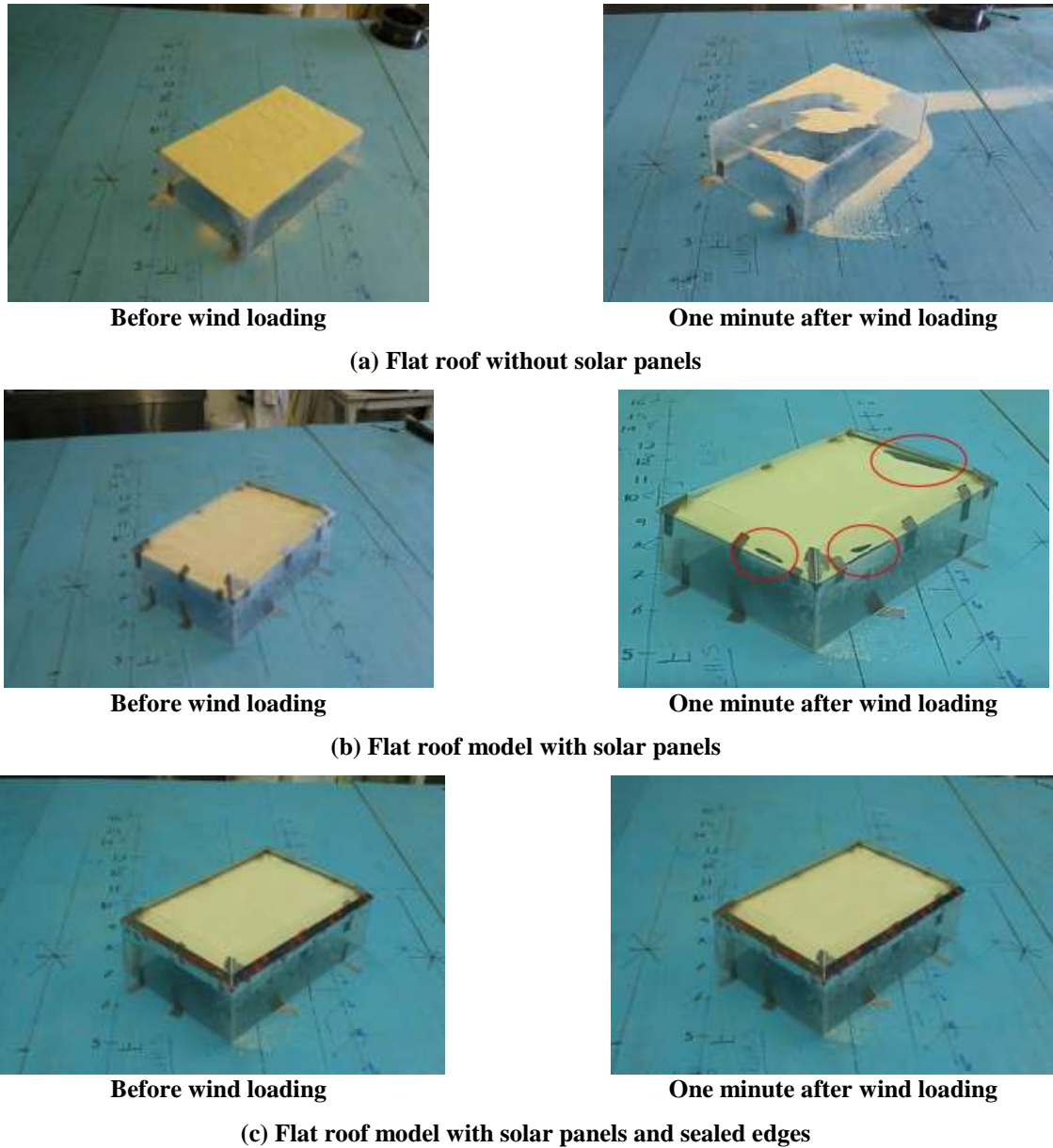


Figure 2-45. Sand erosion observed on flat roofs installed with solar panels along the roof edge (Iverson 2016)

Table 2-5. Peak Values of Minimum Pressure Coefficients (C_p) with and without Solar Panels (Iverson 2016)

Wind Angle	Minimum Values	
	Minimum C_p without Solar Panels	Minimum C_p with Solar Panels
0°	-1.5761	-0.7037
45°	-3.4597	-0.8212
90°	-1.2459	-0.7508

Table 2-6. ASCE 07-10 Pressure Coefficients and Measured Values with and without Solar Panels (Iverson 2016)

Zone	ASCE 07-10	Measured C_p	
		Without Panels	With Panels
1	-0.9	-1.7946	-0.5992
2	-1.1	-1.8110	-0.5310
3	-1.8	-2.0853	-0.6814

Aly and Bresowar (2016) studied the performance of roof damage mitigation devices shown in Figure 2-46. The height of an aerodynamic device (h_p) was assigned three values relative to the height of the building (h) – small ($h_p/h = 0.08$), medium ($h_p/h = 0.16$), and large ($h_p/h = 0.24$). The results were used to identify the device that minimizes the uplift force on the roof and lift and drag forces on the device itself.

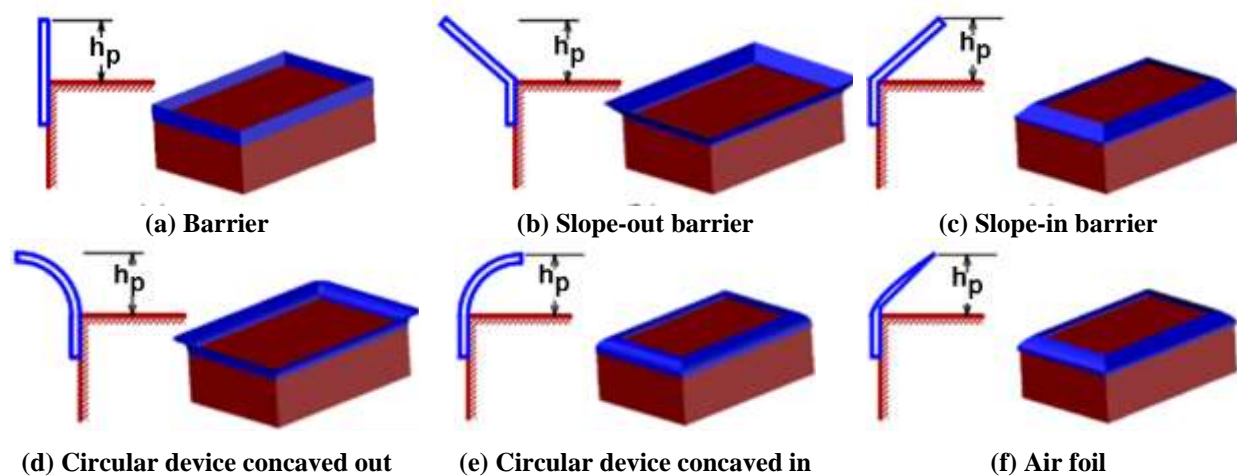
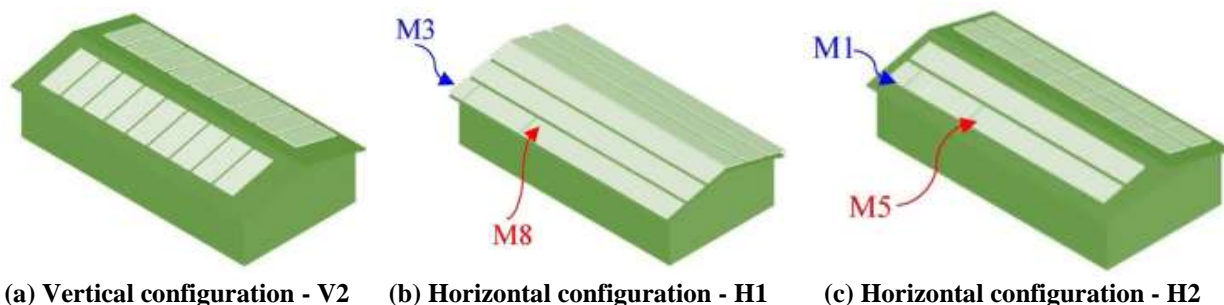
**Figure 2-46. Roof damage mitigation devices evaluated by Aly and Bresowar (2016)**

Table 2-7 shows the drag and lift coefficients (C_d and C_l) for the building and the aerodynamic devices. The percentage reduction or the increase in the coefficients with respect to the bare roof was calculated to evaluate the effectiveness of each device. In general, the larger the device, the larger the drag force on it. In comparison, the air foil device (shown in Figure 2-46(f)) generates the least uplift loads on the building and the device itself. However, the slope-in barrier (shown in Figure 2-46(c)) was suggested as the practical shape due to its simplicity and the possibility of replacing it with solar panels. Also, small and medium size devices are more suitable for low-rise buildings.

Table 2-7. Drag and Lift Coefficients on the Building and the Damage Mitigation Devices (Aly and Bresowar 2016)

Corner	Size	Building Force Coefficients		Device Force Coefficients		Total Force Coefficients	
		C_a	C_l	C_a	C_l	C_a	C_l
Bare roof	-	1.02	1.33	-	-	1.02	1.33
Barrier	Small	1.12 (5.7%)	1.03 (-22.6%)	0.23	0.04	1.35 (27.4%)	1.07 (-19.4%)
	Medium	1.14 (7.5%)	0.99 (-25.6%)	0.42	0.04	1.56 (47.2%)	1.07 (-19.3%)
	Large	1.18 (11.3%)	1.26 (-5.3%)	0.55	0.04	1.73 (63.2%)	1.23 (-7.9%)
Slope-out barrier	Small	1.15 (8.5%)	1.06 (-20.3%)	0.26	0.17	1.41 (33.0%)	1.17 (-12.0%)
	Medium	1.18 (11.3%)	0.92 (-30.8%)	0.49	0.30	1.67 (57.5%)	1.18 (-11.0%)
	Large	1.29 (21.7%)	0.87 (-34.6%)	0.76	0.40	2.05 (93.4%)	1.26 (-5.0%)
Slope-in barrier	Small	1.04 (-1.9%)	0.77 (-42.1%)	0.09	0.13	1.13 (6.6%)	1.04 (-22.0%)
	Medium	1.07 (0.9%)	0.89 (-33.1%)	0.23	0.11	1.30 (22.6%)	1.03 (-22.2%)
	Large	1.09 (2.8%)	1.11 (-16.5%)	0.29	0.04	1.38 (30.2%)	1.19 (-10.5%)
Circular device concaved out	Small	1.08 (1.9%)	1.08 (-18.8%)	0.25	0.24	1.33 (25.5%)	1.28 (-3.9%)
	Medium	1.18 (11.3%)	0.98 (-26.3%)	0.46	0.49	1.64 (54.7%)	1.36 (2.2%)
	Large	1.26 (18.9%)	0.90 (-32.3%)	0.68	0.71	1.94 (83.0%)	1.50 (12.5%)
Circular device concaved in	Small	1.01 (-4.7%)	0.62 (-53.4%)	0.06	0.21	1.07 (0.9%)	1.01 (-24.1%)
	Medium	1.05 (-0.9%)	0.58 (-56.4%)	0.18	0.31	1.23 (16.0%)	1.05 (-21.3%)
	Large	1.06 (0.0%)	0.75 (-43.6%)	0.24	0.39	1.30 (22.6%)	1.26 (-5.1%)
Air foil	Small	1.03 (-2.8%)	0.71 (-46.6%)	0.10	0.12	1.13 (6.6%)	0.96 (-27.9%)
	Medium	1.07 (0.9%)	0.77 (-42.1%)	0.22	0.17	1.29 (21.7%)	1.01 (-24.1%)
	Large	1.08 (1.9%)	1.02 (-23.3%)	0.27	0.14	1.35 (27.4%)	1.20 (-10.0%)

Aly et al. (2017) investigated the possibility of using solar panels as wind suction mitigation devices on gable roof buildings. Three different solar panel configurations, installed on a gable roof building with a roof pitch of 3:12, were evaluated experimentally and numerically. As shown in Figure 2-47, one vertical configuration (V2) and two horizontal configurations (H2 and H3) were considered.

**Figure 2-47. Tested solar panel configurations (Aly et al. 2017)**

Note: M1, M3, M5, and M8 are solar panels on which the pressure distribution was measured.

The pressure-time history was measured on 1:30 scaled building models with and without solar panels. CFD simulations on a 1:15 scaled model of the building were performed using the ANSYS Fluent. The CFD model of the building with H2 solar panel configuration is shown in

Figure 2-48(a). The wind directions considered in the CFD simulations ranged from 0° to 350° in 10° increments. In addition, 45° , 135° , 225° , and 315° were also considered. Figure 2-48(b) illustrates the experimental set up used to collect data for validating the CFD simulation models (Aly et al. 2017).

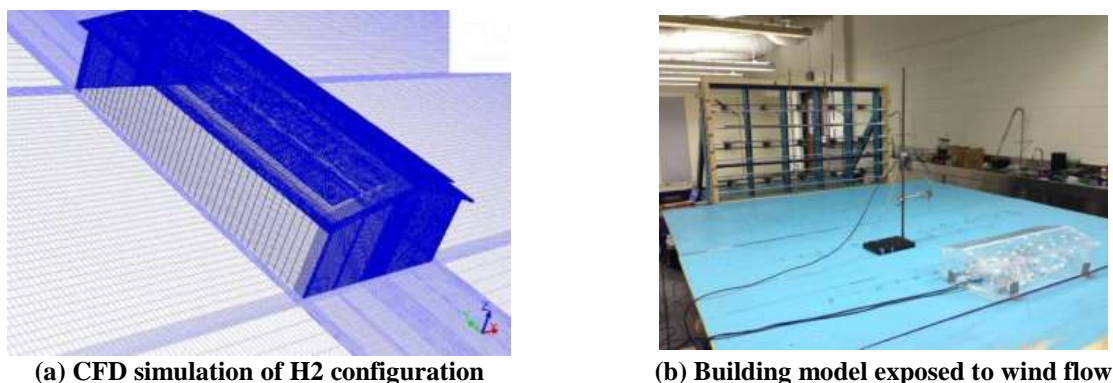


Figure 2-48. Numerical and experimental work conducted by Aly et al. (2017)

Table 2-8 summarizes drag and lift force coefficients on the building, solar panels, and the entire system. The results indicate a reduction in the uplift force on the building with the installation of the solar panels. However, a slight increase in the drag coefficients is observed in the presence of solar panels, but this increase was small compared to the reduction in the uplift forces. Both numerical and experimental results showed that placing the solar panels away from the roof corner and edge reduced the uplift load on the panels themselves. However, a slight increase in the pressure coefficients underneath the solar panels was observed in both numerical simulations and experimental work, possibly due to localized wind accelerations underneath the panels (Aly et al. 2017).

Table 2-8. Drag and Lift Coefficients on the Gable Roof Building with Different Solar Panel Configurations (Aly et al. 2017)

Arrangement	Building		Solar Panels		Total	
	C_d	C_l	C_d	C_l	C_d	C_l
Bare roof	0.449	1.694	0	0	0.449	1.694
H1	0.583	1.132	0.076	-0.010	0.659	1.122
H2	0.625	1.379	0.069	-0.245	0.694	1.134
V2	0.558	1.401	0.037	-0.083	0.595	1.318

Li et al. (2018) evaluated the reduction in wind suction on low-rise gable roof buildings with three different spoiler configurations. A 1:20 scaled gable roof building model with a roof angle of 30° was used in a BLWT. As shown in Figure 2-49, spoiler configurations were labeled based on their position on the roof - at the eaves (Spoiler E), at the gable walls (Spoiler G), and at

the ridges (Spoiler R). The height, width, angle, and the position of spoilers on the roof (eave, gable wall, and ridge) were the parameters used in the analysis to evaluate the effect of these features on roof wind load distribution.

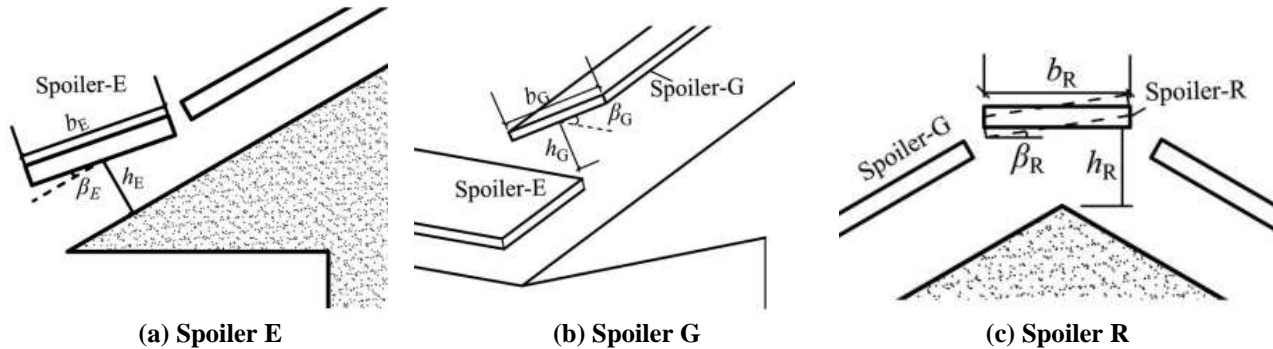


Figure 2-49. Spoiler configurations evaluated by Li et.al (2018)

Note: b_E , b_G , b_R : Width of spoiler, h_E , h_G , h_R : Height of spoiler, β_E , β_G , β_R : Angle of spoiler.

The eave and gable spoilers significantly reduced roof wind pressure when compared with the spoilers at the ridge. This is because the vortices are often formed at roof eaves and gable wall positions. The spoiler angle (β) had the greatest influence on the reduction of wind pressure. The recommended angles for spoiler E and G are $\beta_E = 0^\circ$ and $\beta_G = 10^\circ - 25^\circ$. Based on economic and construction considerations, a width equal to $L/20$, where L is the building length, and a height ranging from 8 in. (0.2 m) to 24 in. (0.6 m) were recommended for a spoiler. The maximum reductions of the mean and peak wind pressure on the roof observed under these recommended dimensions of the spoilers were 90% and 58%, respectively (Li et al. 2018).

Chowdhury et al. (2019) investigated the use of roof integrated wind turbine systems to reduce wind uplift loads and generate power. This is a patented system known as Aerodynamics Mitigation and Power System (AMPS). The AMPS system consists of two horizontal axis wind turbines that can be fitted onto roofs with or without gutters as shown in Figure 2-50(a). Figure 2-50(b) shows three different wind turbine configurations evaluated by Chowdhury et al. (2019). A 1:65 scaled flat roof building model was used for this study. Wind load was generated using the WOW from several directions ranging from 0° to 90° (0° , 10° , 20° , 30° , 37.5° , 45° , 52.5° , 60° , 70° , 80° , and 90°). Area averaged mean and peak pressure coefficients were obtained at various locations on the roof.

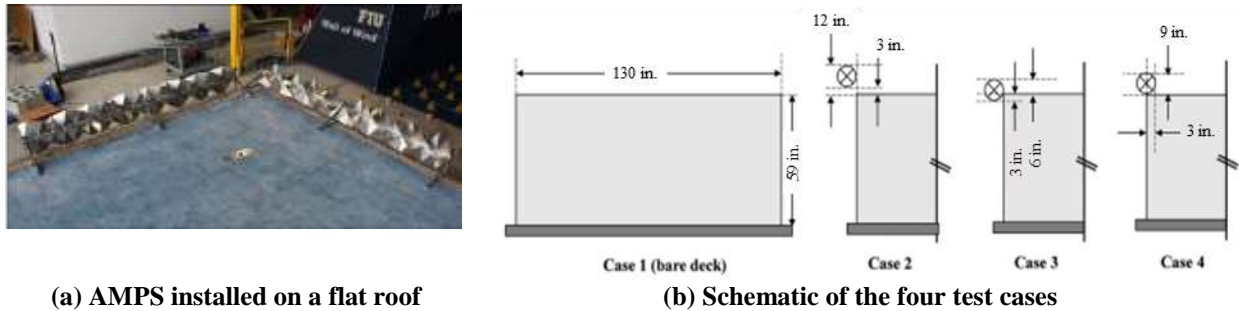


Figure 2-50. Aerodynamics Mitigation and Power Systems (AMPS) evaluated by Chowdhury et al. (2019)

Smoke generators and the sand erosion technique were employed to observe the flow patterns formed around the roof. Figure 2-51(a) shows the formation of conical vortices on the bare roof corner under a 45° wind direction. Figure 2-51(b) shows the observed flow patterns on the roof in the presence of the AMPS under a 45° wind direction. In the presence of AMPS, sand scouring and the formation of vortices at the roof edges and corners were reduced. Therefore, the results of the two flow visualization techniques were used to conclude qualitatively that the presence of wind turbines disrupts the vortex structure and thereby reduces the high roof suction at the roof corners (Chowdhury et al. 2019).

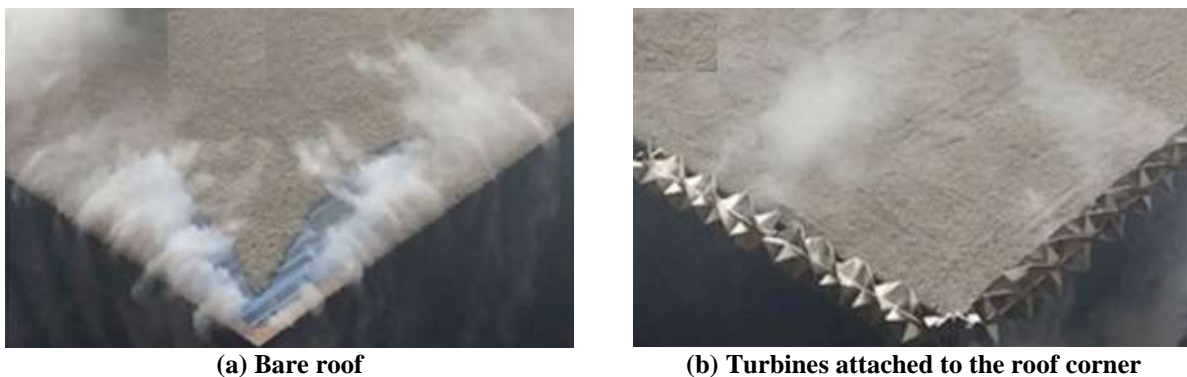


Figure 2-51. Formation of conical vortices under wind direction of 45° and the impact of wind turbines mounted at roof corners (Chowdhury et al. 2019)

For a quantitative assessment of the roof suction reduction, area averaged minimum pressure coefficients were calculated for three zones at the roof corner. The results indicated that AMPS mounted closer to the roof edge effectively reduced roof suction. However, the reduction of suction pressure was less pronounced at locations away from the roof edges.

Qiu et al. (2019) performed numerical studies to propose the best performing porosity of porous parapets that improve the aerodynamic behavior of low-rise buildings with flat roofs. CFD simulations and an optimization algorithm was utilized in this study. The results indicated that the porous parapets with a porosity between 38.2% and 52.3% produced the best results in reducing

peak suction at roof corners when $h_p/h = 0.01 \sim 0.05$. However, when $h_p/h \geq 0.07$, solid parapets exhibited the best performance.

2.4 WIND FLOW MEASUREMENTS AROUND A LOW-RISE BUILDING

The wind loads and structural response are evaluated using scaled models and prototypes under simulated wind conditions, monitoring of in-service structures or experimental structures subjected to natural wind conditions, and numerical simulations. Figure 2-52 illustrates these three approaches of wind measurement studies conducted on low-rise buildings. Wind loads on prototypes can be generated using large turbines such as the wall-of-wind (WOW) or open-jet simulators. The structures instrumented and monitored under the Florida Coastal Monitoring Program (FCMP) and the Kern P. Pitts Center in North Carolina are two examples of monitoring in-service structures under natural wind condition (Caracoglia and Jones 2009, Balderrama et al. 2011).

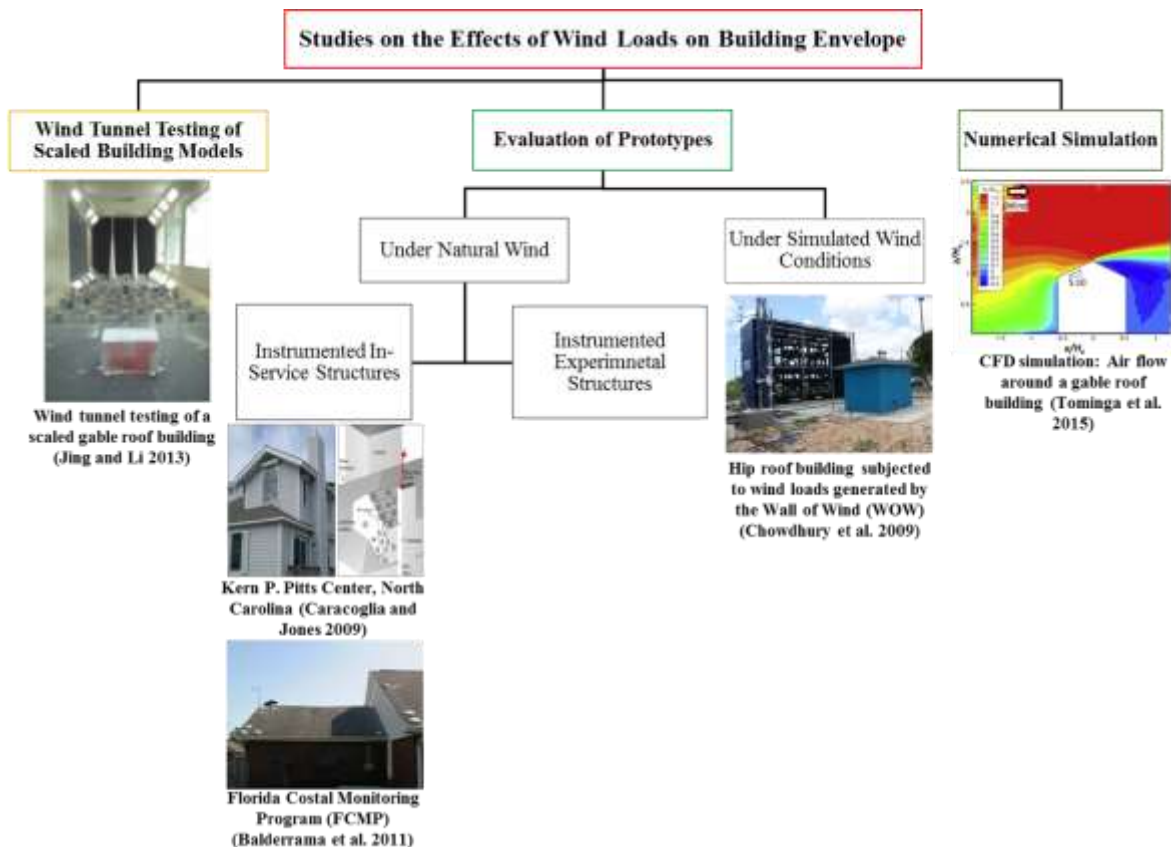


Figure 2-52. Evaluation of wind loads and structural response

The objective of this section is to synthesize information and details on instrumentation and monitoring of prototype structures under natural wind conditions. Details of experimental

structures, flow measurement systems, response measurement systems, and data acquisition and processing systems are presented. In addition, details of two instrumented facilities are presented.

2.4.1 Instrumented Low-rise Buildings

Low-rise buildings are instrumented and monitored under natural winds to gather data to complement the lack of lower atmospheric boundary layer wind data, collect data during specific wind conditions such as typhoons and hurricanes, define wind pressure magnitudes and frequency for experimental investigations, understand the correlation between wind tunnel testing results and the prototype, and validate numerical models. Table 2-9 provides a list of full-scale studies performed on low-rise buildings since 1970s.

Table 2-9. Instrumented Low-Rise Buildings for Wind Pressure and Response Monitoring

Structure	Location	Year of Commencement	Size (Length×Width× Height in m; 1 m = 39 in.)	Roof Pitch	Objective of the Project	Details
Aylesbury structure (Eaton and Mayne 1975)	Aylesbury, UK	Early 1970s	13.3×7×5	5° to 45°	To reduce cost of repair associated with low-rise buildings subjected to wind loads. To address the lack of wind data in the lower atmospheric boundary layer (10m) where majority of the low-rise buildings were located. To address the lack of a systematic way to measure the sheltering effect.	Structure was constructed under a program commenced by the Building Research Establishment (BRE) in the UK. Structure comprised of two single story buildings made of steel frames. The steel frames have six stanchions, with each stanchion standing on a load cell. Timber cladding was used as walls and were fixed to the frame. (See Appendix C for details).
Texas Tech University (TTU) building	Texas, USA	1989	9.1×13.7×4	2°	-	Rotatable building. (See section 2.4.6.1 for details).
Silsoe structure building (SBS) (Aponte-Bermudez 2006)	Silsoe Research Institute, Bedford, UK.	1986	24.3×12.93×4.14	10°	To obtain full-scale wind pressure measurements.	A steel frame building with variable eave styles, sharp eaves or curved eaves of 635 mm radius.
Silsoe cube (Richards et al. 2001, Shea et al. 2010)	Silsoe Research Institute, Bedford, UK.	Beginning of 20 th century	6×6×6	0°	To study the interaction between wind and a structure.	The cube is on a turntable to achieve any wind angle. (See Appendix C for details).
Hunan University (HNU) building (Li et al. 2009, Li et al. 2012a, 2012b, 2017a, 2017b, Li and Yu 2014)	China	2007	6×4×4	1.1°	To monitor wind characteristics and associated building surface pressures during typhoon landfalls.	A moveable low-rise building with a flat roof. (See section 2.4.6.2 for details).

Table 2-9. Instrumented Low-Rise Buildings for Wind Pressure and Response Monitoring (Contd.)

Tongji University (TJU) building (Huang et al. 2012, Xu et al. 2012)	China	2008	10×6×8	0° to 30°	-	-
New Brunswick building (Zisis and Stathopoulos 2009)	Hugh John Fleming Forestry Center, Fredericton, New Brunswick, Canada	Unknown	16.8×8.5	4/12	-	A single story typical north American residential house with a duo pitch roof and a timber wall cladding system. (See Appendix C for details).
Gable roof building with roof overhang (Wang et al. 2018)	Coastal site near Wengtian town, Hainan province, China.	Unknown	24.5×9.5×4.4	9.5°	To investigate negative pressure on gable roof and the overhang.	A gable roof building with an extended roof overhang of approximately 1.3 m and an eave height of 3.5m. A 10m tall meteorological tower to collect wind measurements. (See Appendix C for details).

2.4.2 Instrumented Experimental Structures

2.4.2.1 Location and Exposure Conditions

The location of an instrumented structure needs to be selected after careful evaluation of the monitoring purpose and required site conditions. As an example, Li et al. (2009 and 2012b) instrumented a low-rise building to study typhoon generated wind characteristics and wind effects on low-rise buildings. The site selected for this purpose has an extensive record of typhoon and storm landfalls. Figure 2-53 shows the selected building site and previous typhoon paths.

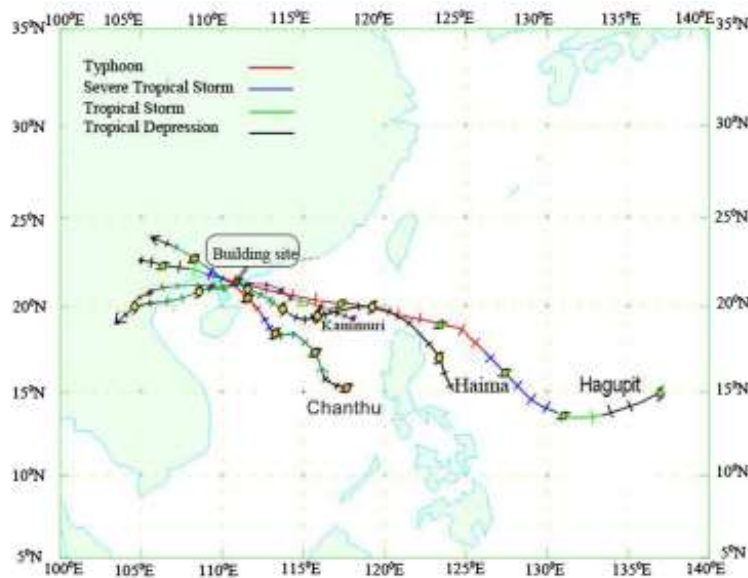
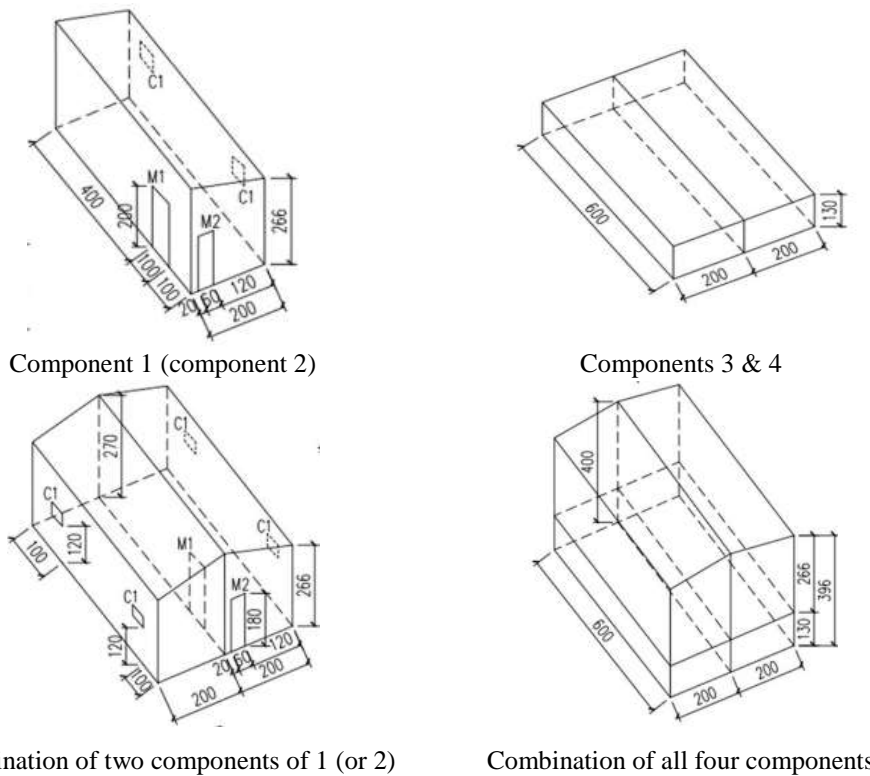


Figure 2-53. Building site and previous typhoon paths (Li et al. 2012b)

2.4.2.2 Building Fixity

The instrumented structure can be a permanent one located at a specific site or a mobile one that can be located at a site of interest. The mobile structures can be built as modular systems intended to be transported and assembled as needed. For example, the HNU building is a movable structure constructed with four modules as shown in Figure 2-54.



(a) Schematic diagram of the four prefabricated metal components (All units are in cm)



(b) The assembled HNU building

Figure 2-54. The movable HNU experimental building (Li et al. 2017a)

2.4.2.3 Building Orientation

The building is generally oriented towards the dominant wind direction. Since knowing the loads and the structural response under different wind directions is very important, in certain cases, the test structure is mounted on a turntable or a similar structure that allows changing building orientation as desired. Two such examples are the Texas Tech University (TTU) test building structure presented in section 2.4.6.1 and the Silsoe cube presented in Appendix C.

2.4.2.4 Building Details and Features

A test structure mainly consists of two parts: the base structure and the roof. The base structure includes several characteristics such as the size (length, width, and height), number of stories, number/size/location of openings (doors, windows and ventilation openings), internal compartmentalization, etc. The roof characteristics include roof slope (flat or pitched), components and the arrangement of the roof system, overhangs, and other aerodynamic features and devices. The base structure and roof characteristics are defined based on the experimental program objectives. The roof can be designed to have a flexibility for changing the pitch, as in the Aylesbury experimental building (see Appendix C) and the TTU experimental building (discussed in Section 2.4.6.2). Openings and internal compartmentalization can be designed to provide adequate flexibility for changing the size and location to alter internal pressure distribution.

2.4.3 Flow (Wind) Measurement Equipment/System

The characteristics of approaching wind are generally measured using equipment mounted on a meteorological tower or on a mast. The meteorological tower or the mast is stationed at a safe distance away from obstacles to avoid the disturbance caused by eddies generated from these obstacles. The wind speed and/or wind direction, atmospheric temperature, barometric pressure, and relative humidity are measured. Figure 2-55 shows the location and orientation of the meteorological tower with respect to the TTU test building.



Figure 2-55. Location of the meteorological tower and the TTU experimental building (Smith et al. 2017)

The following sections describe the typical equipment used for measuring wind flow characteristics.

2.4.3.1 Wind Speed and/or Direction

The speed and/or the direction of flow is measured using anemometers and vanes. Cup anemometers (3 cup or 4 cup), propeller anemometers, ultrasonic anemometers (2 axis or 3 axis), and hot wire anemometers are a few common types. Cup anemometers are the simplest type of anemometers in use. A cup anemometer consists of hemispherical cups, each mounted at the end of a horizontal arm. The horizontal arms are spaced at equal angles to each other on a vertical shaft. When a wind passes across the cups in a horizontal direction, the cups turn at a speed proportional to the passing wind speed. The average wind speed is taken as the distance completed through the turns of the cups over a period of time. Figure 2-56(a) shows a 3-cup anemometer. The vane attached to the anemometer in Figure 2-56(a) indicates the wind direction. The propeller vane assembly, shown in Figure 2-56(b), consists of a propeller and a vane connected to the two ends of a rotating horizontal shaft. The propeller has three or four blades that rotate under the horizontal wind while the vane keeps the propeller facing into the wind. The rotating horizontal shaft inserted into a coil generates an electric current or a voltage difference proportional to the wind speed. The wind vane in Figure 2-56(b) indicates the wind direction (Katsaros 2001). As shown in Figure 2-56(c), the three propeller anemometer system has the ability to measure wind from three orthogonal directions. Ultrasonic anemometers, shown in Figure 2-56(d) and Figure 2-56(e), are capable of detecting wind speed and direction. The ultrasonic anemometers measure the time taken by short sound pulses to travel from an emitter to a receiver under the disturbances from the prevailing wind. Three sound paths allow the evaluation of three components of the wind. Figure 2-56(d) is a 2-axis anemometer which measures only the wind velocity in 2 orthogonal directions. Figure 2-56(e) is a 3-axis anemometer which measures wind velocity in 3 orthogonal directions. Typically, three velocity components are evaluated according to the U, V, W axis system. Even though ultrasonic anemometers do not have many moving parts they are affected by water intrusion from rain. All three types of anemometers are affected by snow (Katsaros 2001). Figure 2-56(f) shows a hot wire anemometer. In a hot-wire anemometer, a very thin wire gets heated up to a temperature that slightly exceeds the atmospheric temperature. This heated wire cools down due to passing wind across it. Since electrical resistance of most metals

depends on the temperature of the metal, the velocity can be recorded once the relationship between resistance of the wire and temperature is established.



Figure 2-56. Wind speed and/or direction measuring instruments

Typically, these anemometers are mounted on the meteorological tower at different heights to capture characteristics of the approaching wind profile. The wind data are captured during specified time intervals to obtain the time varying wind profiles at a given location. The measured time-velocity variation is used for calculating the turbulence characteristics of the wind, such as the turbulence intensity profile.

In addition to the wind velocity measurement equipment, thermometers and barometers are used to measure atmospheric temperature and pressure. The liquid-in-glass thermometers were

the first type of instruments to be used for temperature measurements. Lately, the electronic temperature sensors are used to record the minimum and maximum temperatures. These sensors have a shielding to reduce the exposure to extra solar radiation. The wind or air flow through the covering contacts the sensors.

2.4.4 Pressure Measurement System

A pressure measurement system generally consists of pressure taps, pressure transducers, and a network of flexible tubes. Holes are drilled through the roof or walls on which the pressure needs to be measured, and short tubes typically made of stainless steel or copper are inserted into these holes. The top of the tubes, the pressure taps, are flush with the top surface of the hole (Ho-Tak 1988). A denser pressure tap layout is installed in areas where more data needs to be captured. A network of flexible tubes made of silicone, vinyl, or plastic connects pressure taps to pressure transducers. These pressure transducers generate analog electric signals that are interpreted by a computer. Figure 2-57 shows a schematic of a typical connection between a pressure tap and a transducer. The U-shape tubing shown in Figure 2-57 acts as a rain trap.

Gauge pressure, absolute pressure, and differential pressure transducers are the three types available in the market. The gauge pressure transducer measures the pressure with reference to the atmospheric pressure. The absolute pressure transducer measures the pressure with reference to a vacuum. The differential pressure transducer measures the pressure between two ports. All these transducers generate an output signal in proportion to the deflection of an in-built diaphragm that has a piezoelectric sensor. The pressure transducers are housed in a common scanning system with 12, 16, 32 or 64 pressure transducer channels. The scanning system has the reference pressure, which is typically the atmospheric pressure, as a common input port. Figure 2-58 shows the components of a pressure measurement system used for measuring the pressure distribution over a roof tile.

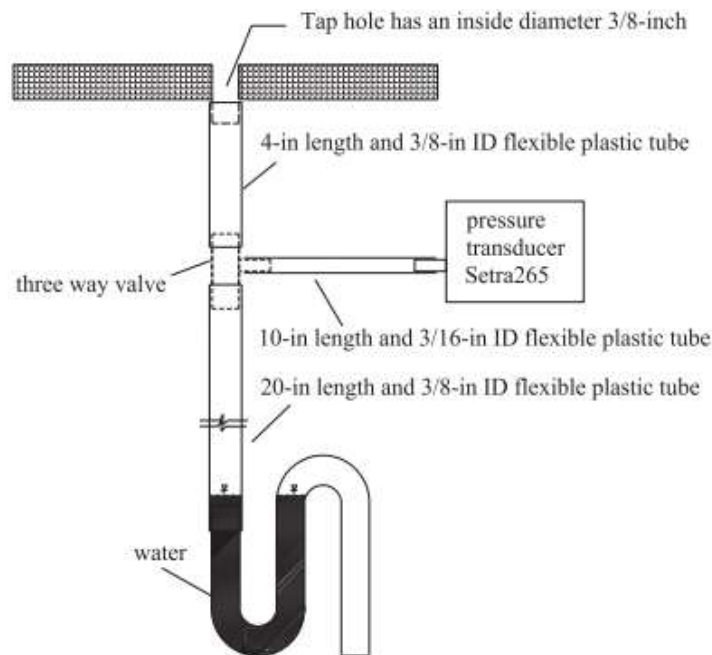


Figure 2-57. Schematic diagram of the pressure measurement system with rain traps (Li et al. 2012a)



Figure 2-58. Pressure scanner (scanning system) connected to a model tile (Masters and Gurley 2011)

2.4.5 Structural Response Measurement System

Primarily, deformations and forces are measured to understand the structural response due to wind loads. The following sections provide an overview of typical deformation and force monitoring sensors.

2.4.5.1 Deformation

The deformation of roofing membrane and other roofing components is measured as part of any monitoring program. The challenges of using traditional sensors are discussed in Attanayake and Aktan (2019). Figure 2-59 shows few commercially available non-contact displacement sensors. The selection of a suitable displacement sensor depends on the type of application, required

accuracy, number of devices and the installation cost. The use of non-contact sensors has an advantage over the contact type, as the roof needs not be damaged in order to install the sensor. The induction sensors are possible only if the target component is made of a conductive material that can induce a current (Keyence Corporation 2019).

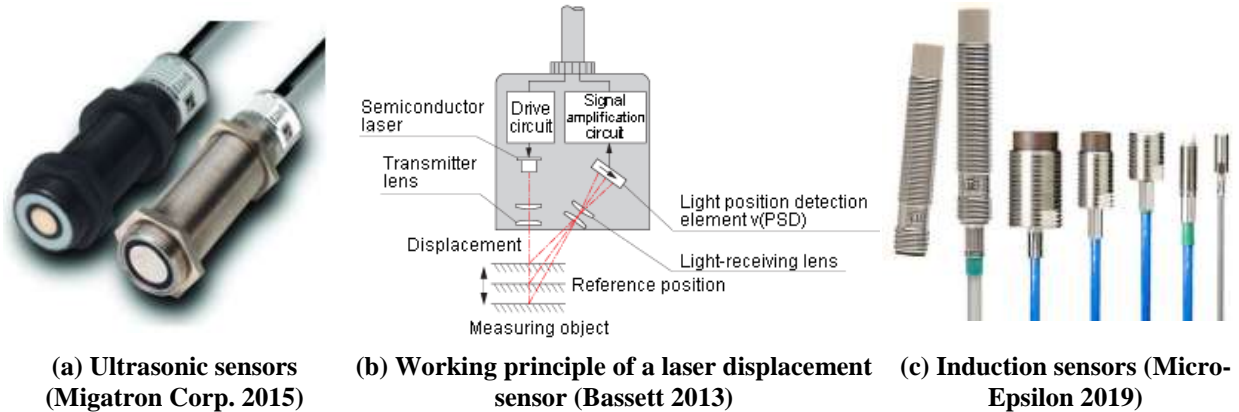
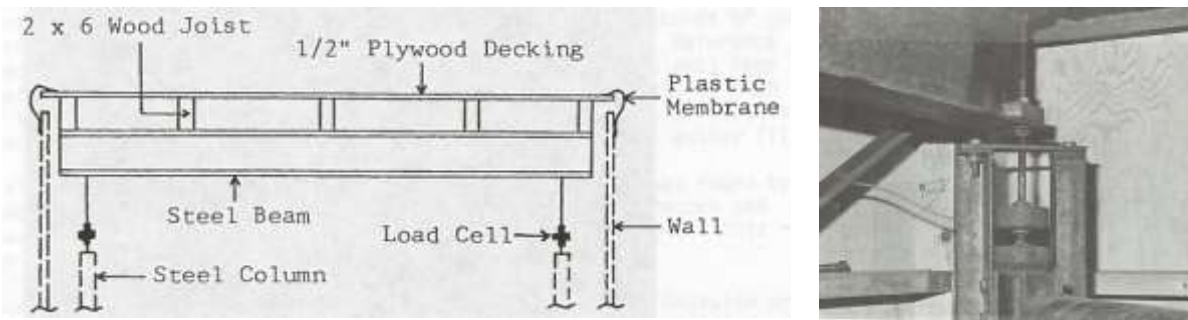


Figure 2-59. Displacement sensors

2.4.5.2 Forces

Strain gauges and load cells are typically used to measure forces in structures subjected to wind loads. Two common types of strain gauges: wire strain gauge and semiconductor strain gauge, are used in practice (Hufnagel and Schewe 2007). The forces and/or torques induced in the roofing fasteners and the supporting structural members due to wind loads are commonly measured. As an example, Figure 2-60 shows the placement of load cells to measure fluctuating wind load on a flat roof system. Load cells are placed at the four corners of the roof and underneath the steel beams (Kim and Mehta 1980).



(a) Schematic of the load cell arrangement

Figure 2-60. Details of a force measurement system (Kim and Mehta 1980)

2.4.6 Data Acquisition and Data Processing System

As shown in Figure 2-61, a data acquisition system (DAS) consists of three main components;

- (i) sensors to measure a physical phenomenon and convert it into a measurable electric signal
- (ii) a data acquisition (DAQ) device to read the electric signal from the sensor, condition and convert the signals from analog to digital, and transfer (bus) to the computer
- (iii) a computer with programmable software such as Microsoft Excel and Matlab to process, visualize and store the measured data (National Instruments 2019a).



Figure 2-61. Components of a data acquisition system (National Instruments 2019a)

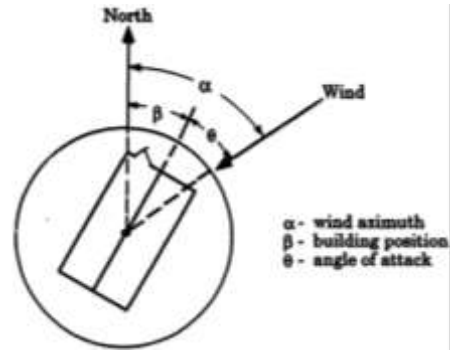
2.4.6.1 Case Study 1: Texas Tech University (TTU) Experimental Building

The wind research facility at Texas Tech University (TTU) features a field test building with a pressure measurement system to study the effect of wind induced pressures on a low-rise building. This facility was constructed in 1989 and is known as the Wind Engineering Research Field Laboratory (WERFL). The data produced by the facility has been used in the validation of wind tunnel and computational fluid dynamic simulation results (Smith et al. 2017). As shown in Figure 2-62(a), the test building is a prefabricated steel model with dimensions of $30 \times 45 \times 13$ ft ($9.1 \times 13.7 \times 4.0$ m). The building has a nearly flat roof, and a minor slope of 1:60 is provided for drainage (Ho-Tak 1988). The building is anchored to a rigid steel undercarriage with wheels at four corners. These wheels are guided by a circular steel rail track embedded to a concrete slab. Hydraulic jacks placed at each corner allow the test building to be raised up to 3 in. and rotated 360° in 15° intervals using a pair of electric motors. The rotation allows the building to be oriented at a required incident wind angle. Once the building is rotated to the required angle, the building is lowered and secured to the anchor bolts embedded in the concrete slab. These anchor bolts are installed at every 15° interval around the circle. The building position is defined as the angle between the longitudinal axis of the test building and the true north, as illustrated in Figure 2-62(b). The direction of the wind is the difference between the wind azimuth and the building position.

The field site is surrounded by a flat and open terrain (Levitan and Mehta 1992a, Levitan and Mehta 1992b). The exterior wall coverings of the building are corrugated steel panels attached with self-tapping screws at a 1-ft center to center spacing. At the bottom of the building, a rubber gasket skirt seals the gap between the building and the concrete slab (Ho-Tak 1988).



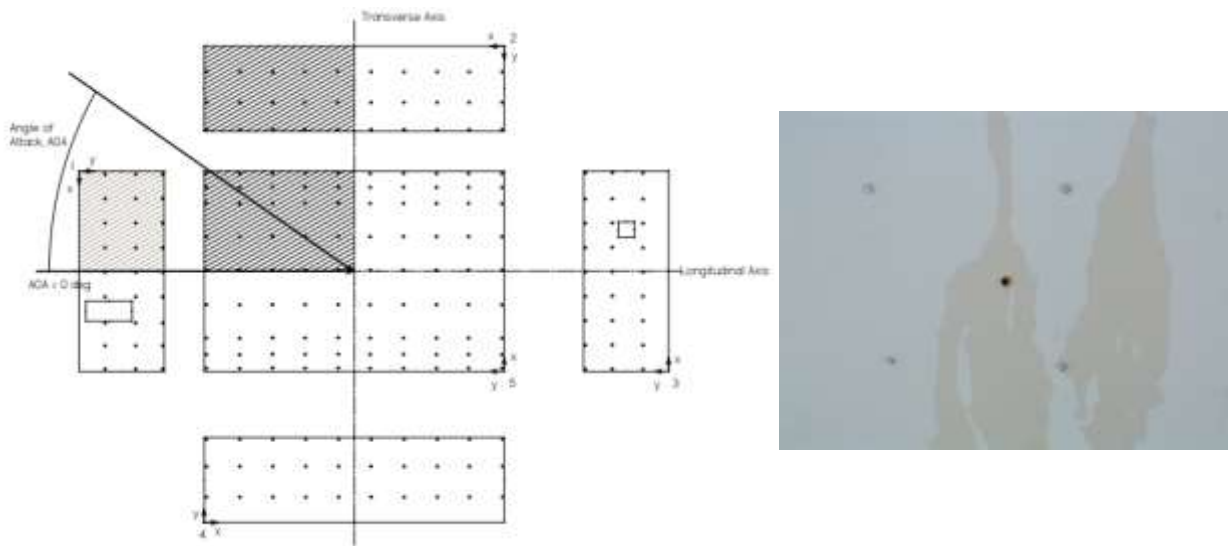
(a) WERFL at Texas Tech University (Smith et al. 2007)



(b) Wind azimuth and angle of attack (Levitan and Mehta 1992a)

Figure 2-62. Wind Engineering Research Field Laboratory (WERFL) of Texas Tech University (TTU), U.S.

As shown in Figure 2-63(a), more than 100 pressure taps are installed on the roof and on the walls of the test building with a denser layout near the roof corners and edges. These pressure taps have an internal diameter and a length of 5/16 in. and 2 in., respectively. The pressure taps are mounted flush with the external surface of the building as shown in Figure 2-63(b). Each tap is designated with a 5-digit number; sxxyy where 's' defines the building surface, while 'xx' and 'yy' represent the nominal coordinates (in ft) of the tap on the given surface. The short wall with the door is numbered as 1, and the rest of the walls are numbered in a clockwise manner. A local coordinate system is defined on each wall (Levitan and Mehta 1992a).



(a) Pressure tap locations on the test structure

(b) Pressure taps installed in a wall

Figure 2-63. Pressure tap layout on the TTU building (Smith et al. 2017)

Forty-seven differential pressure transducers are installed to measure external and internal pressure developed on the building. Details of the pressure transducers such as the type, model, manufacturer/ supplier and full scale range are given in Table 2-10. Electrical solenoid valves used for online calibration are mounted along with the pressure transducers. The pressure taps installed at the walls and roof of the test building are connected to the solenoid valves and then to the transducers using flexible plastic tubing. Figure 2-64 shows the layout of the tubing connecting the pressure taps, solenoid valves, and the transducers on the inside of the test building. The ambient pressure is considered as the reference pressure for the transducers. The reference pressure is captured using a buried box with a smooth lid that is flushed at the ground level and located at 75 ft west of the test building. The lid has a 0.5 in. diameter hole. An 8 in. diameter tube connected between the box and the building maintains the atmospheric pressure to be used as the reference at the building. A 3/16 in. diameter tubing connects the reference pressure to each of the pressure transducers. A restrictor tubing of 1/32 in. is placed in the reference pressure lines to maintain a time constant of about 13 sec, so that any changes in the reference pressure is recorded while dampening out any high frequency noise.

Table 2-10. Pressure Transducer Details in TTU Building (Levitan and Mehta 1992a)

Number of transducers	Type	Model	Supplier / Manufacturer	Full Scale Range	Details
13	Variable reluctance	Model DP103	Validyne Engineering Corp	± 0.2 psi with ± 0.0005 psi accuracy	Rugged, versatile and expensive. Signal conditioning is provided by Validyne Engineering Model CD19A Carrier Demodulators.
4				± 0.32 psi with ± 0.0008 psi accuracy	
30	Solid state piezo resistive with a fixed silicon diaphragm	OMEGA Engineering Model PX 163-005 BD 5V	MicroSwitch	± 0.18 psi with ± 0.0009 psi accuracy	Relatively less rugged and versatile. Cost about 1/4 th the cost of Validyne. Signal conditioning is custom built.

In addition to differential pressure transducers, displacement transducers and load cells are installed to measure displacements and forces. Figure 2-60 illustrates the load cell arrangement. Sensors installed on the doors and windows provide information as to whether they are open or closed when collecting the internal pressure data.

**Figure 2-64. Arrangement of pressure measurement tubing and instruments on the roof (Smith et al. 2007)**

The facility has a 160 ft high guyed tower as shown in Figure 2-65. All the meteorological instruments are installed on this tower at six different heights: 3, 8, 13, 33, 70, and 160 ft. Different types of anemometers, manufactured by the R. M. Young Company, are used for wind velocity measurement. The details of the anemometers are provided in Table 2-11. Booms extending from the tower are oriented to receive an unobstructed wind flow to the instruments. Four 3-cup anemometers are placed at 3, 13, 70, and 160 ft levels in the tower, and one 3-cup anemometer is placed on a 13 ft high pole located halfway between the tower and the test building. The direction vanes are installed at 13 ft and 160 ft, and the UVW anemometers are installed at 8 ft and 33 ft.

In addition to the anemometers, a Model BP-100 sensor manufactured by Teledyne Geotech, with a rated resolution of 0.012 in. Hg records the barometric pressure. A Model RH-200 sensor with a rated accuracy of $\pm 3\%$ measures the relative humidity while a platinum temperature sensor built into the unit, rated at $\pm 0.2^\circ\text{F}$, measures the ambient temperature. The temperature, pressure and relative humidity sensors are installed at 160 ft on the tower (Levitan and Mehta 1992a).



Figure 2-65. Meteorological tower located at WERFL (Smith et al. 2007)

Table 2-11. Details of the Anemometers (Levitan and Mehta 1992b)

Type of Anemometer	Number of Instruments	Model	Measured Parameter	Features
Gill 3-cup anemometer	5	Model 12102	Wind speed	Maximum range: 112 mph Distance constant (63% recovery): 8.9 ft
Gill Microvanes	2	Model 12304	Wind direction	Rated delay distance (50% recovery): 3.6 ft
Gill UVW anemometers	2	Model 27005	Wind velocity	Rated range: 90 mph Distance constant (63% recovery): 6.9 ft

The DAS is housed inside a concrete block building placed within the rotatable test building. This concrete block building has reinforced concrete masonry walls and a cast-in-place concrete roof. A 20 MHz 80386-based PC is used for the data acquisition (Ho-Tak 1988). The incoming signals are captured by a MetraByte Corp. DAS-8 analog to digital (A/D) conversion board with 8 channels. Three MetraByte compatible CIO-MUX32 multiplexors, from Computer

Boards Inc., expand the input capacity to 96 channels. LabTech Notebook software, from the Laboratory Technologies Corp., running in a DOS environment drives the A/D board. All the tubing and connections in the DAS to the external test building are made through a small hole in the center of the roof slab of the concrete block building. This prevents the disconnection and connection involved whenever the test building is rotated and oriented. The DAS runs continuously measuring the wind speed, but records data when one-minute mean wind speed exceeds 20 mph. In case of any disruption to the regular power supply, two battery backup power supplies are available to run the DAS and all the instrumentation for approximately one hour. The data collected through the DAS is processed in data analysis systems. Most of the data analysis systems run on personal computers. Preprocessor software is custom written in Microsoft QuickBasic and C++ and provides a summary of the data for each instrument while producing time history plots (Ho-Tak 1988, Levitan and Mehta 1992a, Smith et al. 2017).

In addition, a quality assurance program is in place for data collected through this system. Three major components of the quality assurance program are (i) daily check of the field laboratory, (ii) frequently scheduled instrument calibration and maintenance, and (iii) timely preliminary analysis of the collected data (Levitan and Mehta 1992a).

2.4.6.2 Case Study 2: Tongji University (TJU) Building (Huang et al. 2012, Xu et al. 2012)

In 2008, a field laboratory involving a test building and a meteorological tower was set up by the state Key Laboratory of Disaster Reduction in Civil Engineering of Tongji University (TJU), China. Figure 2-66 shows the details of this experimental facility. The aim of this test facility was to study the turbulence characteristics near the ground and the wind effects on low-rise buildings. The test building is made of steel and has plan dimensions of 32.8×19.7 m (10×6 m) and an eave height of 26.2 ft (8 m). The building has three internal stories with heights 9.8 ft (3 m), 8.2 ft (2.5 m) and 4.9 ft (1.5 m). The data collection and recording equipment are located in the middle story.

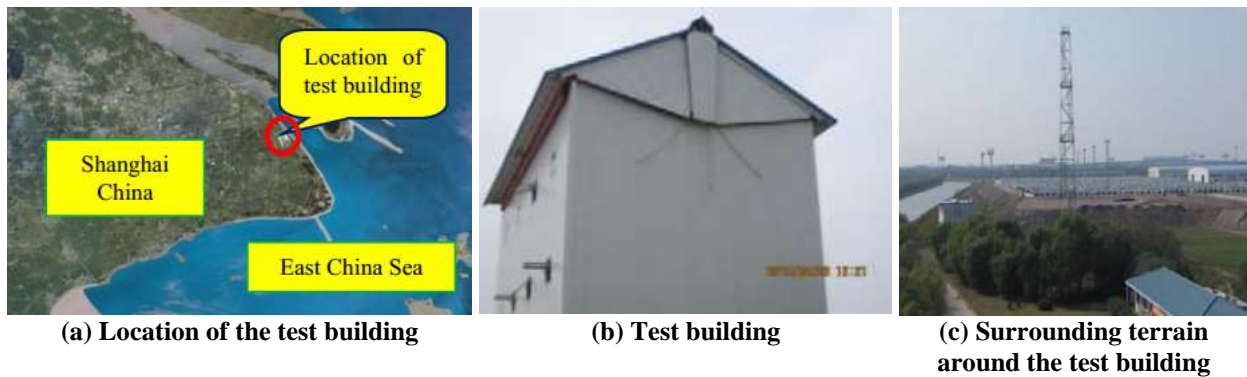


Figure 2-66. Test building location, shape, and the terrain conditions (Xu et al. 2012)

The roof pitch of the test building can be adjusted from 0° to 30° . A hinged design is used at the connection between the ridge beam and the roof as shown in Figure 2-67(a); consequently, when the ridge beam is elevated, the roof pitch is changed accordingly. This elevating mechanism of the roof is illustrated in Figure 2-67(b). The slide-guiding device shown in Figure 2-67(c) maintains the stability of the roof by controlling the motion of the gable end beams. Three lifting devices (one active lifting device and two passive devices as shown in Figure 2-67(d) and (e), respectively) are installed on the columns. The middle column of the test building carries the active lifting device.

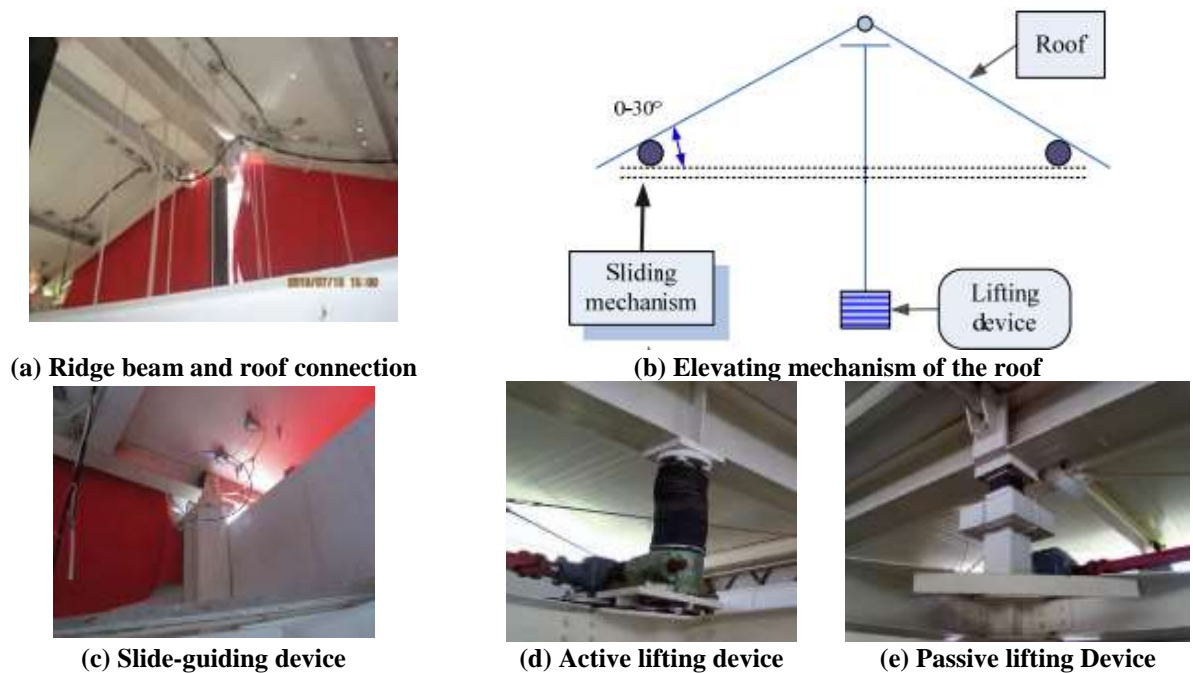


Figure 2-67. The roof lifting mechanism and details (Xu et al. 2012, Huang et al. 2012)

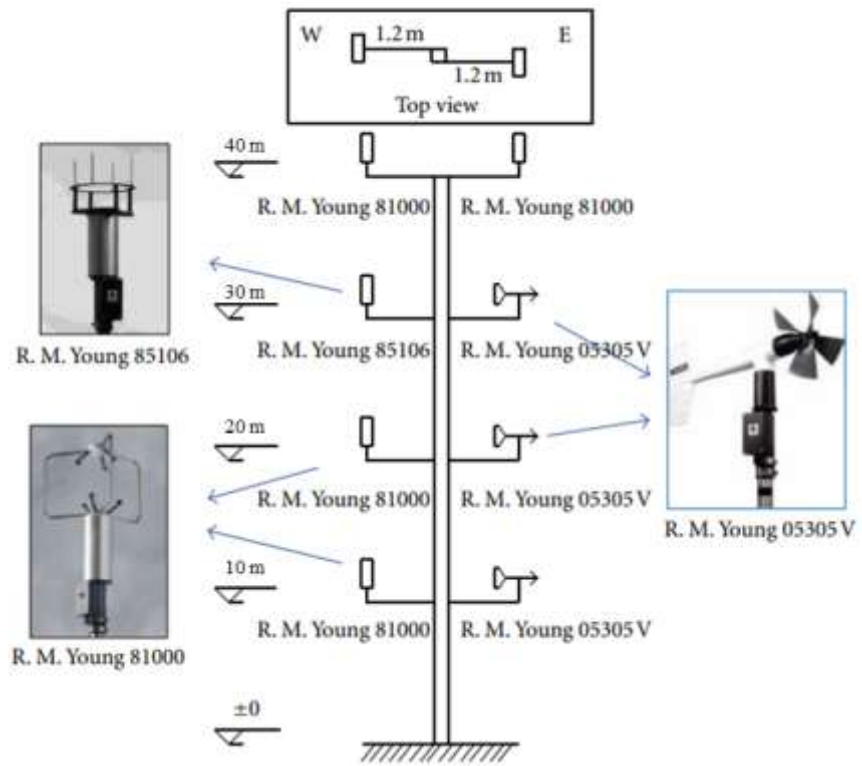
Two self-supporting meteorological steel towers of heights 32.8 ft (10 m) and 131.2 ft (40 m) are located in the field to record wind characteristics. The 32.8 ft tower, shown in Figure 2-68(a), is located 82 ft (25 m) to the east of the test building and supports two anemometers at the top of the tower. The 131.2 ft tower is located at about 114.8 ft (35 m) to the north of the test building. The tower has eight anemometers mounted at 32.8, 65.6, 98.4, and 131.2 ft (10, 20, 30, and 40 m) heights. Figure 2-68(b) and Figure 2-68(c) show the tower and the locations at which the instruments are installed on the tower. Three types of anemometers (R. M. Young 81000, 85106, and 05305V) are installed on the tower. The specifications of these three anemometers are given in Table 2-12.



(a) 10 m tower and the location of anemometers



(b) 40 m tower



(c) Location of anemometers on the 131.2 ft (40 m) tower

Figure 2-68. Details of the meteorological towers at theTonji University (TJU) experimental facility (Huang et al. 2012)

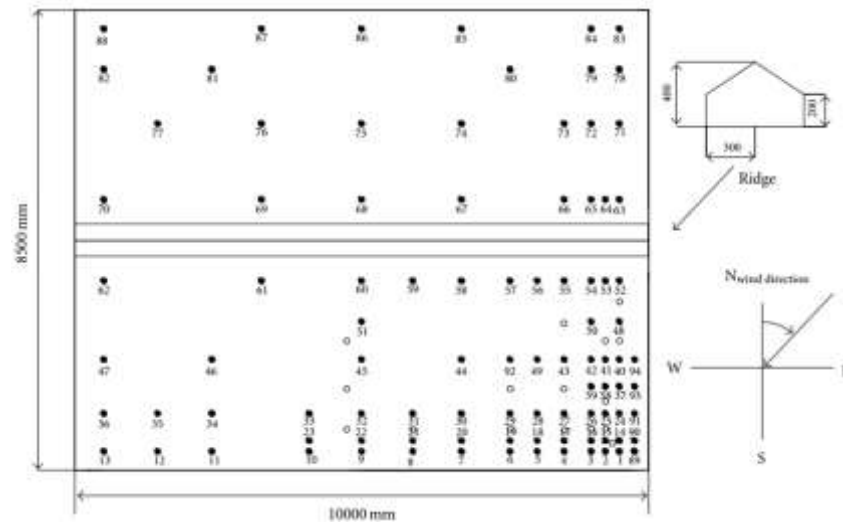
Table 2-12. Specifications of the Anemometers (Huang et al. 2012)

Measurements and Specification		Anemometer Model		
		R.M.Young 81000	R.M.Young 85106	R.M.Young 05350 V
Wind speed	Range	0~40 m/s	0~70 m/s	0~50 m/s
	Resolution	0.01 m/s	0.1 m/s	-
	Accuracy	±0.05 m/s (0~30 m/s)	±0.1 m/s (0~30 m/s)	0.2 m/s
Wind direction	Horizontal Range	0~360°	0~360°	0~360°
	Vertical Range	±60°	0	0
	Resolution	0.1°	1°	-
	Accuracy	±2° (1~30 m/s)	±2°	±3°
Sampling frequency		4-32 Hz (20 Hz used)	1 Hz	20 Hz
Working temperature		-50~50°C	-50~50°C	-50~50°C

Pressure taps are installed on the roof. Two types of pressure transducers: CYG 1220 and CYG 1516, are used in this facility. The specifications of pressure transducers are given in Table 2-13. The layout of the pressure taps and the top and underneath view at a roof corner is shown in Figure 2-69. The prevailing wind at the site is in southeast direction. Therefore, a dense layout of pressure taps is installed at the southeast corner of the roof as shown in Figure 2-69(a).

Table 2-13. Specifications of the Pressure Transducers (Huang et al. 2012)

Parameters	Transducer	
	CYG 1220	CYG 1516
Pressure Range	0 ~ ±1 kPa	0 ~ ±2.5 kPa
Response frequency	More than 20 Hz	More than 200 Hz
Input voltage	DC 24V	DC 24V
Output signal	4 ~ 20mA	4 ~ 20mA
Rated accuracy	Less than 0.5% FS	Less than 0.5% FS
Operating temperature	0 ~ 50°C	0 ~ 50°C



(a) Layout of the roof pressure taps (●: CYG 1220 ○: CYG 1516)



(b) Top surface at the roof corner



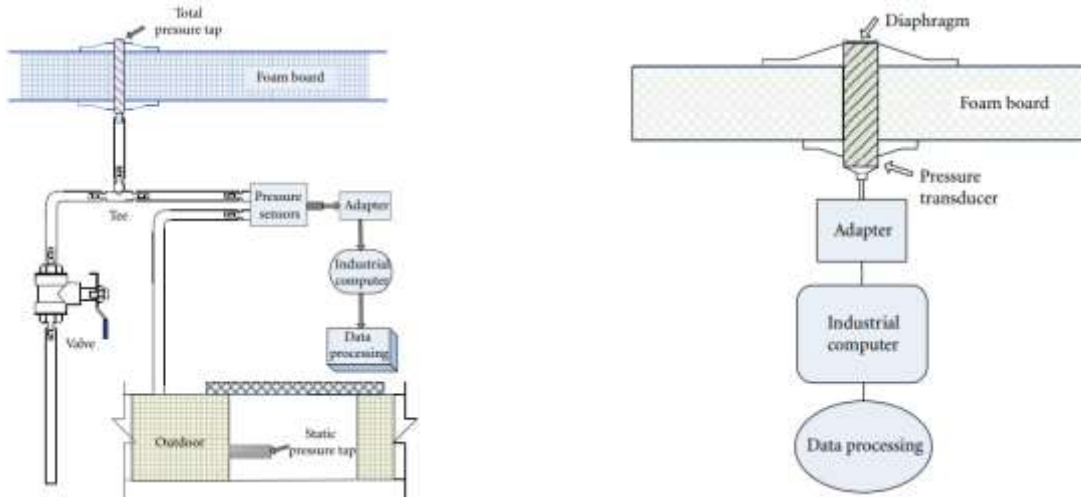
(c) Underneath of the roof corner

Figure 2-69. Pressure tap layout (a) and the top and underside views of the roof (b and c) (Huang et al. 2012)

The CYG 1220 are micro differential pressure sensors, and the CYG 1516 are diaphragm pressure sensors. Figure 2-70(c) and (d) show the CYG 1120 and CYG 1516 pressure sensors, respectively. There are 94 CYG 1220 micro differential pressure sensors installed on the inside of the steel roof to capture wind pressure data without the effect of rain. Figure 2-70(a) illustrates the pressure measurement system with a CYG 1220 differential pressure sensor. A tube extended from the pressure tap connects to a tee. One end of the tee connects to the active side of the CYG 1220 pressure transducer through a tube, and the other end of the tee connects to a valve to collect the rainwater seeped through the pressure tap. The passive end of the transducer is connected to a box located outdoors to obtain the reference or the ambient pressure.

There are 20 CYG 1516 diaphragm pressure sensors installed under the roof to study the wind-rain-induced effects on pressure. The structure and the diaphragm of these transducers

consist of stainless steel to prevent the rainwater intrusion. The pressure measurement system with a CYG 1516 sensor is illustrated in Figure 2-70(b).



(a) Pressure measurement system for CYG 1220 sensor (b) Pressure measurement system for CYG 1516 sensor



(c) CYG 1220 pressure sensor



(d) CYG 1516 pressure sensor

Figure 2-70. Pressure measurement system (a and b) and the respective pressure sensors (c and d) (Huang et al. 2012)

Two adapters, supplied by the National Instruments Corporation, capture the incoming signals. Each adapter consists of 80 channels and a 16-bit A/D converter. The sampling frequency of each adapter is 20 Hz. Before collecting the data, the zero calibration of all the transducers is checked. An industrial computer is used for the data acquisition. Figure 2-71 shows the adapters and the computer.



(a) Adapter



(b) Industrial computer

Figure 2-71. The adapter and the computer used in the DAS (Huang et al. 2012)

2.5 SUMMARY

Post hurricane investigations have revealed that flat and steep sloped roof damages are predominantly initiated at roof edges and corners. Peak suction forces resulting from conical vortices at roof corners and separation bubbles at roof edges are the primary reasons for such damages. For this reason, the roof corners and edges are typically termed as high-pressure zones. Therefore, several damage mitigation approaches were developed and evaluated. The aerodynamic flow patterns and the pressure distribution before and after implementation of such mitigation methods were studied numerically and experimentally to evaluate their effectiveness. The experimental studies have been performed as scale model testing or full-scale testing under simulated or natural wind conditions. The two basic aerodynamic mitigation approaches are the modification of the existing roof geometry or the installation of an aerodynamic mitigation feature/device. Parapets, splitters, spoilers, pergolas, flow dividers, etc., are a few examples for aerodynamic devices. Chamfering, rounding, and recessing are examples for roof edge geometry modifications or damage mitigation features. A detailed summary of these devices and features and their effectiveness is presented in Chapter 5.

A majority of experimental studies are conducted using scale models under simulated winds. Since it is unclear how the prototype structures will respond to natural wind loading, a few prototype buildings were designed, fabricated, instrumented, and installed at several selected sites. The instrumentation on these buildings includes pressure sensors, load cells, strain gauges, displacement measurement devices, etc., to monitor pressure distribution on the building envelope and structural response under natural wind conditions. The characteristics of the approaching wind were measured using meteorological towers instrumented with anemometers, vanes, and temperature, humidity, and pressure sensors. The data gathered through these studies have been used for the validation of numerical models and to verify the accuracy of scaled model wind tunnel testing results.

3 NUMERICAL SIMULATION OF THE FLOW AROUND A FLAT ROOF OF A LOW-RISE BUILDING

3.1 OBJECTIVE AND APPROACH

The objective of this chapter is to develop a numerical model to investigate the pressure distribution over a flat roof of a low-rise building using available numerical simulation tools. Computational Fluid Dynamic (CFD) simulation tools are used for investigating air flow patterns around objects such as buildings and calculating the loads acting on such structures. Even though a large number of CFD simulation tools are available in the market, this research team selected Ansys Fluent after reviewing past experience documented in literature. The team has access to the software with an academic license. The numerical model was validated using experimental data available on a full-scale experimental structure known as the Silsoe cube. The pressure coefficients on the windward wall, roof and the leeward wall along the mid-width of the building are calculated using simulation results. These coefficients are then compared with the available experimental data to demonstrate the expertise of the team to use such tools in future projects to investigate wind-structure interaction for the design of experiments and evaluation of various options for mitigating roof damage under high wind loads.

3.2 EXPERIMENTAL STRUCTURE

A 6 m cube with a smooth surface finish was fabricated at the Silsoe Research Institute in the UK to study wind-structure interaction (Richards et al. 2007). This cube is known as the Silsoe cube and placed in an open terrain. Figure 3-1 shows the pressure taps located along the vertical and horizontal centerlines of the cube surface. Ultrasonic anemometers, located on a reference mast at a distance (1.04 times the height of the cube) away from the cube, record the approaching wind profile velocity. The cube is located on a turntable such that the cube can be rotated to orient towards a desirable wind direction. Several wind tunnel studies and numerical studies have been conducted on scaled models of this Silsoe cube (Richards et al. 2007, Irtaza et al. 2013, Enteria 2016). The data recorded from the full-scale Silsoe cube is used for validation of experimental and numerical simulation results. The experimental data recorded from the full-scale structure and published in Richards and Hoxey (2012) is used to validate the numerical model developed for this study.

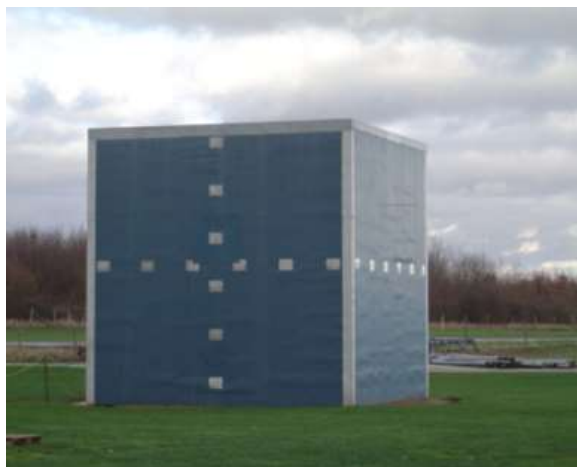


Figure 3-1. Silsoe cube (Richards and Hoxey 2012)

3.3 NUMERICAL MODEL

A numerical model of the 1:30 scaled Silsoe cube used for wind tunnel testing by Irtaza et al. (2013) was developed. Figure 3-2 shows the 1:30 scale model tested by Irtaza et al. (2013). Irtaza et al. (2013) developed a numerical model using Ansys Fluent and validated the results with the experimental data. The input parameters used for the numerical simulation conducted in this study are similar to those measured during the wind tunnel test by Irtaza et al. (2013).

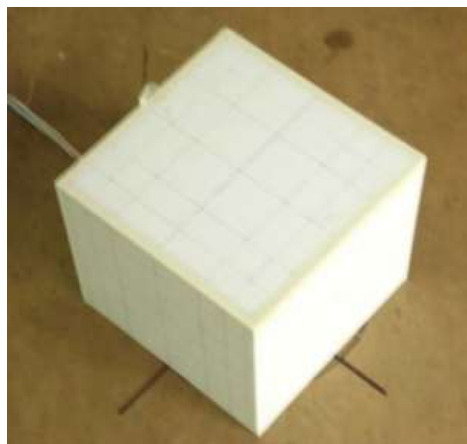


Figure 3-2. 1:30 scale model of the Silsoe cube (Irtaza et al. 2013)

Figure 3-3 shows the geometry of the numerical model. A bounding box of $14.4 \times 8.5 \times 3.9$ ft ($4400 \times 2600 \times 1200$ mm) encompassing the $7.87 \times 7.87 \times 7.87$ in. ($200 \times 200 \times 200$ mm) cube representing the low-rise flat roof building forms the computational domain. The computational domain has seven surfaces: inlet, outlet, two sides, ground, domain roof, and the building surface (walls and roof).

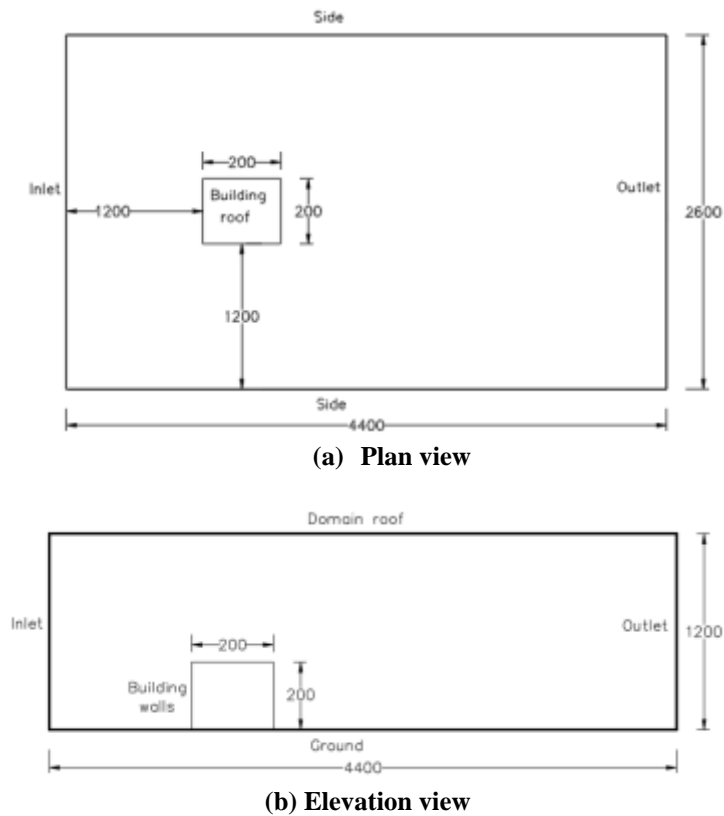


Figure 3-3. Geometry of developed numerical model; Plan view (a) and Elevation view (b)
 (All dimensions are in mm, 25.4 mm = 1 in.)

In order to capture the variation near the walls and roof of the cube, a finer mesh configuration was used for the region around the cube. Figure 3-4 shows the details of the mesh. The model has 476,466 nodes and 443,872 elements.

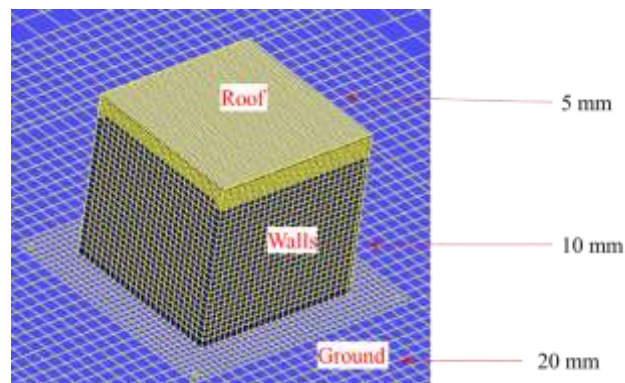


Figure 3-4. Details of the mesh near the cube

The properties of the computational domain represent the properties of air. The density and viscosity of air are 0.07647 lb/ft^3 (1.225 kg/m^3) and $1.2024 \times 10^{-5} \text{ lb/fts}^{-1}$ ($1.7894 \times 10^{-5} \text{ kg/ms}^{-1}$),

respectively. The numerical simulation was performed using five turbulence models: standard $k-\varepsilon$, realizable $k-\varepsilon$, re-normalization group (RNG) $k-\varepsilon$, $k-\omega$ shear stress transport (SST), Spalart Allmaras and Reynolds Stress model (RSM). The near wall-treatment was applied using standard wall functions. Table 3-1 describes the boundary conditions assigned to the surfaces of the computational domain.

Table 3-1. Boundary Condition Definitions

Boundary Condition	Assigned Surface	Parameters
Velocity Inlet	Inlet	Velocity magnitude is normal to the boundary. A parabolic velocity profile as shown in Figure 3-5 was imposed at the inlet. Turbulence specification method: Intensity and Length Scale Turbulent Intensity = 18% Turbulent Length Scale = 0.30 m
Pressure Outlet	Outlet	Gauge pressure = 0 Turbulence specification method: Intensity and Length Scale Turbulent Intensity = 18% Turbulent Length Scale = 0.30 m
Wall	Building walls, building roof, and ground	Stationary wall No slip conditions Standard roughness model Sand roughness height = 0.01 m, roughness height = 0.5
Symmetry	Sides and domain roof	-

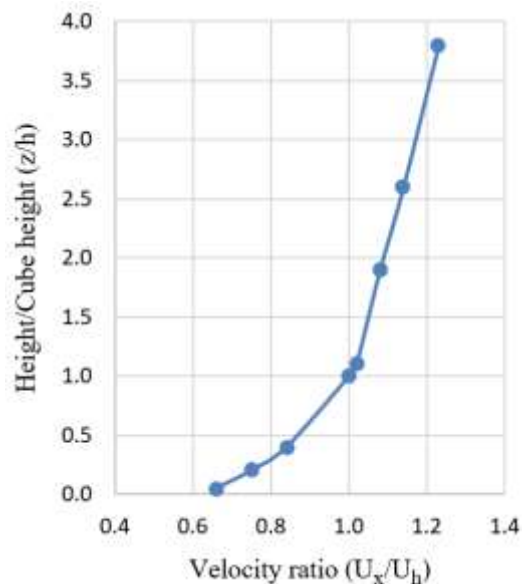


Figure 3-5. Simulated wind profile at the inlet

Note: U_x : Velocity along the flow direction, U_h : velocity at the cube height (h)

A pressure-based solver with absolute velocity formulation was used for the solver settings. A transient analysis was performed. The pressure implicit with splitting of operators (PISO) pressure-velocity coupling method (with second order implicit scheme) was used for time discretization.

3.4 RESULTS AND DISCUSSION

Figure 3-6 presents the mean pressure coefficients obtained from CFD analysis using different turbulence models and the full-scale Silsoe cube experimental data available in Richards and Hoxey (2012). The mean pressure coefficients were calculated along the path 0-1-2-3 under 90° wind direction.

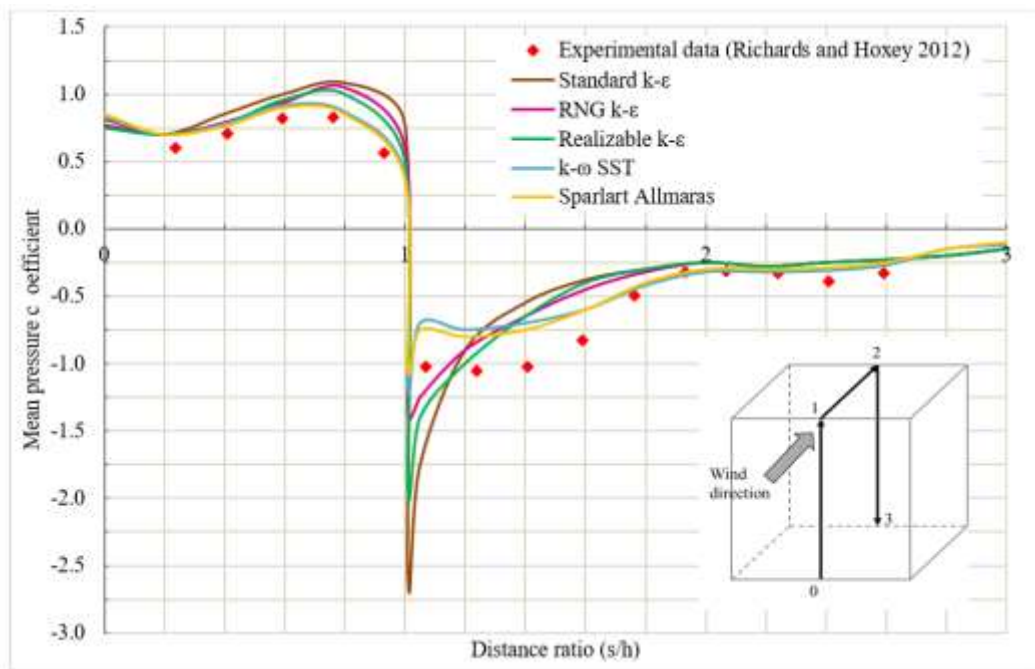


Figure 3-6. Comparison of CFD results with experimental data

Note: s: Distance along the path 0-1-2-3, h: height of the cube

As shown in Figure 3-6, the deviation of numerical and experimental results is smaller on the windward wall (0-1) and the leeward wall (line 2-3) compared to that on the roof (line 1-2). The $k-\omega$ SST and Spalart Allmaras turbulence models yielded the least deviation; this is a significant achievement with a 43k element model. A significant effort is required to optimize the available element count to minimize the observed deviation.

Enteria (2016) conducted CFD simulations of 2:3 scaled models of the Silsoe cube using OpenFoam. Figure 3-7 shows the numerical results obtained by Enteria (2016) using five different turbulence models. Similar trends to Enteria (2016) were observed during this study for all the turbulence models, especially the peak pressure at the windward edge. The pressure coefficient at the windward edge was highest for standard k- ϵ model in both studies; however, the pressure coefficient obtained by Enteria (2016) was about -2.5, whereas the pressure coefficient obtained during this study is about -1.7. Along the line 0-1, the pressure coefficients were overestimated by Enteria (2016). However, the variation of the numerical results of the pressure coefficients was minimum along line 2-3 in the results obtained by Enteria (2016). All the input parameters used by Enteria (2016) were similar to those used in this study, except for the domain size and the grid size. The total number of elements used by Enteria (2016) was about 320,000, whereas about 440,000 elements were used in this study. However, details of the mesh distribution used by Enteria (2016) around the cube is not explicitly given. Therefore, the effect of the mesh size near the cube cannot be deduced as the sole reason for the difference in the numerical results observed under the two studies.

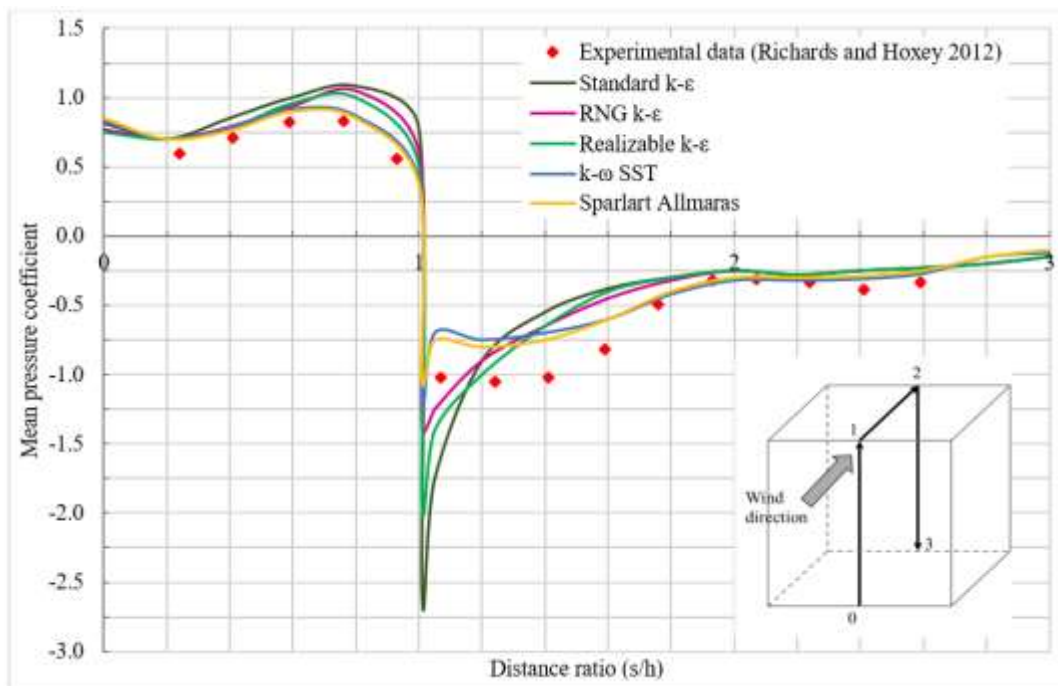


Figure 3-7. Comparison of the numerical and experimental pressure coefficients along the mid-width of the Silsoe cube by Enteria (2016)

In addition to Enteria (2016), Irtaza et al. (2013) performed CFD simulations of 1:30 scaled models of the Silsoe cube using the Ansys Fluent. Figure 3-8 shows the numerical results obtained by Irtaza et al. (2013). Similar to the numerical results obtained in this study and by Enteria (2016), a significant deviation is observed for the pressure coefficients along the line 1-2. However, the peak pressure at the windward edge is not observed in the results obtained by Irtaza et al. (2013). The input parameters used by Irtaza et al. (2013) were similar to those used in this study, but the total number of elements used by Irtaza et al. (2013) was about 4 million. Further, Irtaza et al. (2013) observed less deviation of the numerical results from the experimental data, when the large eddy simulation (LES) model was used to simulate turbulence. However, the LES was not included in the analysis presented in this chapter as a turbulence model due to the restrictions on the total number of elements in the numerical tool.

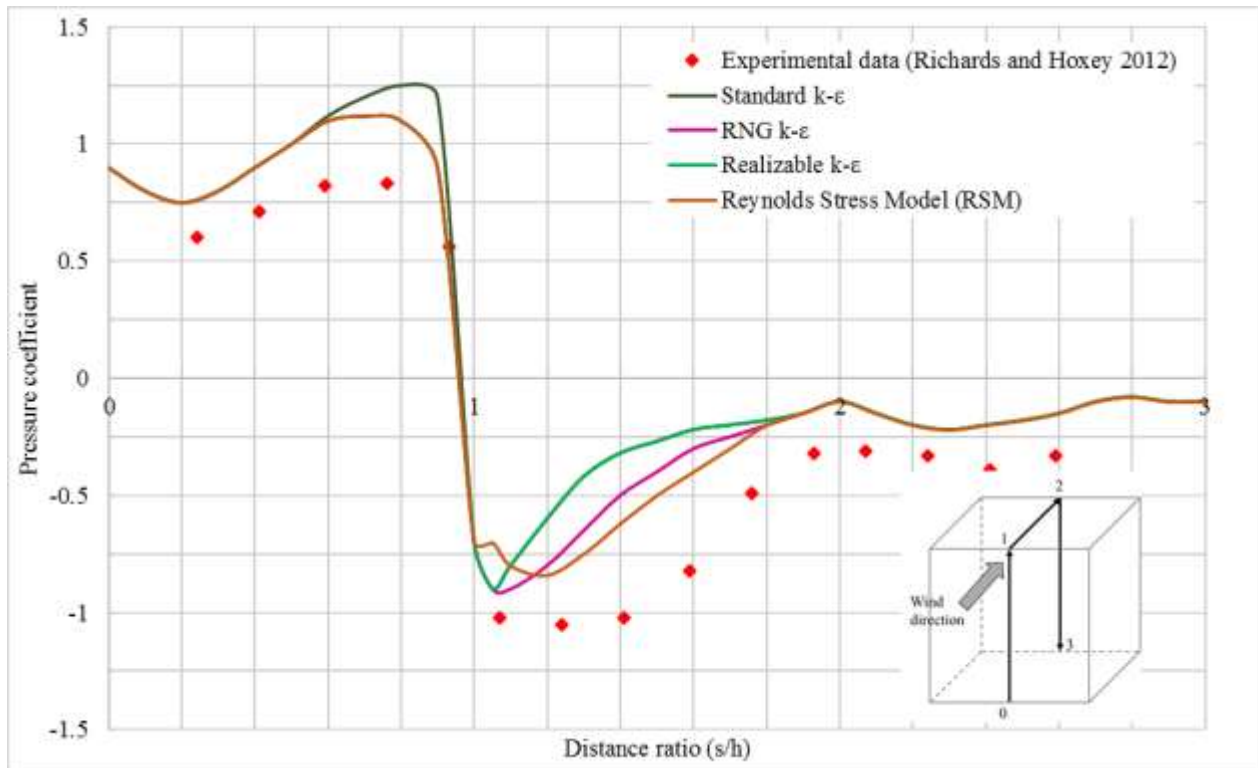


Figure 3-8. Comparison of the numerical and experimental pressure coefficients along the mid-width of the Silsoe cube by Irtaza et al. (2013)

3.5 SUMMARY AND CONCLUSIONS

A CFD model was developed to study the wind pressure distribution around a cube structure. The pressure coefficients along the mid-width of the cube along the windward wall (line 0-1), the roof

(line 1-2) and the leeward wall (line 2-3) were calculated when the wind flows perpendicular to the windward edge. Six turbulence models were used in the simulation: standard $k-\epsilon$, realizable $k-\epsilon$, RNG $k-\epsilon$, $k-\omega$ SST, Spalart Allmaras, and Reynolds stress model (RSM). Results were validated using published experimental data. The mean pressure coefficients calculated from the CFD analysis were in agreement with the experimental data at the mid-width of the cube along the windward wall but deviated significantly from the experimental pressure coefficients at the mid-width along the roof. Similar observations were reported by Irtaza et al. (2013) and Enteria (2016). However, Irtaza et al. (2013) reported the minimum deviation of numerical pressure coefficients over the roof when compared with Enteria (2013) and the study presented in this chapter. The primary reasons for such a deviation are the mesh size, the refinement around the structure to capture flow variations at the boundary layer, and the turbulence models used in the analysis. As an example, Irtaza et al. (2013) were able to closely correlate the numerical and experimental results by using a total of 4 million elements, more refined mesh around the cube structure to capture the flow variations at the boundary layer, and the large eddy simulation (LES) turbulence model. Limitations of the simulation tool available for this study restricted the use of a refined mesh and the LES turbulence model to improve the outcome. Irrespective of the total number of elements in the model, Irtaza et al. (2013) observed a deviation of the numerical results from the experimental data over the roof of the building. The possible causes for such a deviation need to be further investigated.

4 PROPOSED OUTDOOR EXPERIMENTAL FACILITY

4.1 OBJECTIVE AND APPROACH

The objective of this chapter is to provide the design details and an initial cost estimate for an outdoor experimental research facility. The aim of developing such an experimental facility is to study the response of a full-scale structure under natural wind load conditions, evaluation of the resilience of structural health monitoring systems under severe exposure conditions, evaluation of the effectiveness of roof damage mitigation details/devices, and study of heated air movement to validate fire simulation models. The details of the facility are provided in the following sections.

4.2 DESIGN DETAILS AND THE COST ESTIMATE

The information provided in this section is divided into four main topics: design details of the experimental structure, the meteorological system, the structural response monitoring system, and the data acquisition system (DAS). Each of the four topics are discussed in detail and an initial cost estimate is provided.

4.2.1 Design Details of the Experimental Structure

A modular structure is proposed as the experimental building since it can be easily moved, assembled, disassembled, and relocated as needed. The experimental building needs to be placed at different locations to monitor wind flow patterns and structural response due to uninterrupted and interrupted winds due to nearby structures. The structure is designed considering Michigan wind loads.

4.2.1.1 Details of the Structure

As shown in Figure 4-1, a $10 \times 20 \times 8$ ft modular building with four perimeter frames is proposed. The expected snow load and the wind load on the building were calculated as per the ASCE 07-10 provisions to establish the geometric and design details.

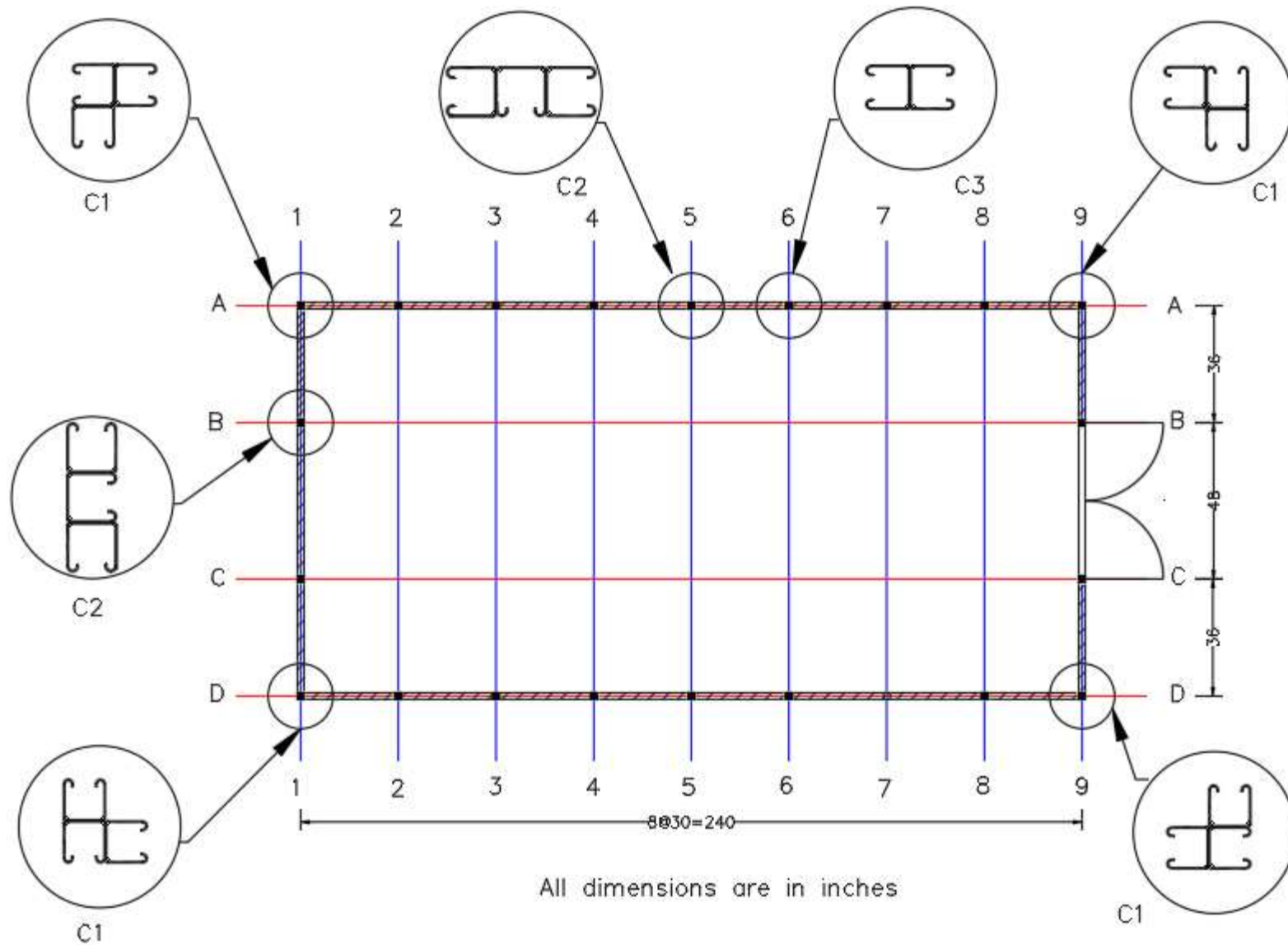


Figure 4-1. Layout of the building and typical column geometry

The perimeter frames A-A and D-D are similar and labeled as PF1 and PF2. The perimeter frame 9-9 includes a door and is labeled as PF3. The frame along 1-1 is labeled as PF4. Figure 4-2, Figure 4-3, and Figure 4-4 show the elevation view of PF1 (or PF2), PF3, and PF4, respectively. Steel channel sections with different cross-section geometries are selected for columns, horizontal bracing, beams, and cross ties. These channel sections provide flexibility during assembly, dismantling, and transportation. Further, internal partitioning of the building with plywood boards is possible with these channel sections.

Three column sections are used: C1 – corner columns, C2 - interior columns supporting roof trusses, and C3 - the remaining interior columns. The column locations are shown in Figure 4-1. All the column sections are pre-galvanized (PG). Column cross-section dimensions are shown in Figure 4-5.

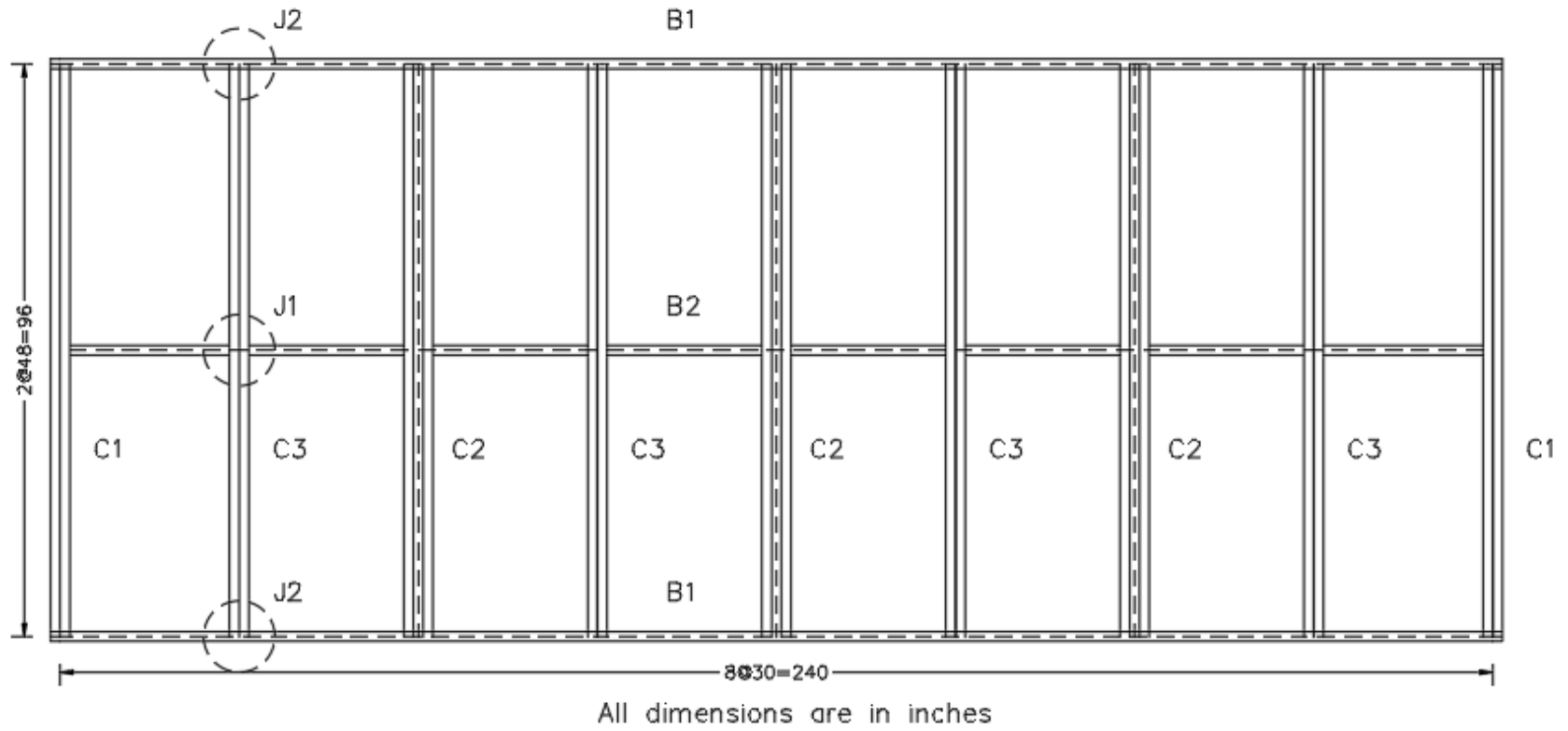
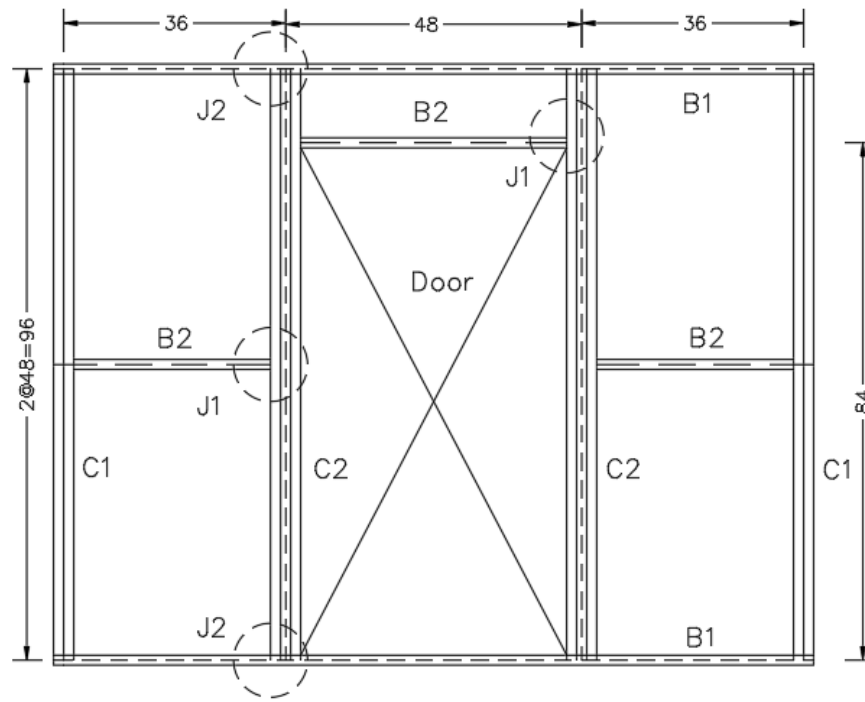
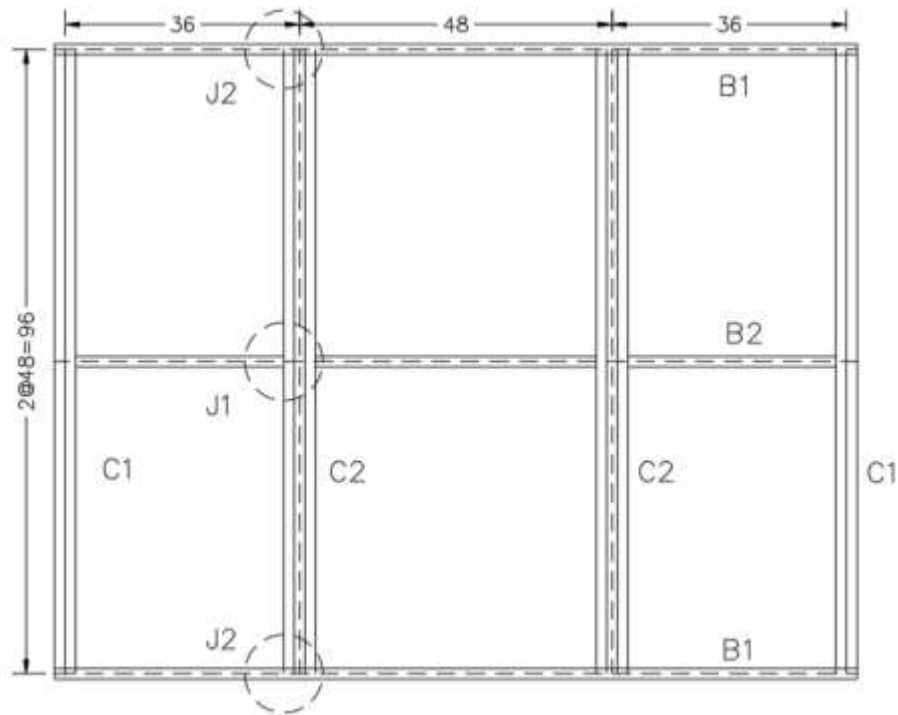


Figure 4-2. Elevation view of PF1 and PF2



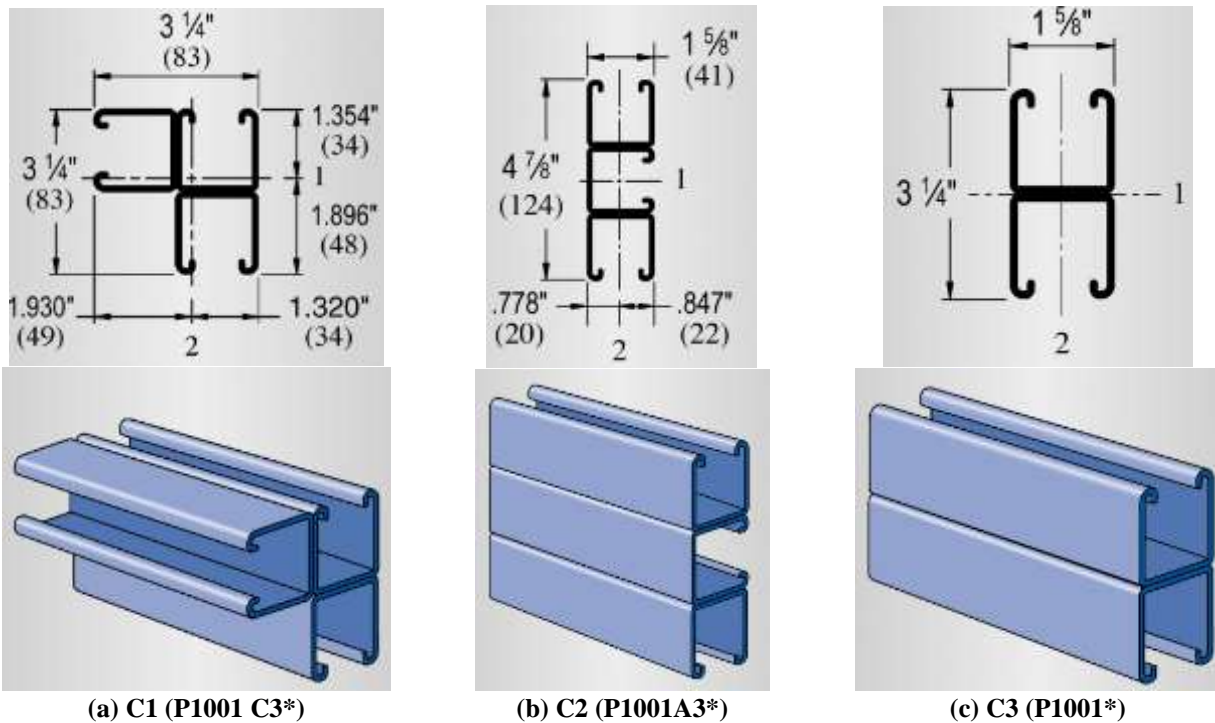
All dimensions are in inches

Figure 4-3. Elevation view of PF3



All dimensions are in inches

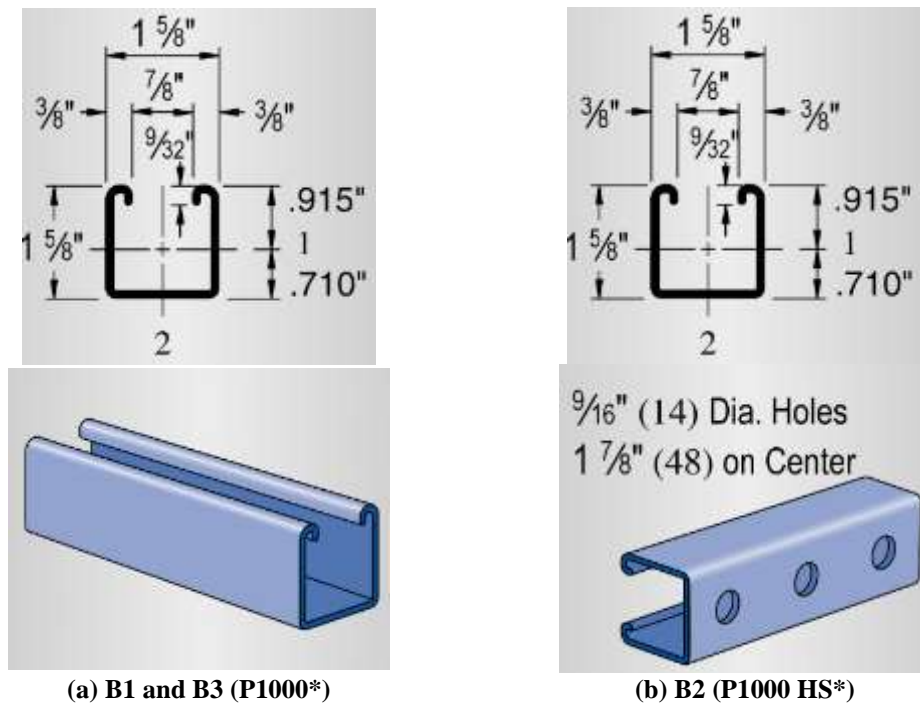
Figure 4-4. Elevation view of PF4



*The section designation given by UNISTRUT (the manufacturer).

Figure 4-5. Building column sections (Unistrut 2017)

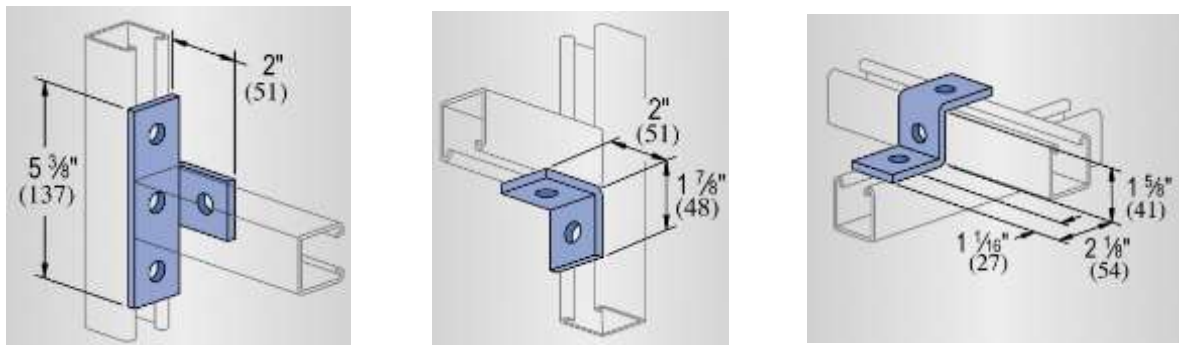
As shown in Figure 4-2, Figure 4-3, and Figure 4-4, channels are used as beams at the top and bottom of the four perimeter frames. These members are labeled as B1. In addition, channels are used as horizontal bracings (B2) in all four frames. The channels are also used in the transverse direction to provide the required lateral stability by connecting C3 columns at the roof level. These transverse members are labeled as cross ties (B3). All the channel sections are pre-galvanized (PG). Figure 4-6 shows the dimensions of the channel sections used for B1, B2, and B3.



*The section designation given by UNISTRUT (the manufacturer).

Figure 4-6. Details of the beams, bracings and cross ties (Unistrut 2017)

J1, J2 and J3 are the three connection details noted in Figure 4-2, Figure 4-3, and Figure 4-4. The fittings needed for these connections are shown in Figure 4-7. The 90° fitting (J1) is selected for the connection between the column and horizontal bracing. The 90° fitting (J2) is selected for the column to beam and beam to cross tie connections. The “Z” shape fitting is selected for the connection between the flat roof truss and the top beam. All the fittings are electrogalvanized (EG).



(a) J1 (P1033 4-hole 90° fitting*) (b) J2 (P1026 2-hole 90° fitting*) (c) J3 (P1045 3-hole Z shape fitting*)

*The section designation given by the UNISTRUT (the manufacturer).

Figure 4-7. Fitting details (Unistrut 2017)

The fittings are connected to the channels using hex-head bolts and nuts. As shown in Figure 4-8, the nuts are supported by a spring to retain them in place until the bolts are tightened (Unistrut 2017).

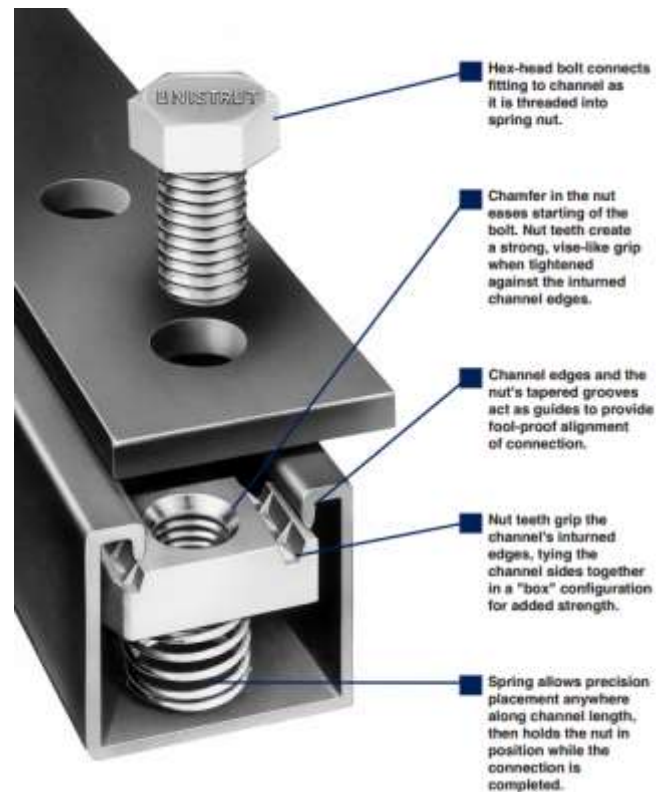


Figure 4-8. Connection detail showing a nut and a spring supported nut (Unistrut 2017)

As shown in Figure 4-3, this single-story building has only one door. However, windows can be placed at any location as desired to simulate various enclosed or opening structural conditions. A partition wall can be connected to column C2 since it has a channel in the middle oriented towards the interior of the structure. Hence, partitioning is possible along the longitudinal as well as the transverse directions. Figure 4-9 illustrates the possible locations for internal partitioning. A pressure measurement system and the DAS can be placed inside the structure. Depending on the location of the building, alternatives for recording reference atmospheric pressure need to be evaluated.

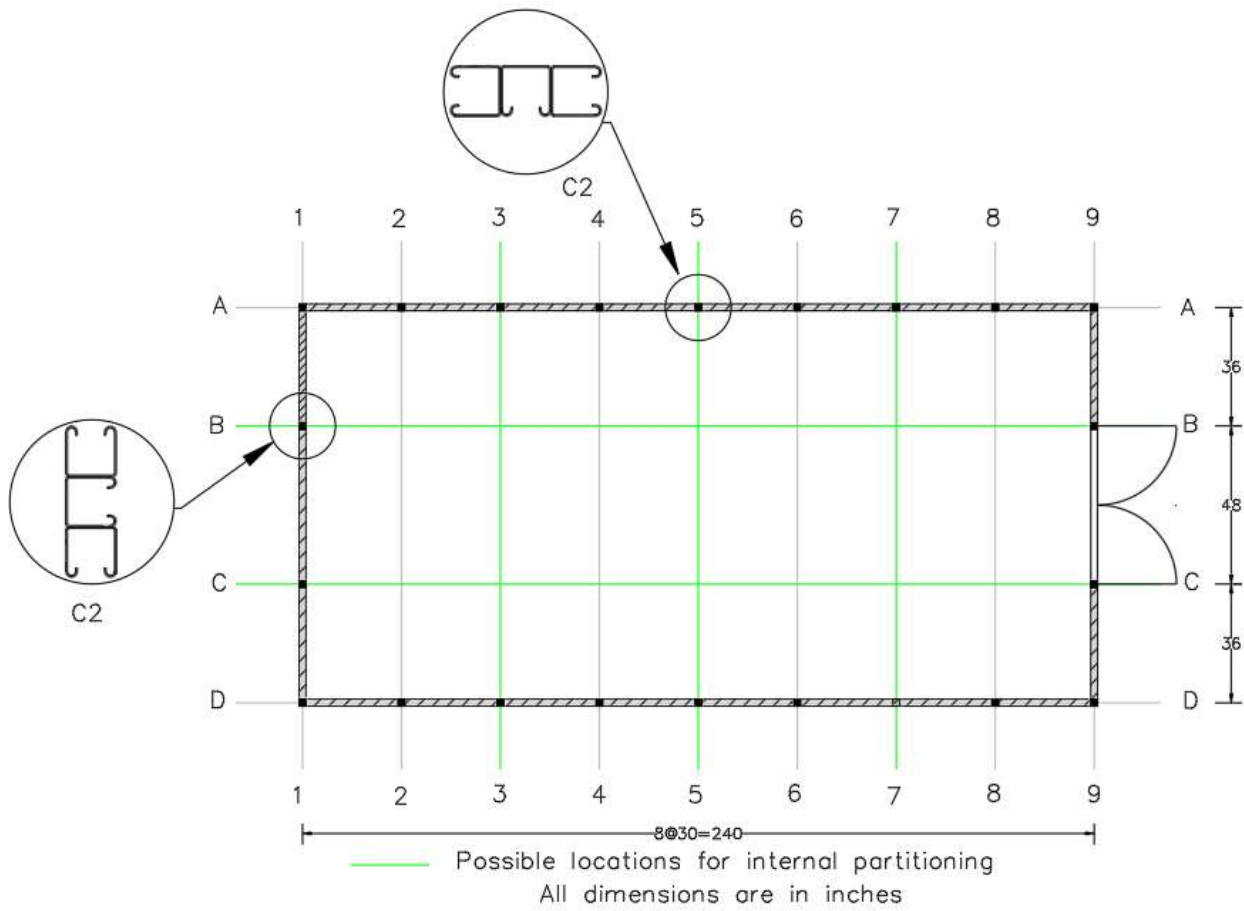


Figure 4-9. Locations provided for internal partitioning

4.2.1.2 Cost Estimate for the Base Structure

Table 4-1 shows the initial cost estimate for the proposed structure. This cost estimate has been prepared based on the quotation provided by a distributor of the UNISTRUT products (Graybar). Appendix E has the original quotation.

Table 4-1. Cost Estimate for the Structure

Item*	Description	Qty	Unit Price (\$)	Total Price (\$)
P1001 A3 -10 PG	For column C2 (Interior columns supporting roof truss)-10ft (100 in a standard package)	10	-	1625.28
P1001 C3 -10 PG	For column C1 (Corner columns supporting roof truss)-10ft (80 in a standard package)	4	-	2398.89
P1001 - 10 PG	For column C3 (Interior columns)-10ft (100 in a standard package)	10	-	863.45
P1000 - 10 PG	For transverse members adjoining walls (cross ties) (110 in a standard package)	19	-	145.53
P1000HS - 10PG	For horizontal bracing - 10ft (20 in a standard package)	6	-	91.88
P1033-4 Hole, 90° fitting - EG	Connection at horizontal bracing to column	44	-	240.25
P1026-2 hole, 90° fitting - EG	Connection at bottom beam to cross ties	84	-	74.09
P1045-3 hole, "z" shape fitting - EG	Connection at top beam to lateral P1000HS and trusses	8	-	21.34
P1008- EG 3/8"-16	Channel nut springs for P1033 4-hole fittings, P1026 2-hole fittings (top) and P1045 3-hole fittings	282	-	111.84
P1010-EG 1/2"-13	Channel nuts with spring for P1026 2-hole fittings (base)	98	-	43.54
HHCS037150 -EG 3/8"	1 1/2" long hex head screw for P1033 4-hole fittings, P1026 2-hole fittings (top) and P1045 3-hole fittings	282	-	120.36
HHCS050150-EG 1/2"	1 1/2" long hex head screw for P1026 2-hole fittings	98	-	72.21
P1769 - HG	8 1/2" bracket for roof truss support (20 in a standard package)	10	-	516.86
*Item code used by the UNISTRUT.				
<ul style="list-style-type: none"> • The cost of shipping, handling and taxes is not included in the cost estimate. • The labor cost for installation and fabrication of the structure is not included in the cost estimate. 				

4.2.1.3 Roof

Two different roof systems with roof pitches of 0 and 8/12 ($\approx 33^\circ$), representing a flat roof and a steep sloped roof, are selected for the structure. Five roof trusses are selected to support the roof. The trusses are mounted along 1-1, 3-3, 5-5, 7-7, and 9-9 lines shown in Figure 4-1. Hurricane ties shown in Figure 4-10 can be used to attach the roof trusses to the base structure to ensure adequate uplift resistance against wind. Timber purlins (2×4 in.) are installed along the longitudinal directions at a spacing of 30 in. to provide lateral stability to the trusses.

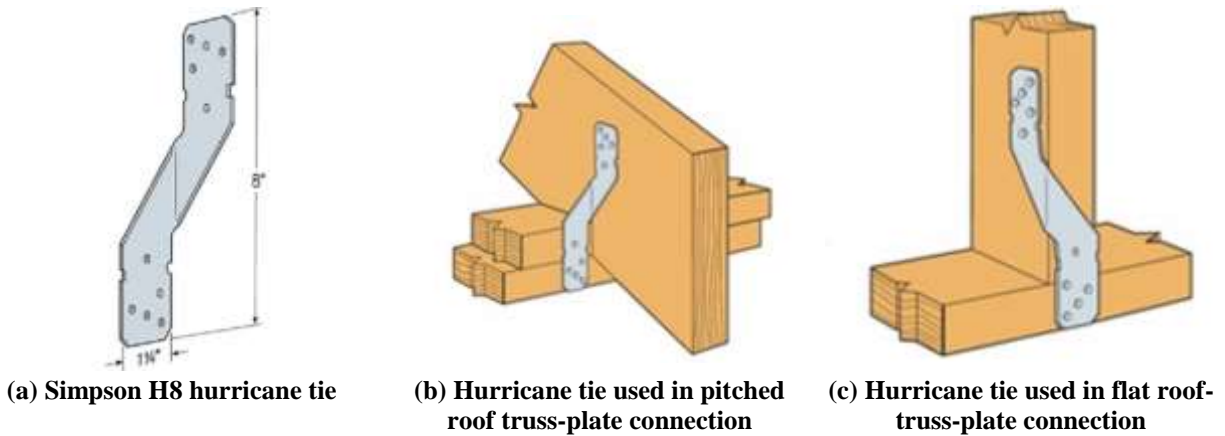


Figure 4-10. Hurricane ties used at the truss-wall connection (Fasteners Plus 2018)

4.2.1.3.1 Flat Roof System

The flat roof system consists of a 22-gauge steel corrugated deck, a 2 in. thick polystyrene foam board insulation, and a 45 mil (~1.14mm) black Ethylene Propylene Diene Monomer (EPDM) roofing membrane. All the components of the flat roof system are mechanically attached to the steel deck. The EPDM membrane is attached to the substrate using the fastener and plate attachment system. Open web roof trusses, as shown in Figure 4-11, support the flat roof system. The top and bottom chords of the truss are made of 2×4 fir timber, and the vertical members connecting the top and bottom chords are steel tubes with a 1 in. an outer diameter. The steel tubes are connected to the timber chords using screws. An aluminum drip edge flashing is installed around the perimeter of the flat roof.

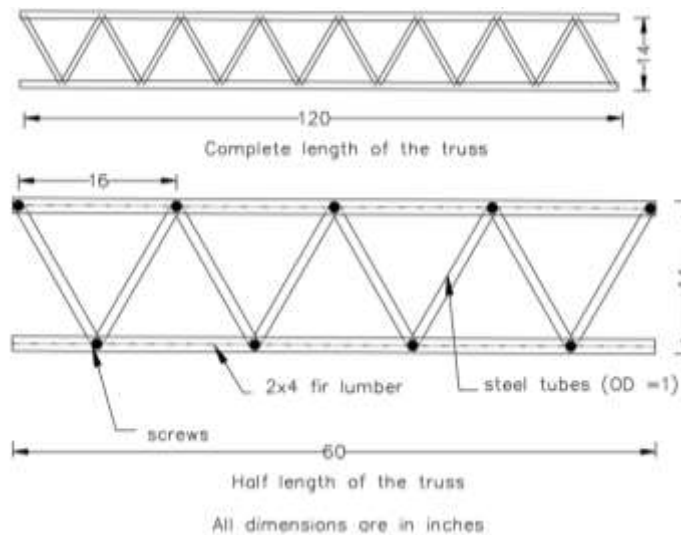


Figure 4-11. Open web roof truss for the flat roof

4.2.1.3.2 Steep Sloped Roof System

The steep sloped roof system (roof pitch = 8/12) consists of oriented strand boards (OSB), rigid foam insulation, underlayment, and a rib metal panel. The roofing components are attached to the roof truss using fasteners. Howe type pitched roof trusses, as shown in Figure 4-12, support the steep sloped roof system.

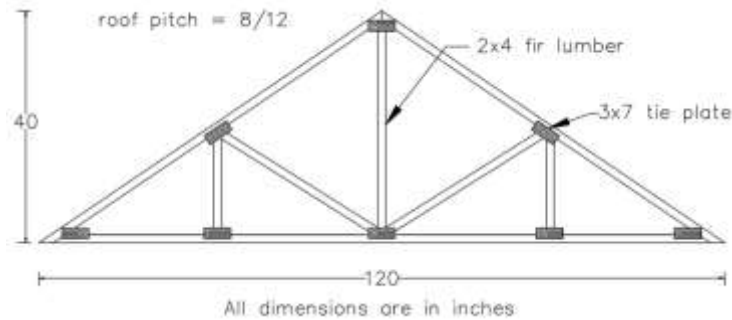


Figure 4-12. Howe type pitched roof truss to support steep sloped roof

The pitched roof truss is supported on a bracket mounted on the C1 and C2 columns. The bracket shown in Figure 4-13 is proposed as the suitable type for this purpose. The bracket is hot dip galvanized (HG).

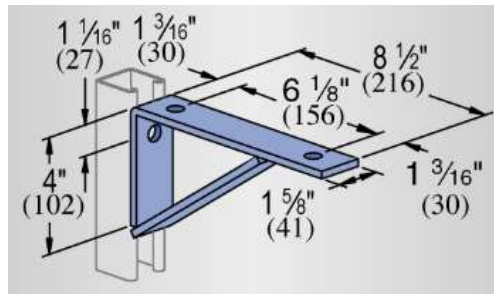


Figure 4-13. Bracket support for the pitched roof truss (P1769) (Unistrut 2017)

4.2.1.4 Cost Estimate for the Roofs

Table 4-2 shows the initial cost estimate for two types of roofing systems. The cost estimate is divided into three sections: flat roof, pitched roof, and the common items. The cost of the majority of items in this estimate has been acquired from the prices listed by the respective manufacturers/distributors. Please note that the cost estimate does not include the shipping cost, handling cost for the items nor the labor cost involved in the installation. The cost of fittings used for the connection between the roof and the structure is included in the cost estimate provided for the structure.

Table 4-2. Cost Estimate for the Flat Roof and Steep Sloped Roof Systems

Item*	Description	Qty	Unit Price (\$)	Total Price (\$)
Flat Roof				
WF204TOPCHC10	Top Choice 2×4×10-ft fir lumber for top and bottom chords	10	4.49	44.90
7335	Alloy steel round tube (1 in. OD and 0.902 in. ID) 4130-normalized seamless	6	16.68	100.08
520684	#10 x 1 1/2" Self-drilling screws / six-lobe (torx) / wafer head / 18-8 stainless steel (500 count per carton)	1	118.91	118.91
WF204TOPCHC10	Top Choice 2×4×10-ft fir lumber for purlins	6	4.49	26.94
P3606-22G12	P303 Series, gauge 22, all galvanized corrugated steel roof deck	7	100.00	700.00
C10	#5 Tek fasteners for metal deck (100 in package)	1	38.00	38.00
90001019	2-in x 4-ft x 8-ft Insulfoam, R7.7 faced polystyrene foam board insulation	7	29.48	206.36
IF3P	Carlisle insulation fastening plates (1000 count pail)	1	100.00	100.00
IF214	Carlisle insulfast 2 1/4-inch insulation fastener (1000 count)	1	84.00	84.00
EPDM-301797-1	Black EPDM rubber roofing membrane, 45 mil, 10 ft. wide (per foot)	20	9.45	189.00
HPX5	Carlisle HP-X 5 in. fasteners (500 Count)	1	105.50	105.50
HPXPP	Carlisle piranha fastening plates (1000 Count)	1	187.00	187.00
CAD12-WH	Gibraltar building products 12 ft. aluminum birch white drip edge flashing	6	5.96	35.76
Pitched Roof				
WF204TOPCHC10	Top Choice 2×4×10-ft fir lumber for truss chords	91	4.49	408.89
WF204TOPCHC10	Top Choice 2×4×10-ft fir lumber for purlins	6	4.49	26.94
HTP37Z	3 in. x 7 in. ZMAX galvanized heavy tie plate	40	2.11	84.40
SD9112R100	#9 x 1-1/2 in. External hex flange hex-head structural-connector screw for tie plates (100 count)	4	11.64	46.56
RT7A-TZ	USP 6-1/2-in 18-gauge triple zinc steel rafter tie	15	0.65	9.75
69138-8HGC1	Grip-Rite 2-1/2-in 10-gauge hot-dipped galvanized steel common nails for rafter ties (1-lb)	1	4.98	4.98
660663	4 ft. x 8 ft. Oriented strand board	7	8.65	60.55
973	1000 sq. ft. FeltBuster synthetic roofing underlayment roll	1	74.98	74.98
320817	1-1/2 in. x 4 ft. x 8 ft. R-5.78 Rigid foam insulation	7	14.15	99.05
2313417	3ftx 12 ft. Classic rib steel roof panel	7	39.84	278.88
8211217	1-1/2 in. Wood charcoal screw (250-bag)	1	37.90	37.90
6451799	Classic rib inside closure strip glued	15	1.98	29.70
4206017	Gable trim	4	22.56	90.24
4202317	14 in. Universal ridge flashing in charcoal	2	26.33	52.66
4204817	5 in. x 10.5 ft. Eave flashing molding in charcoal	4	14.04	56.16
Common Items				
H8	Simpson H8 hurricane tie - g90 galvanized	10	0.54	5.40
T410ARN1	4d (1-1/2") Simpson ring shank roofing nail - 316 stainless steel, 1 lb. pkg for h8 hurricane ties	1	14.19	14.19
*The item codes as indicated by the manufacturer/distributor.				

4.2.1.5 Building Anchoring System

The building can be anchored to the ground using penetrators/anchors. Figure 4-14 shows the locations of these anchors on a plan view of the building. The PE46 penetrator shown in Figure 4-15(a) was found to be adequate to resist the design loads of the structure. These penetrators have a pull-out load capacity specified by the manufacturer based on the substrate: soil or hard material (concrete, asphalt etc.). The penetrator acts both as an anchor for the uplift load and as a footing for the gravity loads (under the design wind and snow loads). These anchors are lightweight, reusable and are ideal for temporary structures (American Earth Anchors 2015). The anchors can be driven into the ground using impact wrenches, hydraulic installers, and power take-offs. Refer to Appendix D for the specifications and installation instructions of these penetrators.

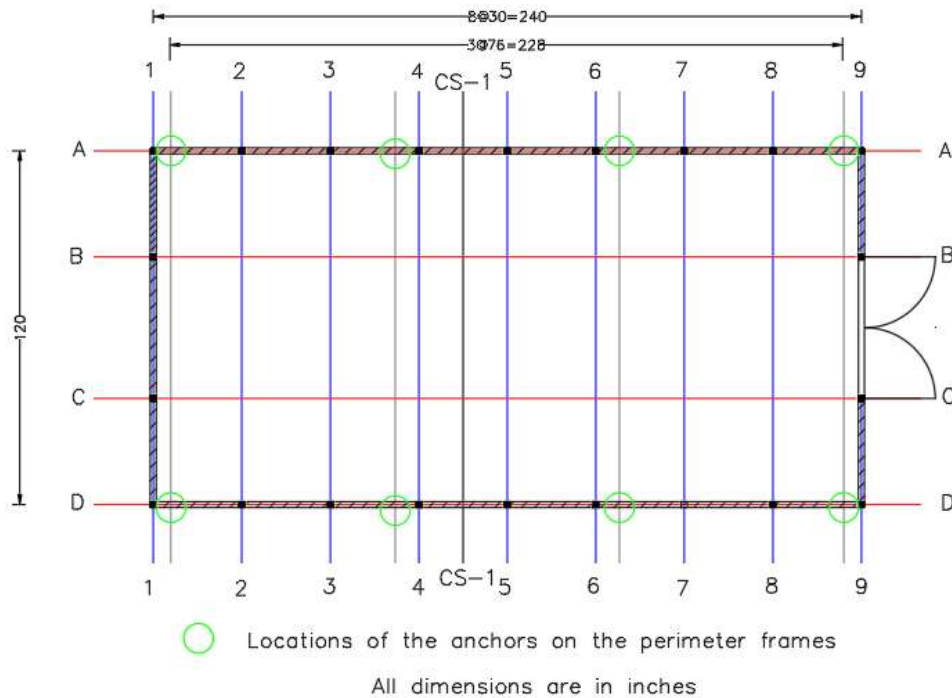


Figure 4-14. Plan view showing the location of the anchors on the perimeter frames

The complete building is erected on a 10 × 20 ft timber base frame constructed using 4 × 6 in. treated lumber. The structure is located 6 in. above the ground due to the presence of this base timber frame. The P1045-3-hole Z shape fittings shown in Figure 4-7(c) are used to attach the perimeter frame of the structure to the timber base frame (from the interior of the building). The timber base frame is provided to attach the ‘L’ bracket that would accommodate the penetrators. These ‘L’ brackets are specifically designed for PE 46 hex head penetrators. Eight

7-gauge steel ‘L’ brackets (at 90° angle), as shown in Figure 4-15(b), are attached to the timber frame. The locations at which the ‘L’ brackets are connected to the timber base frame are similar to locations of the anchors as shown in Figure 4-14. Anchors are driven through the horizontal arm of the ‘L’ bracket into the ground. Hex bolts are used to connect the vertical arm of the ‘L’ bracket to the timber frame. Figure 4-16 illustrates the details of the anchoring system through a cross section of the building (CS1-CS1 in Figure 4-14).

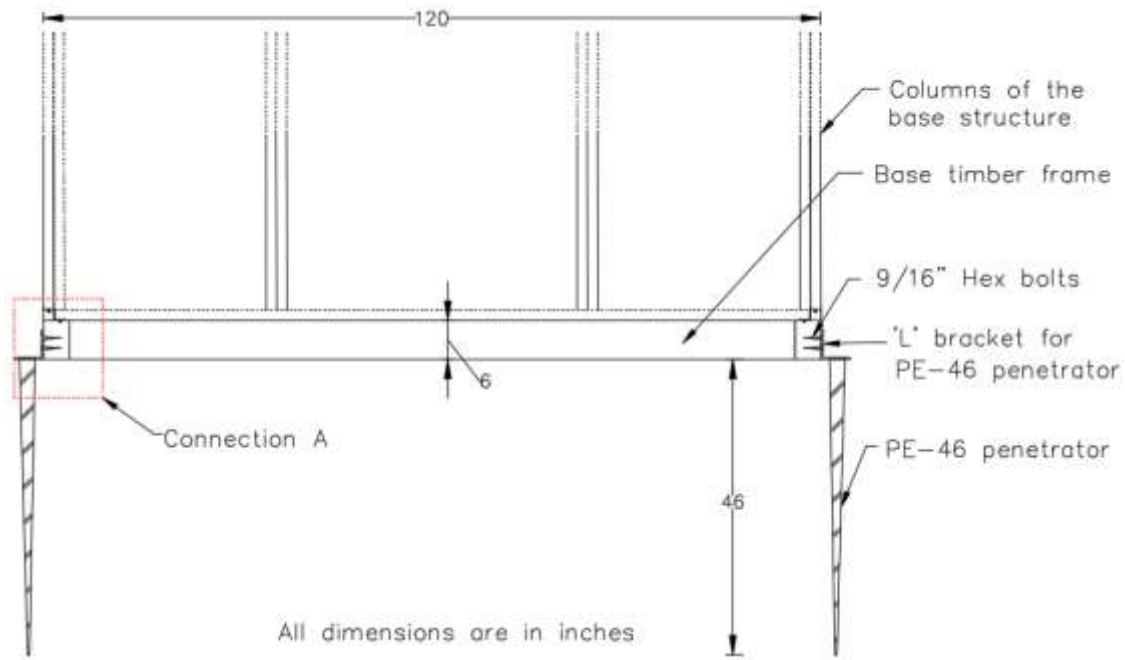


(a) PE46 Hex head penetrator
(American Earth Anchors 2019a)

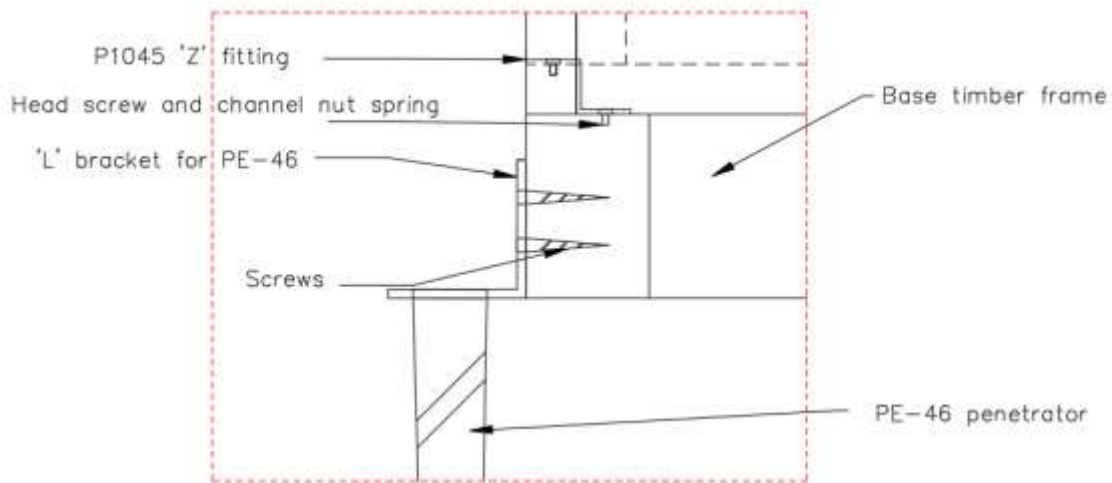


(b) L bracket for the penetrator
(American Earth Anchors 2019b)

Figure 4-15. Details of the anchoring system



(b) Section CS1-CS1



(b) Close-up view of connection A

Figure 4-16. Details of the anchoring system proposed for the building

4.2.1.6 Cost Estimate for the Anchoring System

Table 4-4 shows the initial cost estimate for the proposed anchoring system. Cost of the items in this estimate were acquired from the prices listed by the respective manufacturer for the listed items. The cost estimate does not include the shipping, handling, and installation costs.

Table 4-3. Cost Estimate for the Anchoring System

Item*	Description	Qty	Unit Price (\$)	Total Price (\$)
Penetrators				
PE46-L90	Penetrator 90° bracket for large penetrators	8	39.51	316.08
PE46-Hex	(PE46-Hex) 46-inch penetrator with 2-inch hex head	8	106.85	854.80
Timber base frame				
11503	Severe weather 4-in x 4-in x 10-ft; #2 treated lumber	6	11.37	68.22
20YR92	Wood screw, 6", T40 6 lobe flat head, PK12 for timber	2	24.98	49.96
Connections				
P1045-3 hole, "z" shape fitting - EG	Connection at top plate to lateral P1000HS and trusses	8	-	26.68
HHCS037150 -EG 3/8"	1 1/2" long hex head screw for P1045 3-hole fittings	10	0.43-	4.30
P1008- EG 3/8"-16	Channel nut springs for P1045 3-hole fittings	10	0.40	4.00
18181	Hex bolts, stainless steel 18-8, 9/16"-12 x 2" to connect L90 to timber frame	10	1.74	17.40
*The item code as indicated by manufacturers/distributors				

4.2.1.7 Flooring and Walls

A composite deck board, as shown in Figure 4-17(a), is selected for the floor. The composite deck board has the capacity to withstand the loads while acting as an insulation. The boards are lightweight and durable, hence easy handling and suitable for outdoor applications. The boards are laid over the cross ties and mechanically attached to the cross ties using wood screws.

Strand panel sidings, as shown in Figure 4-17(b), are selected as wall covering. These strand panels are treated engineered wood products recommended to be used in outdoor buildings in high wind areas. The boards are nailed onto the columns using spiral shank nails. One-and-a-half-inch thick foam board insulation panels are attached to walls to provide an air barrier with a vapor retarder.



(a) Composite deck board for flooring (Lowes 2019a)



(b) Panel siding for walls (HomeDepot 2019)

Figure 4-17. Floor and wall coverings

4.2.1.8 Cost Estimate for the Flooring and Walls

Table 4-4 shows the initial cost estimate for the flooring and wall material. The cost of the items was acquired from the prices listed by the respective manufacturers/distributors. The cost estimate does not include the shipping, handling, and installation costs.

Table 4-4. Cost Estimate for the Flooring and Wall Materials

Item*	Description	Qty	Unit Price (\$)	Total Price (\$)
Flooring				
SD010612E2G01	Trex enhance basics 12-ft saddle grooved composite deck board for flooring	4	21.00	84.00
9035679	#10 x 1-1/2 in. Phillips drive wood screws flat head zinc plated steel (100-Pack)	1	37.39	37.39
Walls				
27874	SmartSide 48 in. x 96 in. strand panel siding	15	36.17	542.55
8HGSTPD1	#11 x 2-1/2 in. 8-Penny hot-galvanized spiral-shank deck nails (1 lb.-pack-106 in a pack)	4	6.25	25.00
320817	1-1/2 in. x 4 ft. x 8 ft. R-5.78 Rigid foam insulation	15	14.15	212.25
42821025	MemBrain 9 ft. x 100 ft. air barrier with smart vapor retarder	1	149.09	149.09
320817	1-1/2 in. x 4 ft. x 8 ft. R-5.78 Rigid foam insulation	15	14.15	212.25
*The item code as indicated by the manufacturers/distributors				

4.2.2 Meteorological System

The meteorological system consists of a self-supporting, steel meteorological tower on which the wind measuring equipment is mounted. Although the system is termed as a meteorological system, the system proposed in this study only measures the wind parameters. However, mounting sensors and equipment for measuring other meteorological parameters such as humidity, temperature, solar radiation, etc., is possible. The following sections discuss the details of the tower and the measuring equipment.

4.2.2.1 Meteorological Tower

A self-supporting steel meteorological tower is selected. Based on the ASCE 07-10, a design wind speed of 110 mph was selected. For this design wind speed, the Amerite-55 (AME-55) tower manufactured by the American Tower Company is adequate. This tower includes three sections: a short base to be embedded into a concrete foundation, straight sections to build the tower height, and a top section to support the mast and antenna. The proposed tower is 45 ft tall, with a 5 ft base section and four 10 ft mid sections. Figure 4-18(a), (b), and (c) show the complete tower, plan view of the tower and a typical section detail of the tower, respectively. Appendix D provides the

details of the tower. The foundation of the tower could be a deep concrete foundation or a mat foundation depending on the design loads. The tower is anchored to a concrete foundation through a base plate specifically designed for AME-55, as shown in Figure 4-18(d). J bolt style base bolts are used to connect the base plate to the concrete foundation. Joint bolts are used to connect the five tower sections (1 base section and 4 mid sections) to each other and the base section to the base plate. The details of the suggested concrete foundation for the tower, base plate and the bolt details are given in Appendix D. However, an alternative foundation detail with ground anchors that are used for the building can be developed if the building is not located at a specific site for a considerable time. Mounts or booms can be installed at desired locations on the tower to mount the wind measuring equipment.

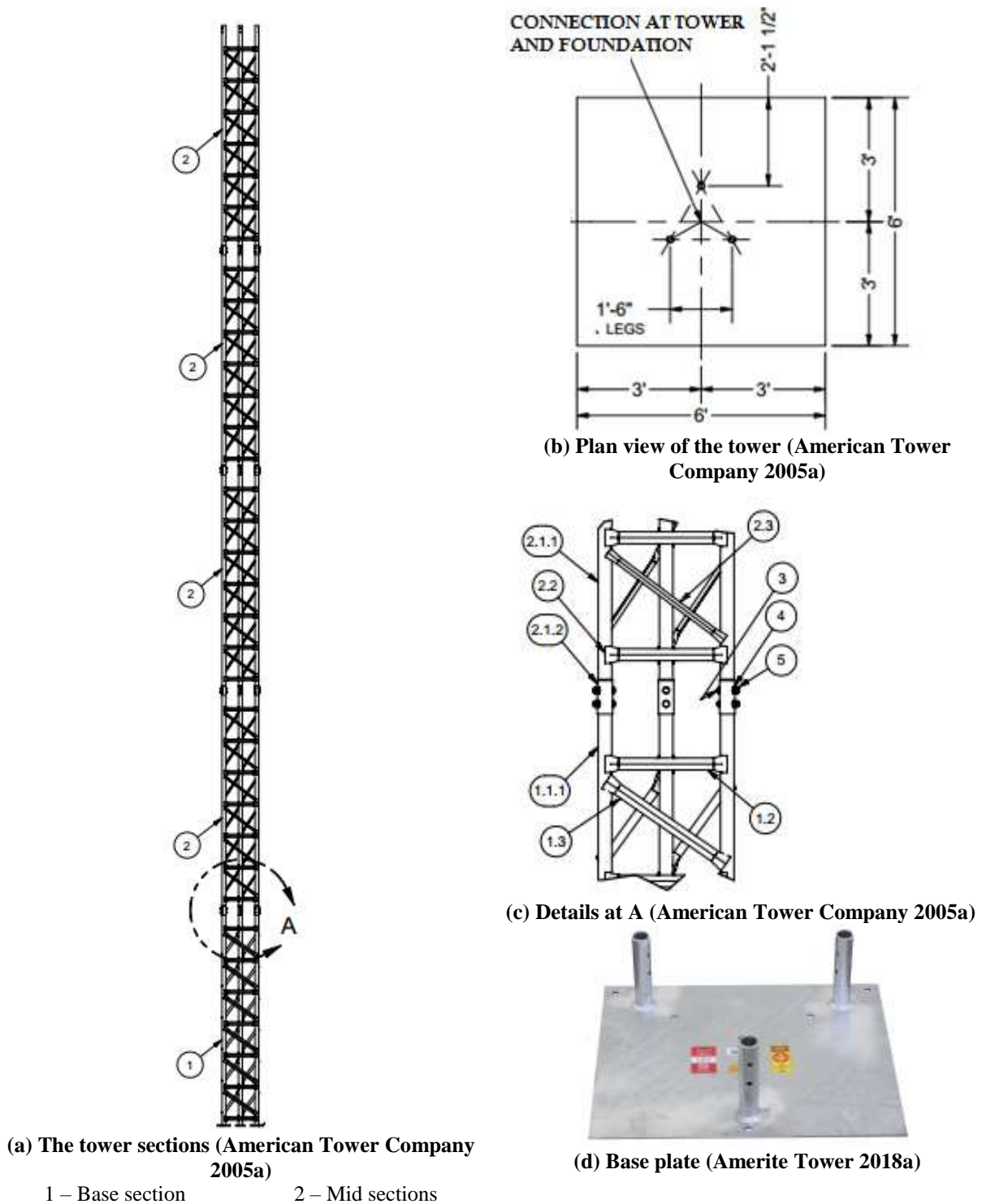


Figure 4-18. Components of the AME-55 tower

4.2.2.2 Wind Measuring Equipment

The 3-axis ultrasonic anemometers are selected to measure wind velocity in all three directions and the magnitude. The time variation of velocity can be used to derive the turbulence variation in the wind. An optimum number of anemometers needs to be installed at various heights along the tower to capture the complete approaching wind profile. Appendix D provides the specifications of the anemometer.

4.2.2.3 Cost Estimate for the Meteorological System

The cost estimate does not include the foundation. Appendix E includes the cost estimate provided by the American Tower Company for the AME-55 tower. The unit cost of an anemometer manufactured by the RM Young is provided in the cost estimate. Upon deciding on the optimum number of instruments to capture necessary data to develop the wind profile, the total cost estimate for the wind measurement system can be prepared. The cost estimate does not include the shipping, handling, and installation costs.

Table 4-5. Cost Estimate for the Meteorological System

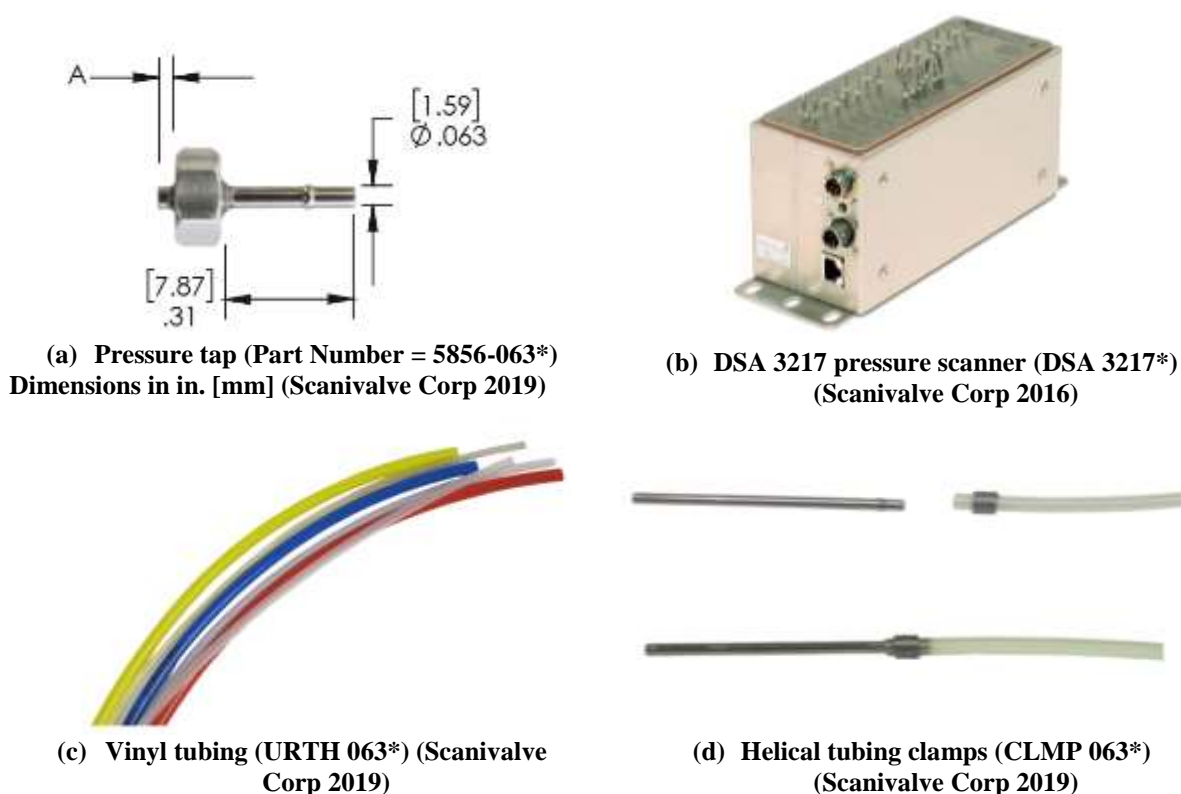
Item*	Description	Qty	Unit Price (\$)	Total Price (\$)
Meteorological Tower				
AME 55-B5	5' Ground base section	1	169.00	169.00
AME 55	10' Mid-section	4	342.38	1369.52
AME55-BGR	Amerite tower base plate	1	149.99	149.99
ROH-1-2X12BB	Tower base bolt, J bolt style, 1/2 in. diameter, 12 in. length	6	18.99	113.94
AME55BK	Amerite joint bolt kits	5	14.99	74.95
Wind Measurement System**				
81000	RM Young model 81000-3-axis ultrasonic anemometer	1	2892.00	2892.00
Cable	Cable for model 81000	200	1.90	380.00
*The item code as indicated by the AMERICAN TOWER COMPANY for the tower components and the RM YOUNG for the ultrasonic anemometer and its accessories				
**Price of one anemometer is given leaving an opportunity to customize the systems as needed.				

4.2.3 Structural Response Measurement System

Wind pressure distribution, displacement, and forces are typically monitored to understand the structural response. The following sections present the details of selected instruments/sensors and accessories of a structural response measurement system as well as the cost estimates.

4.2.3.1 Pressure Measurement System

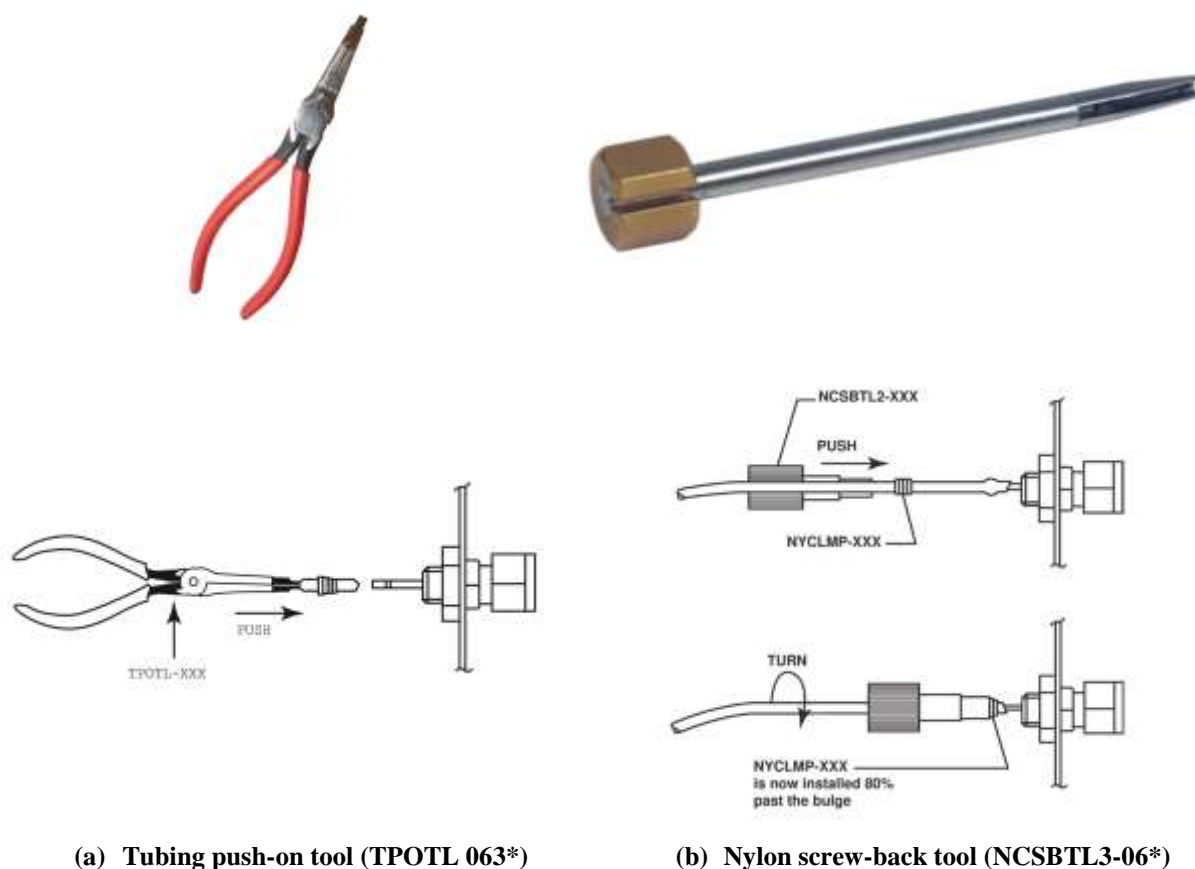
A pressure measurement system manufactured by the Scanivalve is selected for this structure. Pressure taps are to be installed over the roof surface to capture pressure distribution. Figure 4-19(a) shows a pressure tap. A hole is drilled through the test object, and the pressure tap is attached using adhesive. The through-hole design of the tap (Dimension A in Figure 4-19(a)) allows a flush finish on the exterior surface of the roof (Scanivalve Corp 2019). A pressure scanner is used to collect pressure data from pressure taps. A DSA 3217 pressure scanner shown in Figure 4-19(b), with a full-scale pressure range of ± 1.0 psi and with 16 ports, is selected as a suitable scanner. The pressure taps readings and atmospheric pressure readings (reference pressure) are provided as input to the scanner, which calculates the differential pressure and provides as an output (Scanivalve Corp 2016). Flexible tubing shown in Figure 4-19(c) connects pressure tap tubulations and the scanner. Clear urethane tubing (which is extremely flexible, resilient, and resistant to kinking) are selected. Brass helical tubing clamps shown in Figure 4-19(d) are used to clamp plastic tubing onto the tubulations extending from the pressure scanner and from the pressure taps. These clamps conform to the outside diameter of the tubulations in the pressure tap and the scanner such that the clamps easily fit over the urethane tubing on the tubulation (Scanivalve Corp 2019). Appendix D provides specifications of these components.



*Item code defined by the SCANIVALVE (the manufacturer).

Figure 4-19. Pressure measurement system components

Several other accessories are required for pressure measurement system installation. The tubing push-on tool and the nylon screw-back tool (shown in Figure 4-20(a) and (b), respectively) are examples for such accessories. The tubing push-on tool is used to grasp the urethane tubing and push it onto the pressure tap tubulations. The screw-back tool is used to manually install helical clamps over the bulge of the tubulation (Scanivalve Corp 2019). Appendix D provides specifications of these accessories.



(a) Tubing push-on tool (TPOTL 063*)

(b) Nylon screw-back tool (NCSBTL3-06*)

*The item code defined by the SCANIVALVE (the manufacturer).

Figure 4-20. Pressure measurement system installation accessories (Scanivalve Corp 2019)

4.2.3.2 Cost Estimate for the Pressure Measurement System

Total number and density of pressure taps on the roof depend on the possible wind pressure distribution on the roof. The possible wind pressure distribution can be obtained through numerical simulations under predicted wind loads (outside the scope of this study). Therefore, the cost of one pressure scanner is given in Table 4-6. Upon finalizing the distribution of pressure taps on the roof, the total cost for a complete pressure measurement system can be calculated. The cost estimate does not include the shipping, handling, and installation costs.

Table 4-6. Cost Estimate for a Pressure Measurement System

Item*	Description	Qty	Unit Price (\$)	Total Price (\$)
DSA3217	± 1.0 psi Full scale range DSA3218 pressure scanner	1	6,636.00	6,636.00
URTH-064	URTH-064 pressure tubing	150	0.44	66.00
5856.063	5856 Pressure tap with a .063 stickout	16	3.32	53.12
CLMP-063	Helical tubing clamps	16	0.32	5.12
Accessories				
TPOTL-063	Tubing push-on tool	1	92.00	92.00
NCSBTL3-063	NYCLMP Screw-back tool	1	80.00	80.00
*The item code as indicated by the SCANIVALVE				

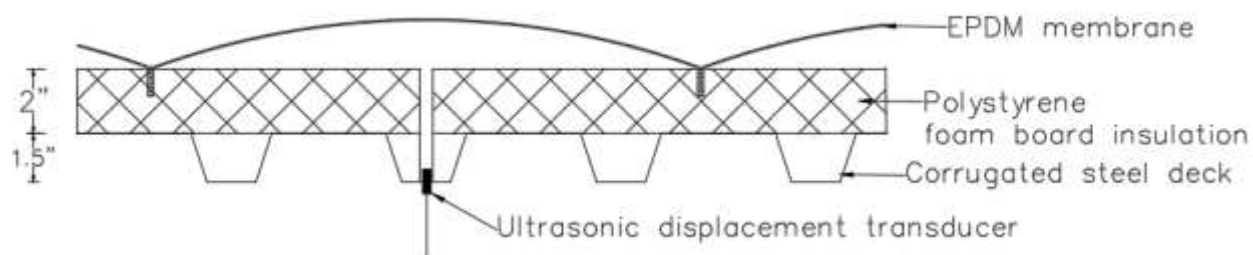
4.2.3.3 Displacement and Force Measurement System

Ultrasonic displacement sensors are selected to measure flat roof membrane deflection. Compared to other available displacement sensors, measurement ranges of ultrasonic sensors are within the required measurement limits. Although inductive sensors satisfy the required measurement ranges, inductive sensors require the targeted surface to be conductive, which is not possible with all the membrane types. An ultrasonic displacement sensor RPS-100-14, with a measurement range of 2 to 14 inches, is selected. Figure 4-21(a) shows the RPS-100-14 displacement sensor developed by the Migatron. Ultrasonic sensors are installed in between fastener lines used to attach the flat roof membrane. In flat roof systems, this location is expected to produce the maximum deflection due to billowing under wind loads. Holes need to be drilled through the roofing system into the steel deck to accommodate the sensors. The displacement will be measured relative to the steel deck through these holes. Figure 4-21(b) illustrates the location of the displacement sensor within a flat roof system. In order to identify the exact number of displacement sensors required to collect the necessary data, numerical simulations can be performed under simulated wind conditions to locate the critical displacement locations on a roof. In the case of a steep sloped roof system, significant deflections are not expected in roof covering due to high stiffness of the roofing system. However, displacement transducers can be used measure structural system response of any of these roofing systems.



(a) Ultrasonic displacement sensor (RPS-100-14*) (Migatron Corporation 2001)

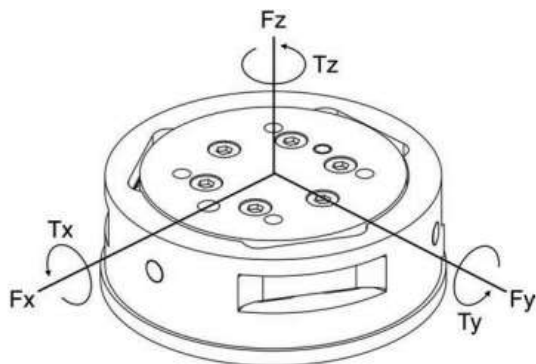
* Item code defined by the MIGATTRON.



(b) Location of ultrasonic displacement sensor in a flat roof system

Figure 4-21. Ultrasonic displacement sensor and its location in a flat roof system

In order to monitor the force in the fasteners under the prevailing wind conditions, six-component force transducers are proposed to be installed at the fastener locations on both flat and steep sloped roofs. A six-component force transducer simultaneously measures forces in three orthogonal directions and moments about these three axes, as shown in Figure 4-22(a). The nano25 IPS65 Force/Torque (F/T) sensor shown in Figure 4-22(b) is selected as a suitable force sensor. Appendix D provides complete specifications of this device. Further analysis using numerical simulation tools under predicted wind conditions is required to identify the total number of sensors or the installation locations of force sensors on the roof (out of the scope of this study).



(a) Applied forces and torques on the transducer (ATI Industrial automation 2019b)



(b) Nano25 IP65/68 F/T sensor* (ATI Industrial Automation 2019a)

*Item code defined by the ATI INDUSTRIAL AUTOMATION.

Figure 4-22. Force/torque (F/T) sensor

4.2.3.4 Cost Estimate of the Displacement and Force Measurement System

Total number and the layout of sensors need to be defined after evaluating the structural and component response under expected wind condition (outside the scope of this study). Therefore, the cost of one ultrasonic displacement sensor and one force/torque (F/T) sensor is provided in Table 4-7. Upon finalizing the total number of ultrasonic sensors and F/T sensors, the total cost for the displacement and force measurement system can be calculated. Appendix E includes the cost estimate provided by the ATI Industrial Automation for the ATI transducers and accessories. The cost estimate does not include the shipping, handling, and installation costs.

Table 4-7. Cost Estimate for the Displacement and Force Measurement System

Item*	Description	Qty	Unit Price (\$)	Total Price (\$)
RPS-100-14	Ultrasonic sensor in a plastic housing with a range of 2-14 in.	1	668.00	668.00
9105-TW-NANO25-E-1.8	Nano25-E transducer with strain relieved cable, 1.8 m	1	4250.00	4250.00
9105-IFPS-1	Interface board and power supply for (1) F/T transducer	1	1700.00	1700.00
9105-C-PS-U-2	Cable from power supply or interface power supply box to DAQ card, unterminated, 2 m length	1	185.00	185.00
9105-M1USB6210	Bus-powered M-series multifunction DAQ, 16-bit, 250 kS/s. screw terminals. NI 779675-01	1	844.00	844.00

*Item code defined by the MIGATRON and the ATI INDUSTRIAL AUTOMATION

4.2.4 Data Acquisition System (DAS)

Three main components (sensors, data acquisition measurement hardware, and a computer) are required for a complete DAS. The sensors required for data collection are already discussed in

this report. After reviewing data acquisition systems used in similar full-scale experimental studies and the available product data sheets, several candidate systems are identified. However, only one system is presented in the next section.

4.2.4.1 DAS

The PXIe-1065, a data acquisition system (shown in Figure 4-23) with 18 slots as designed by the National Instruments, is selected as a suitable data acquisition hardware system. Appendix D includes PXIe-1065 specifications. A Dell, 9th Generation, Intel Core i5, desktop computer is adequate to process and output the measured data. The LabVIEW full development system is needed to develop a comprehensive data collection and processing system.



*The item code as indicated by the National Instruments.

Figure 4-23. PXIe-1065* (National Instruments 2019b)

4.2.4.2 Cost Estimate for the DAS

The cost estimate for the data acquisition system is shown in Table 4-8.

Table 4-8. Cost Estimate for the DAS

Item*	Description	Qty	Unit Price (\$)	Total Price (\$)
779730-01	Model: PXIe-1065	1	7325	7325.00
960680-100	Hardware service program	1	586.00	586.00
763000-01	Power cord, AC, U.S., 120 VAC, 2.3 m	1	10.00	10.00
776670-35WM	LabVIEW full development system	1	4487.32	4487.32
Dell 27 7000	Dell Inspiron 27 7000 all-in-one	1	799.99	799.99
*Item code defined by the NATIONAL INSTRUMENTS and DELL				

4.3 SUMMARY

The response of a structure under natural wind conditions is different than one under simulated wind conditions. A majority of the studies conducted in the past used wind tunnels to study the structural response under simulated wind conditions. Limited outdoor facilities are available to monitor real-time wind effect on building envelopes under natural wind conditions. The Texas Tech University (TTU) building is one such experimental structure that collects real-time wind-response data in the U.S. Such data is widely used for validation of wind tunnel and numerical simulation results. An experimental structure and necessary instrumentation and data acquisition

systems are developed and presented in this report. The system basically consists of four components: an experimental building, a meteorological measurement system, a response measurement system, and the data acquisition system. Cost estimates are prepared for each major component and summarized in Table 4-9. Since the process requires performing a comprehensive wind-structure interaction analysis before finalizing a sensor layout, unit prices are presented for the items indicated with a superscript (*) in Table 4-9. Shipping, handling, and installation costs are not included in the estimate.

Table 4-9. Cost Estimate for the Proposed Experimental System

Component of the Proposed Experimental Plan	Cost (\$)
Experimental building	14,728
Structure	6,326
Roofs	2,910
Building anchoring system	1,342
Flooring and walls	1,263
Meteorological system	
Meteorological tower	1,878
Wind measurement system*	3,272
Response measurement system	
Pressure measurement system*	7,107
Displacement and force measurement system*	7,647
Data acquisition system	8,721

5 SUMMARY, CONCLUSIONS, AND RECOMMENDATIONS

5.1 SUMMARY AND CONCLUSIONS

The edges and corners of flat and steep sloped roofs experience higher negative pressures (suction) compared to the roof interior. Separation bubbles created by the wind flowing perpendicular to the leading edge of a roof and the conical vortices created by the wind, flowing nearly oblique to the leading edge of a roof, are the two major flow phenomena behind this peak suction. The Federal Emergency Management Agency (FEMA) investigation reports, design codes such as ASCE 07, and published literature have highlighted the need of enhancing the resiliency of roofs. This can be accomplished by strengthening these high-pressure zones or altering wind patterns over the roof edges and corners to reduce suction by modifying roof edges or incorporating additional features and devices. Wind tunnel testing of scaled models, full-scale testing of prototype and real structures under simulated and natural wind conditions, and numerical simulations using computational fluid dynamic (CFD) techniques are used in predicting the wind loads on the roof. The sand erosion technique, digital imagery, laser sheets, smoke injection, etc., were used in experimental studies to visualize wind flow patterns. The following sections summarize the key findings from a comprehensive review of literature. In addition, recommendations for further research are presented based on the literature review and the limited CFD simulations performed during this study.

5.1.1 Roof Wind Pressure Distribution

Wind and building characteristics are the two major factors affecting wind pressure distribution on a roof. Table 5-1 summarizes research findings describing the impact of such parameters on roof wind pressure distribution and magnitude.

Table 5-1. Impact of Wind and Structure Characteristics on Wind Pressure Distribution and Magnitude over a Low-Rise Building Roof

Wind and building Characteristics		Research findings
Wind characteristics	Wind profile	The effect of a uniform flow on pressure distribution differs from that of a boundary layer flow (Cook 1985).
	Wind direction	Critical wind direction is 15° from windward roof corner (Özmen and Baydar 2016).
	Wind turbulence	Both longitudinal and lateral turbulences affect the pressure fluctuations (Wu et al. 2000). Smooth flow creates higher suction under conical vortices than turbulent flow (Kawai 1997).
Building characteristics	Building geometry	Area percentage under large suction at corners and edges increases with the decrease in plan dimensions (Gerhard and Kramer 1992). As an example, high pressure zone of a building with height/width (h/B) ratio of 0.4 extends from a corner up to 0.375B, whereas the high-pressure zone extends from a corner up to 0.065B when h/B = 0.04.
	Roof type	The uplift force on a flat roof is the highest compared to gable, hip, and pyramid roofs of comparable dimensions subjected to the same wind conditions. Pyramid roofs are subjected to the lowest uplift force while gable roofs are subjected to the second highest force (Keote et al. 2015, Meecham 1992, Xu and Reardon 1998, Prasad and Ahmed 2009, Özmen and Baydar 2016).
	Roof pitch	With the increase in roof pitch, the flow reattachment position moved towards the windward edge of the roof with no flow separation observed at 45° (Cook 1985). For a gable roof, with the increase in roof pitch, the peak suction at corners and edges disappear (Barnaud et al. 1974). The uplift force is the highest on a roof with a negative pitch. The second highest uplift force acts on a flat roof while a roof with a 45° pitch develops a compression (Cook 1985, Barnaud et al. 1974).
	Presence of aerodynamic features and edge modifications	Discussed in sec 5.1.2
	Building grouping	Presence of an upstream building amplifies the wind load on the flat roof of a downstream building. Wind load on the roof increases with the increase in relative height of the buildings (distance between the two buildings/height of the downstream building) (Pindado et al. 2011). Presence of a building group generally reduces roof suction, with a corner reduction of 50 – 65% (Surry and Lin 1995). A tandem arrangement produces the greatest wind interference effects on a building followed by staggered and parallel arrangements. The roof of the building located at the corner of a group experience the largest interference effects, irrespective of the group arrangement (Li et al. 2017).

However, only a few studies evaluated the impact of structural characteristics of a roofing system or its components on the uplift force magnitude and distribution on a roof. A full-scale experimental study conducted by Baskaran et al. (2012) demonstrated the impact of roofing

membrane stiffness on uplift pressure as well as on the membrane deformation. Sun et al. (2012) conducted a numerical simulation and demonstrated that the wind flow pattern around a roof is altered due to the flexibility of the roof itself. However, Sun et al. (2012) did not suggest any guidelines to identify the significance of this issue or strengthening mechanisms for the roof that they studied.

5.1.2 Wind Suction Mitigation Techniques for a Low-Rise Building

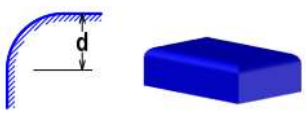

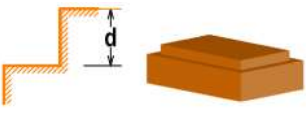
Roof edge modification and the use of aerodynamic features/devices are the two approaches considered and evaluated so far for reducing wind uplift pressure acting on roof edges and corners. The following sections summarize research findings on these two approaches.

5.1.2.1 Roof Edge Modification

The most popular edge modifications involve chamfering, rounding, and recessing roof edges. Table 5-2 summarizes the findings from the state-of-art and practice review. In general, the following observations are noted:

- The findings on rounded edges are inconclusive.
- Shallow chamfer angles reduce uplift force.
- The uplift force magnitude is inversely proportional to the depth of the recessed edge.

Table 5-2. Roof Edge Modification - A Summary of Findings

Edge modification	Geometry		Research finding	Comment(s)
	d*/h	Slope		
Rounded 	0.080	NA	Uplift force increased by 12.8% (Aly and Bresowar 2016).	Not recommended
	0.160		Uplift force increased by 9.0% (Aly and Bresowar 2016).	Not recommended
	0.240		Uplift force increased by 1.5% (Aly and Bresowar 2016).	Not recommended
	0.125		The height of separation bubble is inversely proportional to the radius of the rounded edge (Mahmood et al. 2008, 2011).	Rounded edges of these dimensions reduce negative pressure on the roof.
	0.250			
	0.125		The reduction in uplift force is 5%, 8%, and 11% at wind directions 0°, 30°, and 45°, respectively (Dong et al. 2019).	Rounded edges of these dimensions along the leading edge reduces the total uplift force on flat roofs, with the most effective reduction under skewed flows.
	0.175		The reduction in uplift force is 9%, 5%, and 11% at wind directions 0°, 30°, and 45°, respectively (Dong et al. 2019).	
Chamfered 	0.080	NA	Uplift force increased by 0.8% (Aly and Bresowar 2016).	Not recommended
	0.160		Uplift force decreased by 7.5% (Aly and Bresowar 2016).	Recommended
	0.240		Uplift force decreased by 12.0% (Aly and Bresowar 2016).	Recommended
	30°, 45° and 60°		Chamfer with 30° slope reduced the corner suction by up to 70% and overall roof load by 34% (Blackmore 1988).	Shallower chamfers produce largest load reductions. Steeper chamfers produce additional loads on windward edges.
Recessed 	0.080	NA	Uplift force decreased by 5.3% (Aly and Bresowar 2016).	Not recommended (Authors did not recommend this size, but the reasons are not clearly stipulated)
	0.160		Uplift force decreased by 8.3% (Aly and Bresowar 2016).	Recommended
	0.240		Uplift force decreased by 13.5% (Aly and Bresowar 2016).	Recommended

*For rounded edges $d = r$ (r is radius of the edge)

5.1.2.2 *Roof Aerodynamic Features/Devices*

Different types of aerodynamic features/devices are studied to identify alternatives to mitigate roof edge and corner damage. The objective of implementing such features and devices is to either disrupt the formation of the vortices or to disturb and displace the vortices formed at specific locations.

All these features/devices can be broadly categorized into three groups based on their geometry: parapets, spoilers, and special features/devices. Typically, parapets are vertical devices mounted along the edges. The spoilers are horizontal devices mounted on vertical supports erected along the edges. Parapets can be solid or porous. Both solid and porous parapets can be continuous (perimetric) or discontinuous. The continuous parapets run along the entire perimeter of the roof. Screens are a subset of porous parapets. Table 5-3 and Table 5-6 summarize the findings of the state-of-the-art review on parapets and spoilers installed on low-rise building roofs.

In addition to the parapets and spoilers, special features/devices such as porous canopy roofs, passive pressure equalization roofs, rotating cylinders (using the momentum injecting method), architectural elements, solar panels, and wind turbines have been proposed as aerodynamic damage mitigation devices. Trellis (pergolas), ridge extensions, and eave configurations with different designs are a few examples of architectural elements proposed for steep sloped roofs. These elements are generally installed flushed with the roof edge. In addition, gable end extensions are specifically proposed for gable roofs. Although the performance of some of these devices, such as porous canopy roofs and passive pressure equalization roofs, have been proven through scaled model testing, the design considerations and practical implementations are yet to be evaluated. The possibility of using solar panel arrays on both flat and gable roof buildings has been a focus in recent years due to their additional benefit of power generation required by the base building. Up to 75% and 30% suction reduction have been observed on flat roofs and gable roofs with solar panels, respectively (Iverson 2016, Aly and Bresowar 2016). However, several parameters (such as geometry of the roof, geometry and characteristics of solar panel arrays and wind characteristics) could influence the wind pressure loads on the roof as well as on the panels.

Table 5-3. Research Findings on Aerodynamic Devices - Parapets

Parapet type and reference	Geometry and details					Remarks	Research findings
	h_p/h [d*/h]	l_p/L	l_p/B	b_p/h	Porosity (%)		
Solid Parapets							
<i>Continuous (Perimetric)</i>							
Kopp et al. 2005a, 2005b	0.587	1	NA		0	Vertical	Reduced edge suction by about 20%.
Aly and Bresowar 2016	0.080	1	NA		0	Vertical	Total uplift force ¹ reduction is 19.4%
	0.160		NA	Total uplift force ¹ reduction is 19.3%.			
	0.240		NA	Total uplift force ¹ reduction is 7.9%.			
	0.080	1	NA		0	Slope-out	Total uplift force ¹ reduction is 12%.
	0.160		NA	Total uplift force ¹ reduction is 11%.			
	0.240		NA	Total uplift force ¹ reduction is 5%.			
	0.080	1	NA		0	Slope-in	Total uplift force ¹ reduction is 22%.
	0.160		NA	Total uplift force ¹ reduction is 22.2%.			
	0.240		NA	Total uplift force ¹ reduction is 10.5%.			
	0.080	1	NA		0	Circular and concaved out	Total uplift force ¹ reduction is 3.9%.
	0.160		NA	Total uplift force ¹ increase is 2.2%.			
	0.240		NA	Total uplift force ¹ increase is 12.5%.			
	0.080	1	NA		0	Circular and concaved in	Total uplift force ¹ reduction is 24.1%.
	0.160		NA	Total uplift force ¹ reduction is 21.3%.			
	0.240		NA	Total uplift force ¹ reduction is 5.1%.			
0.080	1	NA		0	Air foil shape	Total uplift force ¹ reduction is 27.9%.	
0.160		NA	Total uplift force ¹ reduction is 24.1%.				
0.240		NA	Total uplift force ¹ reduction is 10%.				
Kopp et al. 2005a, 2005b.	0.196 (0.382 at corners)	1	NA		0	Raised corners	Increased edge suction compared to a bare roof.
<i>Discontinuous</i>							
Kopp et al. 2005a, 2005b.	≤ 0.587	1	0	NA	0	Vertical and isolated.	Increased the edge suction compared to a bare roof.
Suaris and Irwin 2010	0.054	1	0	NA	0	Vertical and isolated.	Reduced corner and eave suction up to 12% and 30%, respectively. Negligible suction reduction along the gable ridge.

Table 5-4. Research Findings on Aerodynamic Devices – Parapets (Contd.)

Huang et al. 2013	0.0375	1	0	NA	0	Vertical and isolated.	Reduced corner suction up to 50%.
Kopp et al. 2005a and 2005b	0.196 (0.098 at corners)	1	NA		0	Vertical with slotted corners	Increased the edge suction compared to a bare roof.
Kopp et al. 2005a and 2005b	0.196	0.869	0.802	NA	0	Vertical with no corners.	Increased the edge suction compared to a bare roof.
Huang et al. 2013	0.0875	0.050	0	NA	0	Vertical and discrete with two, three and four segments spaced at 2.6 m, 1.5m, and 1.0 m, respectively.	Increased suction behind the edges with discrete parapets.
Surry and Lin 1995	0.192	0.296	0.437	NA	0	Vertical and spanning radially 15° from the corner.	Reduced corner suction by about 60%.
Surry and Lin 1995	0.064	0.037	0.037	NA	0	Vertical and single-sawtooth	Reduced corner suction by about 50%.
	0.064	0.074	0.074	NA	0	Vertical and dual-sawtooth	Reduced corner suction by about 30-40%.
	0.064	0.111	0.164	NA	0	Vertical and triple-sawtooth	Reduced corner suction by about 30-40%.
Surry and Lin 1995	[0.205]	1	1	NA	0	Semi-cylindrical projection.	Reduced corner suction more than 60%.
Chowdhury and Blessing 2007	[0.042]	1	0	NA	0	Vertical and isolated on windward edge. Trademarked product of AeroEdge - Gable edge cap vortex suppressor. Only for gable roofs.	Reductions in the roof uplift by 10-45% at majority of the locations. Helped to reduce the suction pressure throughout the entire roof surface, not just closer to the edge.
Huang et al. 2013	0.0375	0.05	0.083	NA	0	Vertical and at corners.	Reduced corner suction up to 33%.
Porous Parapets							
<i>Continuous (Perimetric)</i>							
Kopp et al. 2005a and 2005b	0.196	1	1	NA	50	Vertical	Reduced edge suction by about 20%.
<i>Discontinuous</i>							
Surry and Lin 1995	0.064	0.296	0.437	NA	50	Vertical and at corners.	Reduced corner suction up to 70%.

Table 5-5. Research Findings on Aerodynamic Devices - Parapets (Contd.)

Suaris and Irwin 2010	0.054	0.069	0.1	NA	33	Vertical at corners and at gable able ends.	Reduced corner and eave suction up to 60% and 20%, respectively. Negligible suction reduction along the gable ridge.
Cochran and English 1997	0.475	0	NA		75	Vertical and installed at the corner.	Reduced corner suction by 30%.
Kopp et al. 2005a, 2005b	0.196	0.869	0.802	NA	50	Vertical and porous corners	Increased the edge suction compared to a bare roof.
Surry and Lin 1995	0.192	0.296	0.437	NA	50	Vertical and spanning radially 15° from the corner.	Reduced corner suction by about 60%. The performance is better than equivalent solid radial splitters.
Chowdhury and Blessing 2007	0.033	1	0	NA	40-50%	Vertical and isolated on windward edge. Trademarked product of the AeroEdge for gable roofs - Gable edge screen vortex suppressor.	Increase or decrease in pressure depends on the location on the roof. Suction increased by 107% at one location on the roof edge. The roof pressure distribution is uniform.
Chowdhury and Blessing 2007	0.054	1	0		40-50%	Vertical and isolated on windward edge. Trademarked product of the AeroEdge for flat roofs - Flat roof AeroEdge guard.	Roof suction was reduced from 15-74%. The roof pressure distribution is uniform.
Chowdhury and Blessing 2007	0.033	1	0	NA	>0%	Vertical and isolated on windward edge. Trademarked product of the AeroEdge for flat roofs- Drain-thru gravel stop.	Slightly increased suction pressures.
Suaris and Irwin 2010	0.054	1	0	NA	20	Vertical and isolated.	Reduced edge and gable end suction up to 30%. Negligible suction reduction along the gable ridge.
*For curved devices $d = 2r$ (r is radius of the device)							
1 – Total uplift force = Uplift force on the roof + uplift force on the device							
Notations							
h_p – Height of the device			l_p – Length of the device			b_p – Width of the device	
h – Height of the building			L – Length of the building			B – Width of the building	

Table 5-6. Research Findings on Aerodynamic Devices – Spoilers

Spoiler type and reference	Geometry and details					Remarks	Research findings	Comments	
	h_p/h	l_p/L	l_p/B	b_p/h	Porosity (%)				
Spoilers									
<i>Continuous</i>									
Banks et al. 2001	0.0375	1	1	0.0563	NA	A flat plate is installed over discontinuous vertical legs along the eave of a flat roof.	Reduced corner suction up to 50%.	-	
Kopp et al. 2005a, 2005b	0.0032	1	1	0.0048	NA	-	Reduced the edge suction by about 50%.	-	
Banks et al. 2001	0.0686	1	1	0.0375 (here $b_p = d$)	NA	A cylinder is installed over discontinuous vertical legs along the eave of a flat roof.	Reduced corner suction up to 40%.	-	
Li et.al 2018	0.042	1	0	0.0625	NA	Installed at eaves.	Eave suction reduces 58-71%	Spoiler width of $L/20$, height of $0.02h-0.0625h$ and an angle greater than 30° at the windward eave is recommended.	
Bitsuamalak et al. 2013	0	1	1	0.133	NA	Trellis (pergolas) flushed to the eaves of gable and hip roofs.	Reduced windward eave suction up to 25%.	-	
Li et.al 2018	0.042	0	$\frac{0.57}{1}$	0.0625	NA	Gable end spoiler.	Gable end suction reduced up to 46%.	Spoiler width of $L/20$ and height of $0.02h-0.0625h$ and an angle $10^\circ-25^\circ$ at the gable end is recommended.	
Li et.al 2018	0.042	1	0	0.0313	NA	Gable ridge spoiler.	Ridge suction reduces 47-95%.	Spoiler width of $L/20$ and height of $0.02h-0.0625h$ is recommended.	
Notations									
h_p – Height of the device					l_p – Length of the device			b_p – Width of the device	
h – Height of the building					L – Length of the building			B – Width of the building	

The performance comparison of different aerodynamic mitigation features/devices revealed four major features that impact wind suction mitigation. They are dimension of the device [parapets and spoiler height (h_p), diameter (d) of cylindrical devices, width (b_p) of spoilers], length along the roof edge (l_p), location of the device on the roof (edges and/or corners), and the porosity. In addition, the building characteristics, roof characteristics, and wind characteristics affect the performance of a device. Although several studies have been conducted to evaluate the performance of different aerodynamic mitigation approaches, an organized output explaining the relationship between the performances of a device under different conditions has not been developed. The majority of the outputs of these studies is qualitative. The following is a summary derived from the review conducted for this study:

- Compared to solid parapets, porous parapets effectively reduce suction on a roof under the same wind conditions.
- Compared to parapets, the height of spoilers can be shorter but effective in reducing suction on a roof.
- Although discontinuous parapets reduced the wind suction on a roof compared to a bare roof, the discontinuity at the roof corners resulted in higher suctions at roof corners.
- Porous parapets require lesser heights compared to solid parapets to reduce the wind suction by equal magnitudes.
- Isolated parapets on the roof could result in an unintentional increase in the suction pressures on the roof based on the location of parapet and wind direction.
- Even though certain h_p/h ratios of the devices exhibit better performances in wind suction mitigation, the practicality of implementing such devices on structures while satisfying safety aspects and aesthetic considerations needs to be evaluated.

A few studies provide benchmark values for parameters such as relative device height, wind direction, and optimum porosity in parapets. However, these benchmark values are restricted by numerous conditions. For example, Eq. 1 can be used to calculate the required solid parapet height for a given structure to maintain the magnitude of the negative pressure less than twice the corresponding lift coefficients. The feasibility of using this equation for other conditions is not explicitly stated, thus limiting its application as a general tool.

$$h_p/h = K(B/h)^{2.7} \quad \text{Eq. 1}$$

where,

h_p = parapet height with respect to the roof

h = building height

B = width of the building plan

L = length of the building plan

K = numerical constant; $K = 0.01$ for $B/L = 1$, $K = 0.03$ for $B/L = 0$.

Eq 1 can only be used to design solid perimeter parapets, with limited B/L ratios for the base building. Design codes such as the ASCE 07-10 provide guidelines to calculate the design wind loads on a parapet; however, they do not provide the guidelines to calculate wind pressure on the roof in the presence of a parapet or any other aerodynamic feature/device. Therefore, design guidelines need to be established to calculate the wind loads on a roof in the presence of aerodynamic devices/features. These guidelines will help building designers to select a suitable aerodynamic damage mitigation approach for a given roof.

5.1.3 Wind Pressure Measurements of a Full-Scale Low-Rise Building

The full-scale testing of building models is performed under natural wind conditions and simulated wind conditions (generated using experimental apparatus such as wall-of-wind (WOW) or open-jet simulators). The full-scale testing under natural wind conditions is performed by instrumenting in-service or experimental structures. The Aylesbury structure (UK), the TTU building (Texas, USA), the Silsoe Structure (UK), the HNU building (China), and the TJU building (China), are a few experimental facilities that monitor the wind effects on field installed instrumented structures. The TTU building in Texas is one of the earliest instrumented buildings in the U.S. to monitor wind pressure distribution on the building envelope under prevailing wind conditions. The data gathered through full-scale studies under natural wind conditions have been used in the validation of numerical models and verification of scaled models used in wind tunnel testing

An experimental structure to collect wind pressure data mainly has four components. They are the experimental building, the meteorological system, the building response system, and the data acquisition system (DAS). The metrological system measures approaching wind characteristics (wind speed and direction). The building response system measures the response of the building (deflection, pressure, internal forces in structural members, and forces imposed on

the roofing fasteners) under wind loads. The experimental building is equipped with sensors to monitor the response of the structure. The measured response data and wind data are collected and interpreted through the DAS.

5.1.4 Numerical Simulation of the Flow around a Flat Roof of a Low-Rise Building

Commercially available CFD software such as Abaqus CFD, Ansys Fluent, OpenFoam, Star-CCM+, etc., are used to simulate behavior of wind around building roofs. The numerical results obtained through such models are validated with available experimental data. In this report, a numerical model is developed using Ansys Fluent to simulate the flow around a low-rise flat roof building. The low-rise flat roof building used in the study is a scaled model of the Silsoe Cube, which is an experimental structure in the UK that collects wind pressure data under natural wind conditions. The pressure coefficients down the mid-width of the building (along the windward wall, roof and leeward wall) are collected under a perpendicular wind direction (a wind perpendicular to the leading edge of the building). The simulation was conducted with several turbulence models. The numerical results were compared with available published experimental data.

The numerical simulation results indicated that the use of an adequate number of elements, finer meshes around the building surface to capture boundary layer variations, and the use of proper turbulence model affect the accuracy of numerical results.

5.2 RECOMMENDATIONS

5.2.1 Wind Suction Mitigation Approaches

- Contradicting results are presented in literature regarding the use of rounded edges as damage mitigation features. Therefore, the feasibility of using rounded roof edges as aerodynamic damage mitigation feature should be further evaluated by considering all the affecting parameters.
- A chamfer angle of 30° can be used a starting value for further studies.
- Perimetric spoilers have shown the best performance for controlling wind suction compared to parapets. In addition, they are aesthetically appealing. The following values are suggested for further analysis.

Device	Recommended value			
	h_p/h	b_p/h	l_p/L or l_p/B	Porosity
Spoilers	0.04	0.05	1	NA

- Solar panel arrays have become a popular choice on both flat and gable roof buildings. However, the wind pressure on the roof in the presence of solar panels could vary due to several factors such as building shape, module size, setback, array distance, tilt angle, wind turbulence, etc. This aspect should be further pursued to determine the best orientation of solar panels to reduce uplift force acting on the roof as well as the solar panels.
- A set of guidelines to determine pressure distribution on a roof with aerodynamic features/devices needs to be developed. For buildings with different plan dimensions (width/length ratio of the building – B/L) the pressure coefficients at three zones (edge, corner and interior) can be specified with respect to wind directions, aerodynamic device, and device dimensions (device height normalized with respect to the height of the building – h_p/h). Figure 2 shows the proposed format of a design chart to calculate pressure at three zones (Zone 1, Zone 2, and Zone 3) of a flat roof on a square building ($B/L = 1.0$) with perimetric solid parapets ($h_p/h = 0.01, 0.05, 0.10, \text{ and } 0.15$) and subjected to a 30° wind.

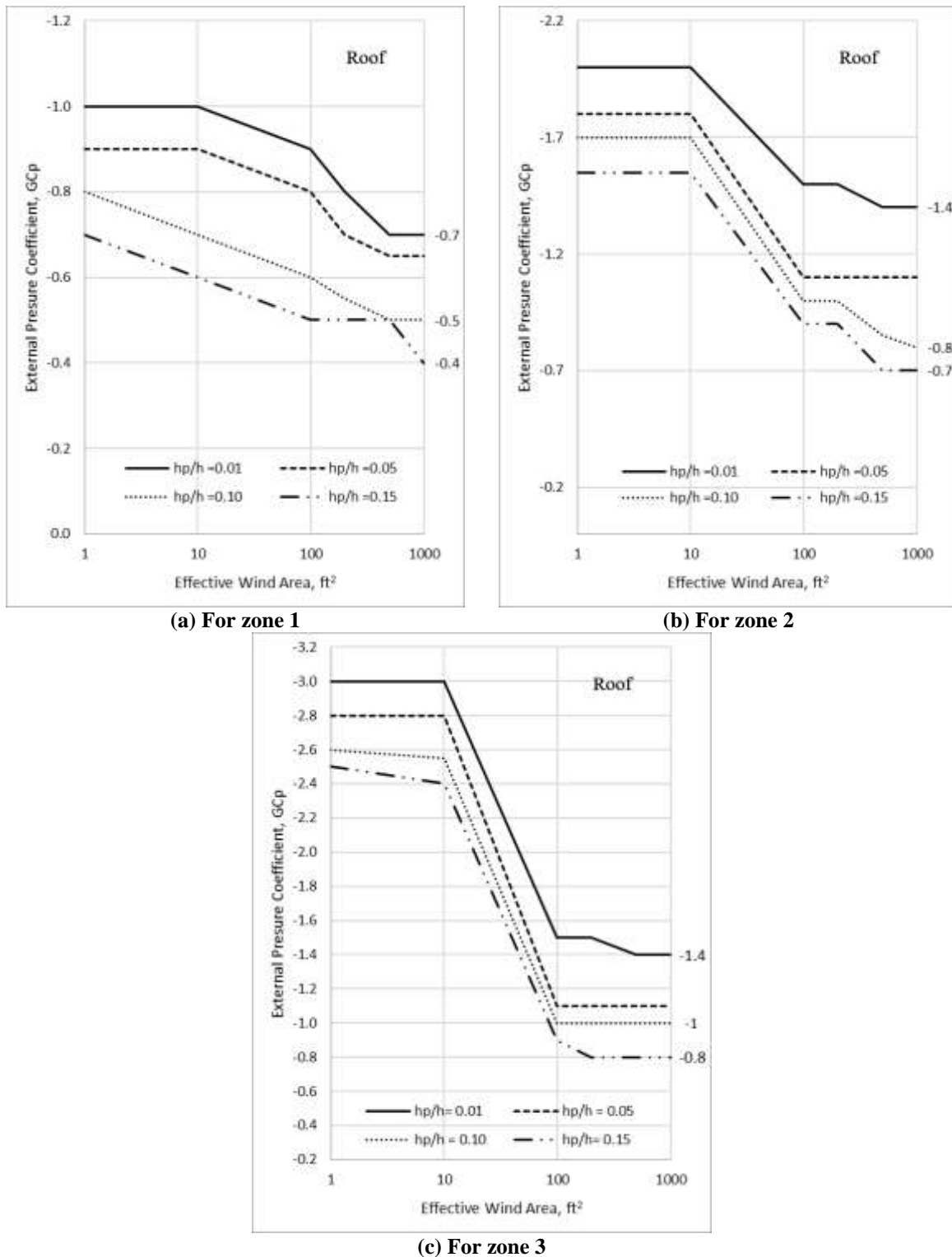


Figure 5-1. Proposed design chart format for a flat roof with perimetric solid parapets on a rectangular building ($B/L = 1.0$) subjected to a wind flowing at 30°

Note: h_p : Parapet height, h : building height, B : building width, L : building length, wind direction 0° is parallel to the longer dimension of the roof

5.2.2 Numerical Simulations to Predict Wind Loads on Flat Roofs

- Numerical simulation capabilities and results are promising. To yield the full potential acquisition of necessary simulation tools are necessary.
- Wind suction pressure observed from numerical simulations was higher than that observed through experimental results. The roofing flexibility could be a possible cause for this observation. Therefore, the structural and material characteristics of roof assembly need to be incorporated into the numerical model. A coupled wind-structure interaction analysis should be performed to study the resulting wind pressure over the roof.
- A comprehensive experimental database with explicit data is required to validate numerical models. The required data include wind pressure distribution over the roof, membrane deflection, approaching wind profile at several locations in the domain, turbulent intensity profile of the wind with the location on the domain, etc. Therefore, either wind tunnel tests on scaled building models should be carried out, or measurements should be obtained from a full-scale instrumented experimental structure. Since experimental structures are not yet implemented under extreme winter weather conditions, the structure presented in Chapter 4 can be implemented to collect as-needed data.
- The evaluations conducted so far on aerodynamic damage mitigation features/devices are not comprehensive. Hence, a study needs to be initiated to evaluate only the ones that have shown a promise based on the studies conducted so far to develop design charts discussed in sec 5.2.1. This can be accomplished through validated numerical models.

6 REFERENCE

1. Abohela, I., Hamza, N., and Dudek, S. (2013). "Effect of roof shape, wind direction, building height and urban configuration on the energy yield and positioning of roof mounted wind turbines." *Renewable Energy*, 50(2013), 1106-1118.
2. Alliance Coastal Technologies. (2011). "Gill UVW Anemometer." <<http://www.act-us.info/sensordetail.php?ID=13766&cat=&type=>> (July 25, 2019).
3. Aly, M. A. and Bresowar, J. (2016). "Aerodynamic mitigation of wind-induced uplift forces on low-rise buildings: A comparative study." *Journal of Building Engineering*, 5, 267-276.
4. Aly, M. A., Chokwitthaya, C., and Poche, R. (2017). "Retrofitting building roofs with aerodynamic features and solar panels to reduce hurricane damage and enhance eco-friendly energy production." *Sustainable Cities and Society*, 35, 581-593.
5. American Earth Anchors. (2019a). "PE46Hex: Specifications." Quick Reference, <<https://americaneearthanchors.com/files/2414/3255/6630/pe46hex-specifications-installation.pdf>> (July 05 2019).
6. American Earth Anchors. (2019b). "Penetrator 90° bracket for large Penetrators." Brackets and Sleeves, <https://americanea.amercommerce.com/penetrator-90-bracket-for-large_penetrators.aspx> (July 05 2019).
7. American Society of Civil Engineers (ASCE). (2010). *ASCE/SEI 7-10: Minimum Design Loads for Buildings and Other Structures*, American Society of Civil Engineers, Virginia, USA.
8. American Tower Company (2005a). "50' Free Standing 1810-18" Triangular Steel Tower." American Tower Company, Shelby, Ohio 44875.
9. American Tower Company (2005b). "50' Free Standing 1810 -18 Triangular Steel Tower Foundation." American Tower Company, Shelby, Ohio 44875.
10. Amerite Tower. (2018a). "AME55-BGR-Ground & Roof Plate." Amerite Series 55 Tower, Tower Sections, <<https://amertower.com/amerite-series-towers/>> (July 25, 2019).
11. Amerite Tower. (2018b). "AME55-10' Mid." Amerite Series 55 Tower, Tower Sections, <<https://amertower.com/wp-content/uploads/2018/04/Amerite-55midsection.pdf>> (July 25, 2019).

12. Amerite Tower. (2018c). “AME55-B5- 5’ Base.” Amerite Series 55 Tower, Tower Sections, <<https://amertower.com/wp-content/uploads/2018/04/Amerite-55tower5ftbasesection.pdf>> (July 25, 2019).
13. Amerite Tower. (2018d). “AME55-BGR-Ground & Roof Plate.” Amerite Series 55 Tower, Tower Sections, <<https://amertower.com/wp-content/uploads/2018/04/Amerite-55concretebpweldment.pdf>> (July 25, 2019).
14. Ansys. (2019). “Fluid-Structure Interaction.” Multiphysics Simulation, <<https://www.ansys.com/products/platform/multiphysics-simulation/fluid-structure-interaction>> (August 14, 2019).
15. Aponte- Bermudez, L. D. (2006). “Measured Hurricane wind Pressure on Full-Scale Residential Structures: Analysis and Comparison to Wind Tunnel Studies and ASCE-7.” PhD Dissertation, University of Florida, Florida.
16. Attanayake, U. and Aktan, H. (2019). “Noncontact Measurement of Bridge Load Response Using He–Ne Modulated Lasers.” *Journal of Bridge Engineering*, 24(11), 04010101.
17. ATI Industrial Automation. (2019a). “F/T Sensor: Nano25 IP65/68.” F/T models, <https://www.ati-ia.com/products/ft/ft_models.aspx?id=Nano25+IP65%2fIP68> (August 5, 2019).
18. ATI Industrial Automation. (2019b). “F/T Transducer: Six axis Force/Torque Sensor System.” Installation and Operation Manual, Document #: 9620-05-Transducer Section, ATI Industrial Automation, Goodworth Drive, Apex, NC 27539, USA.
19. Balderrama, J. A., Masters, F. J., Gurley, K. R., Prevatt, D. O., Aponte-Bermudez, L. D., Reinhold, T. A., Pinelli, J. P., Subramanian, C. S., Schiff, S. D., and Chowdhury, A. G. (2011). “The Florida Coastal Monitoring Program (FCMP): A review.” *Journal of Wind Engineering and Industrial Aerodynamics*, 99(2011), 979-995.
20. Banks, D., Meroney, R. N., Sarkar, P. P., Zhao, Z., and Wu, F. (2000). “Flow visualization of conical vortices on flat roofs with simultaneous surface pressure measurement.” *Journal of Wind Engineering and Industrial Aerodynamics*, 84, 65-85.
21. Banks, D., Sarkar, P. P., Wu, F., and Meroney, R. N. (2001). “A Device to Mitigate Vortex Induced Rooftop Suction.” Americas Conference on Wind Engineering, June 4-6, 2001, Clemson University, South Carolina, 10 pages.

22. Baskaran, A., Molleti, S., Ko, S., and Reenen, D. V. (2012). "Field-Monitoring the Wind Performance of Commercial Roofs, Part 1: Data from Ottawa Site." Proceedings, 27th RCI International Convention and Trade Show, March 15-20, 2012, 51-58.
23. Bassett, R. (2013). "Laser Displacement Sensors." Technology Focus, <<https://www.automationworld.com/technology-focus-laser-displacement-sensors>>. (June 18, 2019).
24. Bitsuamalak, G. T., and Teclé, A.S. (2009). *Full-scale external and internal pressure measurements for a low-rise building*. Florida State University, Florida, USA.
25. Bitsuamalak, G. T., Warsido, W., Ledesma, E., and Chowdhury, A. G. (2013). "Aerodynamic Mitigation of Roof and Wall Corner Suctions using Simple Architectural Elements." *Journal of Engineering Mechanics*, 139(3), 396-408.
26. Bienkiewicz, B. and Sun, Y. (1992). "Local wind loading on the roof of a low-rise building." *Journal of Wind Engineering and Industrial Aerodynamics*, 45 (1992), 11-24.
27. Blackmore, P. A. (1988). "Load Reduction on Flat Roofs – The Effect of Ridge Profile." *Journal of Wind Engineering and Industrial Aerodynamics*, 29, 89-98.
28. Caracoglia, L. and Jones, N. P. (2009). "Analysis of Full-Scale Wind and Pressure Measurements on a Low-Rise Building." *Journal of Wind Engineering and Industrial Aerodynamics*, 97(2009), 157-173.
29. Chowdhury, A. G. and Blessing, C. (2007). "Mitigation of Roof Uplift through Vortex Suppression Techniques." Report for the State of Florida in partnership with The International Hurricane Research Centre, FIU.
30. Chowdhury, A. G., Moravej, M., Zisis, I., Irwin, P., Tremante, A., and Hajra, B. (2019). "Mitigation of Aerodynamic Uplift Loads Using Roof Integrated Wind Turbine Systems." *Frontiers in Building Environment*, 5, Article 10, 1-9.
31. Cochran, L. S., and English, E. C. (1997). "Reduction of Roof Wind Loads by architectural Features." *Architectural Review*, 40(3), 79-87.
32. Cochran, L. S., and Derickson, R. (1999). "Roof Surface Wind Speed Distributions on Low-rise Buildings." *Architectural Science Review*, 42(3), 151-160.
33. Cook, N. J. (1985). *The designer's guide to wind loading of building structures*. Building Research Establishment (BRE), London.

34. Dantec Dynamics. (2019). *Probes for Hot-wire Anemometry*. Publication No. 238v12, Dantec Dynamics.
35. Dong, X., Ding, J., and Jiao, C. (2019). “Wind loads on flat roofs of low-rise buildings with rounded leading edge.” *Journal of the Chinese Institute of Engineers*, 42 (3), 264-277.
36. DX Engineering. (2019). “Amerite Joint Bolt Kits AME55BK.”
<<https://www.dxengineering.com/parts/tow-ame55bk>> (July 28, 2019).
37. Eaton, K. J. and Mayne, J. R. (1975). “The Measurement of Wind Pressures on Two-Storey Houses at Aylesbury.” *Journal of Industrial Aerodynamics*, 1 (1975), 67-109.
38. Enteria, N. A. (2016). “CFD Evaluation of Philippine Detached Structure with Different Roofing Deigns. *Infrastructures*, 1 (3), 1-15.
39. Fasteners Plus. (2018). “Simpson H8 Hurricane Tie – G90 Galvanized.” H/TSP Seismic & Hurricane Ties, <https://www.fastenersplus.com/Simpson-H8-Hurricane-Tie-G90-Galvanized?gclid=EAIaIQobChMIgvdGDhdC54wIVx8DACH3zbwp1EAQYAiABEgK7CPD_BwE> (July 29, 2019).
40. FEMA. (2005). *FEMA 490: Summary Report on Building Performance-2004 Hurricane Season*, FEMA, Washington, DC.
41. FEMA. (2006). *FEMA 549: Hurricane Katrina in the Gulf Coast-Building Performance Observations, Recommendations and Technical Guidance*, FEMA, Washington, DC.
42. FEMA. (2012). *FEMA P-908: Spring 2011 Tornadoes-April 25-28 and May 22*, FEMA, Washington, DC.
43. Fernandez-Caban, P. L., Masters, F. J., and Phillips, B. M. (2018). “Predicting Roof Pressures on a Low-Rise Structure from Freestream Turbulence using Artificial Neural Networks”. *Frontiers in Built Environment*, 4, Article no. 68.
44. Gerhard, H. J., and Kramer, C. (1992). “Effect of building geometry on roof wind loading.” *Journal of Wind Engineering and Industrial Aerodynamics*, 43(1-3), 1765-1773.
45. Ginger, J. D., and Letchford, C. W. “Peak wind loads under delta wing vortices on canopy roofs.” *Journal of Wind Engineering and Industrial Aerodynamics*, 43(1-3), 1739-1750.
46. Halfmann, A., Rank, E., Glück, M., Breuer, M., and Durst, F. (2000). “A Partitioned Solution Approach for the Fluid-Structure Interaction of Wind and Thin-Walled Structures.” Technische Universität, München.

47. Holmes, J. D. (2001). *Wind Loading of Structures*. Spon Press, Taylor & Francis Group, 29 West 35th Street, New York, NY 10001.
48. Home depot. (2019). "SmartSide 48 in. × 96 in. Strand Panel Siding." Composite Siding, <<https://www.homedepot.com/p/LP-SmartSide-SmartSide-48-in-x-96-in-Strand-Panel-Siding-27874/100055901>> (July 31, 2019).
49. Ho-Tak, H. (1988). "Pressure Measuring System for Wind-Induced Pressure on Building Surfaces." Thesis, Degree of Master of Science in Civil Engineering, Texas Tech University, Texas.
50. Hsu, M. C. and Bazilevs, Y. (2012). "Fluid-Structure interaction modeling of wind-turbines: simulating the full machine." *Comput. Mech.*, 50, 821-833.
51. Huang, P., Wang, X., and Gu, M. (2012). "Field Experiments for Wind Loads on a Low-Rise Building with Adjustable Roof Pitch." *International Journal of Distributed Sensor Networks*, Hindawi Publishing Corporation, 2012.
52. Huang, S., Li, R., and Li, Q. S. (2012). "Numerical Simulation on Fluid-structure Interaction of Wind around Supper-tall Building at High Reynolds Number Conditions." Proceedings, 202 World Congress on Advances in Civil, Environmental, and Materials Research (ACEM 12), Seoul, Korea, August 26-30, 2012, pp. 3075-3091.
53. Huang, P., Gu, M., Jia, C., and Quan, D. (2013). "Field Measurement of Wind Effects of Roof Accessory Structures on Gable-Roofed Low-Rise Building." *International Journal of Distributed Sensor Networks*, 2013(1-3).
54. Huang, P., Peng, X., and Gu, M. (2014). "Aerodynamic devices to mitigate rooftop suction on a gable roof building." *Journal of Wind Engineering and Industrial Aerodynamics*, 135, 90-104.
55. Hufnagel, K. and Schewe, G. (2007). "Force and Moment Measurement." *Handbook of Experimental Fluid Mechanics*, Springer Handbook, Springer, Berlin, Heidelberg.
56. Irtaza, H., Beale, R. G., Godley, M. H. R., and Jameel, A. (2013). "Comparison of wind pressure measurements on Silsoe experimental building from full-scale observation, wind-tunnel experiments and various CFD techniques." *International Journal of Engineering, Science and Technology*, 5(1), 28-41.

57. Iverson, L. M. (2016). "Aerodynamic Mitigation of Roof Suction Using Solar Panels." Thesis, Degree of Master of Science in Civil Engineering, Louisiana State University and Agricultural College, Louisiana.
58. Jing, X. and Li, Y. (2013). "Wind Tunnel Tests for Wind Pressure Distribution on Gable Roof Buildings." *The Scientific World Journal*, Hindawi Publishing Corporation, 2013.
59. Katsaros, K. B. (2001). Sensors for Mean Meteorology. *Encyclopedia of Ocean Sciences*, Second Edition, 375-381.
60. Kawai, H. "Structure of conical vortices related with suction fluctuation on a flat roof in oblique smooth and turbulent flows." *Journal of Wind Engineering and Industrial Aerodynamics*, 69-71, 579-588.
61. Keote, S. A., Kumar, D., and Singh, R. (2015). "Construction of Low-Rise Buildings in Cyclone Prone Areas and Modification of Cyclone". *Journal of Energy and Power Sources*, 2 (7), 247-252.
62. Keyence Corporation. (2019). "What is an inductive displacement sensor?" Inductive displacement sensors, <https://www.keyence.com/ss/products/sensor/sensorbasics/eddy_current/index.jsp> (June 17, 2019).
63. Khanduri, A. C., Stathopoulos, T., and Bédard, C. (1998). "Wind induced interference effects on buildings – a review of the state-of-the-art." *Engineering Structures*, 20, 617-630.
64. Kim, S. I. and Mehta, K. C. (1980). "Full-scale measurements on a flat roof area." Proceedings, Fifth International conference on Wind Engineering, Vol 1, Pergamon Press, J. E. Cemak, Ed., 1980, pp 357-367.
65. Knight, J. J., Lucey, A. D., and Shaw, C. T. (2010). "Fluid-Structure interaction of a two-dimensional membrane in a flow with a pressure gradient with application to convertible car roofs." *Journal of Wind Engineering and Industrial Aerodynamics*, 98(2), 65-72.
66. Kopp, G. A., Surry, D., and Mans, C. (2005a). "Wind effects of parapets on low buildings: Part 1. Basic aerodynamics and local loads." *Journal of Wind Engineering and Industrial Aerodynamics*, 93, 817-841.

67. Kopp, G. A., Mans, C., and Surry, D. (2005b). "Wind effects of parapets on low buildings: Part 4. Mitigation of corner loads with alternative geometries." *Journal of Wind Engineering and Industrial Aerodynamics*, 93, 873-888.
68. Leutheusser, H. J. (1964). *TP 6404: The Effects of Wall Parapets on the Roof Pressure-Coefficients of Block-Type and Cylindrical Structures*. Technical Publication Series, Department of Mechanical Engineering, University of Toronto.
69. Levitan, M. L. and Mehta, K. C. (1992a). "Texas Tech Field Experiments for Wind Loads, Part 1: Building and Pressure Measuring System." *Journal of Wind Engineering and Industrial Aerodynamics*, 41-44, 1565-1576.
70. Levitan, M. L. and Mehta, K. C. (1992b). "Texas Tech Field Experiments for Wind Loads, Part 2: Meteorological Instrumentation and Terrain Parameters." *Journal of Wind Engineering and Industrial Aerodynamics*, 43 (1-3), 1577-1588.
71. Li, Q. S., Hu, S. Y., Da, Y. M., and Li, Z. N. (2009). "Extreme Value Analysis for Filed Measured Peak Pressure Coefficients on a Low-Rise Building." The Seventh Asia-Pacific Conference on Wind Engineering, November 8-12, 2009, Taipei, Taiwan.
72. Li, Q. S., Hu, S. Y., Dai, Y. M., and He, Y. C. (2012a). "Field Measurements of extreme pressures on a flat roof of a low-rise building during typhoons." *Journal of Wind Engineering and Industrial Aerodynamics*, 111 (2012), 14-29.
73. Li, Q. S., Hu, S. Y., and Dai, Y. M. (2012b). "Field Measurements of wind loads on an instrumented low-rise building during typhoons and comparison with wind tunnel test results." The Seventh International Colloquium on Bluff Body Aerodynamics and Applications (BBAA7), Shanghai, China, September 2-6, 2012, pgs. 1187-1196. Published by: International Association for Wind engineering.
74. Li, Q. S. and Yu, S. Y. (2014). "Monitoring of Wind Effects on a Low-Rise Building during Typhoon Landfalls and Comparison to Wind Tunnel Test Results." *Structural Control and Health Monitoring*, 21, 1360-1386.
75. Li, Q. S., Wang, Y. g., and Li, J. C. (2017a). "Monitoring of wind effects on an instrumented low-rise building during the landfall of a severe tropical storm." *Structural Control and Health Monitoring*, 24, e1917.

76. Li, G., Gan, S., Li, Y., and Wang, L. (2017b). “Wind-induced interference effects on low-rise buildings with gable roof.” *Journal of Wind Engineering and Industrial Aerodynamics*, 170 (2017), 94-106.
77. Li, G., Gan, S., and Li, H. (2018). “Wind Pressure Mitigation on Gable Roofs for Low-Rise Buildings Using Spoilers.” *Journal of structural Engineering*, 144 (8), 0.4018104.
78. Lin, J. X., Surry, D., and Tieleman, H. W. (1995). “The Distribution of Pressure near Roof Corners of Flat Roof Low Buildings.” *Journal of Wind Engineering and Industrial Aerodynamics*, 26, 235-265.
79. Lin, J. X., Montpellier, P. R., Tillman, C. W., and Riker, W. I. (2008). “Aerodynamic Devices for Mitigation of Wind Damage Risk.” 4th International Conference on Advances in Wind and Structures (AWAS’08), Jeju, Korea, May 29-31, 1533-1546.
80. Lowes. (2019a). “Trex Enhance Basics 12-ft Saddle grooved Composite Deck Board.” Composite Deck Boards, <<https://www.lowes.com/pd/Trex-Enhance-Basics-12-ft-Saddle-Grooved-Composite-Deck-Board/1000763542> > (July 31, 2019).
81. Lstiburek, J. W. (2012). “Parapets: Where Roofs Meet Walls.” Insight – 050, Building Science Corporation.
82. Mahmood, M., Srinivas, K., and Budair, M. O. (2008). “Experimental Study of Flow past a Low-Rise Building.” *The Arabian Journal for Science and Engineering*, 33 (2B), 551-568.
83. Mahmood, M. (2011). Flow Visualization in Wind Tunnels. *Wind Tunnels and Experimental Fluid Dynamics Research*, Prof. Jorge Colman Lerner (Ed.), ISBN: 978-953-307-623-2, 99-114.
84. Masters, F. J. and Gurley, K. R. (2011). “Wind Resistance of Clay and Concrete Roofing Tiles.” Engineering School of Sustainable Infrastructure & Environment, University of Florida.
85. Meecham, D. (1992). “The Improved Performance of Hip Roofs in Extreme Winds – A Case Study.” *Journal of Wind Engineering and Industrial Aerodynamics*, 43(1), 1717-1726.
86. Micro-Epsilon. (2019). “Inductive sensors (eddy current) for displacement, distance and position.” Sensors for displacement, distance and position, <<https://www.micro-epsilon.com/displacement-position-sensors/>> (June 18, 2019).

87. Migatron Corporation. (2001). *RPS-100*, Migatron Corp, Woodstock, IL 60098 USA.
88. Migatron Corp. (2015). “Precisely Measure Distances with Ultrasonic Sensors.” Distance Measurement Sensors, <<https://www.migatron.com/distance-measurement-sensors/>> (June 18, 2019).
89. National Instruments. (2017). PXI Express-NI PXIe-1065 User Manual, National Instruments, Austin, Texas 78759, USA.
90. National Instruments. (2019a). “What is Data Acquisition?” <<http://www.ni.com/data-acquisition/what-is/>> (July 21, 2019).
91. National Instruments. (2019b). “Model: PXIe-1065, Part number: 779730-01” PXI Chassis, <<http://www.ni.com/en-us/shop/select/pxi-chassis>> (August 01, 2019).
92. Ntinias, G. K., Zhang, G., Fragos, V. P., Bochtis, D. D., Nikita-Martzopoulou, C. (2014). “Airflow patterns around obstacles with arched and pitched roofs: Wind tunnel measurements and direct simulation.” *European Journal of Mechanics B/Fluids*, 43 (2014), 216-229.
93. Özmen, Y. and Baydar, E. (2016). “Experimental investigation of wind pressure fields on buildings with gabled roofs having different pitch angles.” *Journal of Thermal Science and Technology*, 36(2), 7-17.
94. Pindado, S., Meseguer, J., Franchini, S., and Barrero, A. (2009). “On the reduction of the wind-load on buildings by using cantilever parapets.” 4th International building Physics Conference, Istanbul, Turkey, June 15-June 18, 2009, Volume: Energy Efficiency and New Approaches (ISBN: 978-975-561-350-5).
95. Pindado, S., Meseguer, J., and Franchini, S. (2011). “Influence of an Upstream Building geometry on the Wind-induced Mean suction on the Flat roof of a Low-rise Building.” *Journal of Wind Engineering and Industrial Aerodynamics*, 99, 889-893.
96. Piperno, S. and Bournet, P.E. (2012). “Numerical simulations of wind effects on flexible civil engineering structures.” *Revue européenne des éléments finis*, 8(5).
97. Prasad, D. and Ahmed, M. R. (2009). “Wind Loads on Low-Rise building Models with Different Roof Configurations.” *International Journal of Fluid Mechanics Research*, 36(3), 231-243.

98. Qiu, Y., San, B., and Zhao, Y. (2019). “Numerical Simulation and Optimization of Wind Effects of Porous Parapets on Low-Rise Buildings with Flat Roofs.” *Advances in Civil Engineering*, 2019, Hindawi Publications, Article ID: 3402613.
99. Quimby, T. B. (2007). “Wind Loads: The ASCE 7 Provisions”. A Beginner’s Guide to ASCE 07-05, <<https://slideplayer.com/slide/3317544/>> (March 04, 2019).
100. Richards, P. J., Hoxey, R. P., and Short, L. J. (2001). “Wind Pressures on a 6 m Cube.” *Journal of Wind Engineering and Industrial Aerodynamics*, 89(2001), 1553-1564.
101. Roelfs, F. and Shams, A. “CFD-Introduction.” *Thermal Hydraulics Aspects of Liquid Metal Cooled Nuclear Reactors*, Woodhead Publishing, United Kingdom, pp 213-218.
102. R. M. Young. (2019a). “Meteorological Instruments-Ultrasonic Anemometer Model 81000.” Instructions Manual, R. M. Young Company, 2801 Aero Park Drive, Traverse City, MI, 49686, USA.
103. R. M. Young. (2019b). “Wind Sentry - Model 03002/03102.” Mechanical Wind Sensors, <<http://www.youngusa.com/products/7/74.html>> (July 25, 2019).
104. R. M. Young. (2019c). “Wind Monitor – Model 05103.” Mechanical Wind Sensors, <<http://www.youngusa.com/products/7/5.html>> (July 25, 2019).
105. R. M. Young. (2019d). “Ultrasonic Anemometer – Voltage and Serial Outputs – Model 86000.” Ultrasonic Wind Sensors, <<http://www.youngusa.com/products/6/69.html>> (July 25, 2019).
106. R. M. Young. (2019e). “Ultrasonic Anemometer - Voltage and Serial Outputs – Model 81000.” <<http://www.youngusa.com/products/11/3.html>> (July 25, 2019).
107. Ricci, M., Patruno, L., and De Miranda, S. (2017). “Wind loads and structural response: Benchmarking LES on a low-rise building.” *Engineering Structures*, 144 (2017), 26-42.
108. Richards, P. J., Hoxey, R. P., Connell, B. D., and Lander, D. P. (2007). “Wind-tunnel modelling of the Silsoe Cube.” *Journal of Wind Engineering and Industrial Aerodynamics*, 95(2007), 1384-1399.
109. Richards, P. J. and Hoxey, R. P. (2012). “Pressures on a cubic building-Part 1: Full-scale results.” *Journal of Wind Engineering and Industrial Aerodynamics*, 102(2012), 72-86.
110. Sarkar, P. (2001). “Full-scale study of conical vortices and roof corner pressures.” *Wind and Structures*, 4(2), 131-146.

111. Scanivalve Corp. (2016). "Ethernet Pressure Scanner." Digital Sensor Array, Data Sheet No. G511, Scanivalve Corp, Liberty Lake, WA 99019.
112. Scanivalve Corp. (2019). "Scanivalve: Pneumatic connector, Tubing, & Accessory Catalog." Scanivalve Corp, Liberty Lake, WA 99019.
113. Sehn, K. (2008). "Aerodynamic mitigation of extreme wind loading on low-rise buildings." Thesis, Degree of Master of Science in Engineering, Iowa State University, Iowa.
114. Shea, A. D., Robertson, A. P., Levermore, G. J., and Rideout, N. M. (2010) "Measurement of the Performance of a Wind-Driven Ventilation Terminal." *Structures and Buildings*, 163(2), 129-136.
115. Singh, J. and Roy, A. K. (2019). "Effects of roof slope and wind direction on wind pressure distribution on the roof of a square plan pyramidal low-rise building using CFD simulation". *International Journal of Advanced Structural Engineering*, 11, 231-254.
116. Smith, D. A., Morse, S. M., and Mehta, K. C. (2017). *Wind Engineering Research Field Laboratory Selected Data Sets for Comparison to Model-Scale, Full-Scale and Computational Fluid Dynamics Simulations*, Wind Science and Engineering Research Center, Texas Tech University, Lubbock, Texas.
117. Solid Signals. (2019). "American Tower 3' Side Arm for AME 25 AME45 and AME55 Towers (SA-AME)." American Tower Company SA-AME, < <https://www.solidsignal.com/pview.asp?p=sa-ame> > (Jul 31, 2019).
118. Stathopoulos, T., and Baskaran, A. (1987). "Wind Pressures on Flat Roofs with Parapets." *Journal of Structural Engineering*, 113(11), 2166 – 2180.
119. Suaris, W. and Irwin, P. (2010). "Effect of roof-edge parapets on mitigating extreme roof suctions." *Journal of Wind Engineering and Industrial Aerodynamics*, 98, 483-491.
120. Sun, X. Y., Chen, Z. Q., Wu, Y., and Shen, S. Z. (2012). "Numerical studies on the behaviors of wind-structure interaction for membrane structures." Proceedings, Seventh International Colloquium on bluff Body aerodynamics and Applications (BBAA&), Shanghai, China, Sep 2-6, 2012, pp 234-243.
121. Surry, D. and Lin, J. X. (1995). "The Effect of Surroundings and Roof Corner Geometric Modifications on Roof Pressures on Low-rise Buildings." *Journal of Wind Engineering and Industrial Aerodynamics*, 58, 113-138.

122. Tominga, Y., Akabayashi, S., Kitahara, T., and Arinami, Y. (2015). "Air Flow around isolated gable-roof buildings with different roof pitches: Wind tunnel experiments and CFD simulations." *Building and Environment*, 84 (2015), 204-213.
123. UNISTRUT. (2017). *General Engineering Catalogue – No 17 A*. Atkore International, Harvey, IL.
124. Vardoulakis, S., Dimitrova, R., Richards, K., Hamlyn, D., Camilleri, G., Weeks, M., Sini, J., Britter, R., Borrego, C., schatzmann, M., and Moussiopoulos, N. (2011). "Numerical Model Inter-comparison for Wind Flow and Turbulence around Single Block Buildings." *Environ Model Assess*, 16, 169-181.
125. Wang, K. (1998). "Wind Pressure Coefficients for Gable roofs of Intermediate Slopes." Thesis, Degree of Master of Applied Science, Concordia University, Montreal, Quebec, Canada.
126. Wang, X. J., Li, Q. S., Yan, B. W., and Li, J. C. (2018). "Field measurements of wind effects on a low-rise building with roof overhang during typhoons." *Journal of Wind Engineering and Industrial Aerodynamics*, 176(2018), 143-157.
127. Wu, F. (2000). "Full-Scale Study of Conical Vortices and their Effects near Roof Corners." PhD Dissertation, Texas Tech University, Texas.
128. Xu, Y. L. and Reardon, G. F. (1998). "Variations of wind pressure on hip roofs with roof pitch." *Journal of Wind Engineering and Industrial Aerodynamics*, 73, 267-284.
129. Xu, W., Peng, H., and Ming, G. (2012). "Field Measurement of wind loads on low-rise Building with Adjustable Roof Pitch." The Seventh International Colloquium on Bluff Body Aerodynamics and Applications (BBAA7), Shanghai, China, September 2-6, 2012, 1197-1208.
130. Yu, H., Tang, Y. H., Gordon, J. E., and Jeong, D. Y. (2009). "Modelling the Effect of Fluid-Structure Interaction on the Impact Dynamics of Pressurized Tank Cars." Proceedings of ASME International Mechanical Engineering Congress and exposition (IMECE), Nov 13-19, Lake Buena Vista, FL, USA.
131. Zsis, I. and Stathopoulos, T. (2009). "Wind-Induced Cladding and Structural Loads on Low-Wood Building." *Journal of Wind Engineering and Industrial Aerodynamics*, 135(4), 437-447.